A SPECTROSCOPIC ANALYSIS OF THE ECLIPSING NOVA-LIKE EC21178-54

ZWIDOFHELANGANI NDAMULELO KHANGALE

December 2013

A project submitted in partial fulfilment of the requirements for the degree M.Sc.
in the Department of Astronomy, as part of the National Astrophysics
and Space Science Programme
UNIVERSITY OF CAPE TOWN

Supervisor: A/Prof P.A. Woudt

Abstract

EC21178-54 is a 13.7 magnitude eclipsing nova-like (NL) cataclysmic variable (CV) discovered in the Edinburgh-Cape survey of blue objects. It has an orbital period of 3.708 hours. High-speed photometric analysis of its light curve reveal that this system is a rich source of quasi-periodic oscillations (QPOs), dwarf nova oscillations (DNOs) and the other type of periodic oscillations called longer period dwarf nova oscillations (lpDNOs). Its light curve shows a deep symmetrical V-shaped primary eclipse, and its spectra show strong broad double-peaked emission.

In this project we present phase-resolved spectroscopy of the eclipsing nova-like CV EC21178-54. The average spectrum of EC21178-54 shows broad double-peaked emission lines from HeII 4686Å, and the Balmer series. HeII 4686Å dominates the Balmer lines; and in the Balmer lines the blueshifted component is the stronger of the two. The high-excitation feature, CIII/NIII at 4640-4650 Å, is also present and appear broad in emission. A number of other lines, mostly HeI, are clearly present in absorption and/or emission.

Phase-binned spectra of EC21178-54 show orbital variations of both emission and absorption features. A close examination of HeII 4686Å reveals that this line is double-peaked with time variable separation. H_β and H_γ on the other hand, show double-peaked emission profiles most of the time, which sometimes switch to absorption on the redshifted component. H_δ and H_ϵ show the same behaviour as that of H_β and H_γ but, for the former two lines, absorption dominates.

In this work, I have focused on the strongest lines in the spectra, HeII λ4686, H_α, and H_β. Radial velocity curves of these strongest features give the average velocity amplitude, $K_1 \approx 143 \pm 19$ km/s, and systemic heliocentric velocity $\gamma \approx$ -50 ± 14 km/s. Doppler maps of these emission lines revealed the presence of a highly-inclined asymmetric accretion disc and a two spiral arm-like structure in the tomograms of HeII 4686Å. The spiral structure dominates emission in the Doppler maps of HeII 4686Å. The bright spot is absent in both the Doppler maps of HeII 4686Å and the Balmer lines. The Doppler maps of HeII 4686Å shows no evidence of emission from the secondary, and this suggests that this line originate from the inner region of the accretion disc. However, the Doppler map of H_β, does show emission associated with the secondary star but this could be an artifact. Generally, the emission in EC21178-54 is dominated by emission from the accretion disc. Based on all these characteristics we conclude that EC21178-54 is a member of RW Triangulum or UX

Ursae Majoris sub-type of NLs because it shows different spectral characteristics at different epochs. This spectral behaviour suggests that EC21178-54 undergoes distinct variations in mass transfer rate on the observed time scales of months and years.

Acknowledgements

First and foremost, I wish to thank my supervisor A/Prof. Dr Patrick Alan Woudt, for all the help, support and guidance that I received from him for the past three years. You have given me the freedom to express myself and the way I feel, you have always encouraged me to do more and the best I could, and most of all, you have helped me beyond what I can ever thank you for throughout my MSc. Most of all I am greatly indebted to Prof. David Kilkenny and Dr Kurt van der Hyden, for the spectroscopy data. Your observations laid a solid foundation for this dissertation, without it this would have never been possible.

Thanks to Prof. Renèe Kraan-Korteweg, Chair of Astronomy and Head of the Astronomy Department, now Vice-President of the Executive Committee of the IAU, for welcoming me in the Department of Astronomy at UCT and providing me with the space to do my research. A/Prof. Saalih Allie and A/Prof. Thebe R. Medupe, for encouraging and believing in me. I would like to extend my gratitude to Em. Prof. Brian Warner*, who made me fall in love with CVs. To Mrs Nicoletta Bonitta Walker*, Mrs Rushana Fagodien*, Mrs Roslyn Matthews Daniels* (the mother) and Mrs Carol Marsh, thanks for all the support you have given me and I now know that I can always count of you.

I would also want to acknowledge the following people whose input has played a vital role in my dissertation: John Southworth (Keele University, UK), Sean February, Dr. Valerio A. R. M. Ribeiro, Enrico Kotze, and Mpati Ramatsoku*. Many thanks to my friends: Daniel, Osupeng, Papi, Siyambonga, Zolile, Mokhine and Toky, and my EHP kids (class of 2012 and the amazing class of 2013), for always being there for me. To Mrs Lesley Jennings, thank you for all the countless hours we spent in that tiny office editing and correcting my dissertation. Cheers to those who shared the office with me, thanks for always putting up with me. A big thank you to the Department of Astronomy staff as a whole for offering me the comforts and friendship when I was at UCT.

Thanks to the National Atrophysics and Space Science Programme (NASSP) and the National Research Foundation (NRF) for funding my Research while I was a student at UCT. Last but not least, I would like to thank my family (especially my Mom, brothers and sisters) and friends (in CPT and back at home), for all their love and support they showed throughout this study. This dissertation is dedicated to my father who passed away over a decade ago. I know you will be proud and I will always remember...
Above all I thank God for giving me the wisdom and strength to put this document together.

Plagiarism Declaration

I, Zwidofhelangani Ndamulelo Khangale, know the meaning of plagiarism and declare that all of the work in the document, save for that which is properly acknowledged, is my own.

Contents

List of Figures

List of Tables

Chapter 1

Introduction

1.1 Cataclysmic variables

1.1.1 Definition of cataclysmic variables

Cataclysmic variables (CVs) are interacting binary systems consisting of an electron degenerate star (a white dwarf primary) and a low-mass secondary star (normally a red dwarf). The secondary star is usually on or near the main sequence, rich in hydrogen, and transfers the material onto the white dwarf (WD) via an accretion disc. The separation between the two stars in CV binaries is very small (of order a million km), where the two stars are tidally locked together, with the secondary star always presenting the same face towards the primary. This results in the material closest to the primary experiencing a greater gravitational pull towards the primary, and moving towards the inner Lagrangian (L_1) point (see Figure 1.1). Consequently, the secondary star becomes distorted in shape, into a tear-drop-like structure. The effect of the gravitational field is shown in Figure 1.1, where the equipotential contours are drawn for a binary system with a mass ratio (q) of 0.5 (where $q = \frac{M_2}{M_1}$).

When the secondary star fills its Roche-lobe, the material starts to move through the L_1 point to the Roche-lobe of the primary. The Roche-lobe is the equipotential that contains the L_1 point where the net gravitational force is zero (Hellier 2001). Thus the apex of the Roche-lobe, L_1, is the easiest path by which material can transfer between the two stars. Mass transfer starts when the material from the secondary flows through L_1 and enters the Roche-lobe of the primary in a freefall (Lubow & Shu 1975) with the initial velocity (perpendicular to the orbital motion) close to the isothermal sound speed (c_s) in the gas. The material is then accelerated to high supersonic speed and misses the WD due to the deflecting Coriolis force. This fictitious force is due to conservation of angular momentum in a rotating frame. It follows that the material falling to the WD from L_1 cannot be easily accreted by the WD but instead moves in a circular orbit around the WD corresponding to its specific angular momentum (Roelofs 2007).

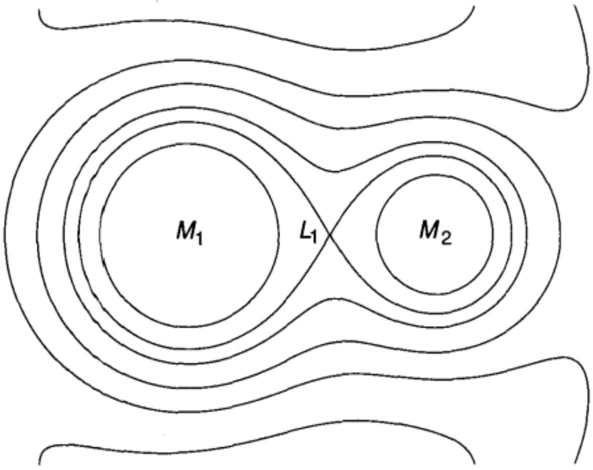

Figure 1.1: An example of contours of equal gravitational potential drawn for a typical binary with $q = 0.5$. (Adopted from Figure 2.3 of Hellier 2001).

The transferred material collides with itself at supersonic speed, heating up the gas to high temperatures, and radiating away the relative kinetic energy of the impact in the process. Angular momentum is conserved and, a small fraction of the initial angular momentum of the stream is lost to the secondary, a significant amount of energy is dissipated. This results in the formation of a ring of gas orbiting the primary at circularization radius (r_c) since a circular orbit has the least energy for a given momentum.

In order for an accretion disc to be formed, angular momentum must be lost and/or gained by the gas particles at r_c. First, the gas particles in a circular orbit at a distance r from the WD will have a Keplerian velocity given by

$$v_{K(r)} = \sqrt{\frac{GM_1}{r}}, \tag{1.1}$$

where M_1 is the mass of the accreting WD. Since the ring of gas has a finite radial thickness, Eq. (1.1) suggests that it should rotate differentially. Thus the evolution of the ring of gas depends on the nature of the angular momentum transport processes. However, if some form of viscosity is present, friction due to a shearing flow between adjacent Kepler orbits results (Spruit 2010). This results in the exchange of angular momentum between neighbouring Keplerian orbits. If angular momentum is increased, the ring moves to a larger radius. If, however, angular momentum is decreased, the ring moves to a smaller radius. In this way an accretion disc is formed by spreading the ring of gas inwards and outwards. The material that moves to the smaller orbits ends up being accreted by the WD, whereas the material that gains angular momentum causes the disc radius to increase.

1.1.2 Formation of cataclysmic variables

The origin of CVs is thought to be from two stars in a binary system in which one of the stars is more massive than the other. This larger star evolves faster since the stars on the upper main sequence (MS) obey the mass-luminosity relation, where the luminosity (L) scales roughly as $L \propto M^{3.5}$ (Ritter 2010). The consequence is that, for two stars with the same age but different in masses, the more massive star evolves faster. But since in this case they are in the binary system, the presence of the second (less evolved) star limits the extent to which the more massive star can expand to its Roche-lobe, without losing mass.

The more massive star (star 1) converts its hydrogen faster than its companion (star 2) and evolves to the red giant phase first. As a consequence, the outer layers of star 1 will expand and contain the orbit of star 2, resulting in the formation of a common-envelope phase in which star 1 and star 2 are in deep contact. The increased pressure and friction on star 2 causes angular momentum to be transferred from star 2 to the expanded outer layers of star 1, and causes the ejection of the outer layers of star 1 into the interstellar medium forming a planetary nebula (Ritter 2010). The post common envelope binary is now a detached short period system consisting of a WD and a red dwarf (star 2). This phase in its evolution is called the pre-CV phase.

Orbital decay due to further loss in angular momentum is required to form a CV. This can happen due to either magnetic braking (Verbunt & Zwaan 1981, Rappaport et al. 1983) or gravitational radiation (Faulkner 1971, Paczynski & Sienkiewicz 1981). Gravitational radiation is irrelevant in the case of CVs with longer periods, but is more effective in short-period systems with orbital period less than 2 hours. Magnetic braking requires a strong stellar wind and strong magnetic field of the secondary (star 2) to be effective. The magnetic field of the secondary star serves as a mechanism for extracting angular momentum from the binary via the field lines and thus reducing the orbital period of the binary. This angular momentum loss (AML) slows down the rotation of the red dwarf and consequently shrinks the orbit to smaller radii resulting in the formation of a CV. However, mass transfer does not start until the separation becomes small enough for material to be transferred from the secondary star to the WD via the Roche-lobe.

1.1.3 Evolution of cataclysmic variables

The best way to describe the evolution of CVs is via the period distribution diagram shown in Figure 1.2. Note that the orbital period (P_{orb}) is often the only quantity that we know for a large population of CVs, whilst their component masses are only known for a very small number of CVs. However, much of the work of the past 30 years has been dedicated to understanding the period distribution of CVs. The period distribution diagram (Figure 1.2) shows many systems having orbital period ranges between 3 h and 6 h, and 80 min and 2 h, but very few of them with orbital periods between 2 h and 3 h. The period range between 2 and 3 hours is known as the period gap. Different models were proposed in order to explain the distribution of CVs shown in Figure 1.2, and we discuss two of the best models in the next paragraphs.

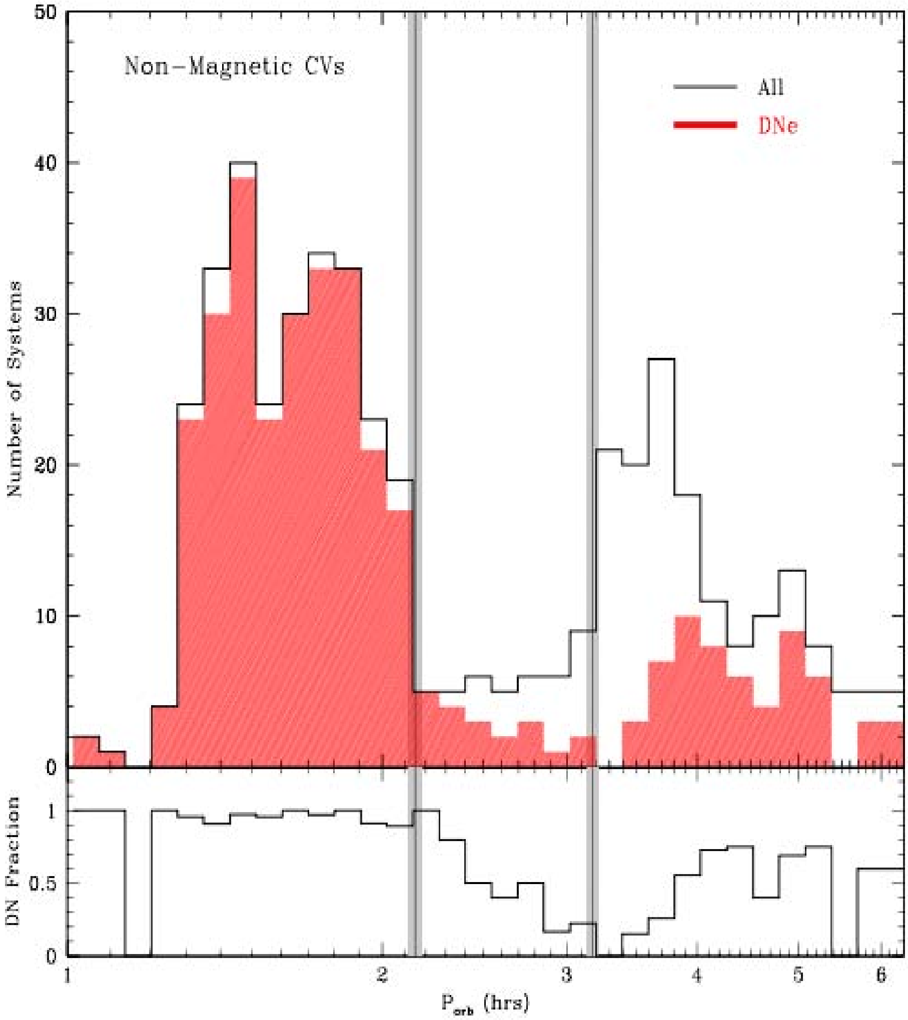

Figure 1.2: Orbital period distribution of non-magnetic CVs and their associated dwarf novae fraction in the Ritter & Kolb (2003) catalogue version (7.11). (Adopted from Figure 18 of Knigge et al. 2011).

Mass transfer in CVs is driven by AML due to magnetic braking (Verbunt & Zwaan 1981) above $P_{\rm orb} = 3$ h and gravitational radiation (Kraft et al. 1962) below $P_{\rm orb} = 2$ h. The model of disrupted magnetic braking (Spruit & Ritter 1983, Rappaport et al. 1983) was adopted as the "standard model" of CV evolution for decades, because it explained most of the features observed in the period distribution diagram. This model explains the scarcity of systems in the period gap by explaining that the donor star becomes fully convective when it reaches $P_{\rm orb} \simeq 3$ h, and consequently magnetic braking will stop operating. At this stage the donor star is driven a little out of thermal equilibrium (TE) and is therefore slightly larger. As a result, the mass transfer rate is reduced, and the donor star contracts thereby losing contact with the Roche-lobe. The system then evolves towards shorter periods as a detached binary, with mass loss driven only by gravitational radiation (GR). But when the binary system reaches $P_{\rm orb} \simeq 2$ h, the Roche-lobe eventually catches up with the donor star and mass transfer resumes.

The existence of a period spike at the period minimum, $P_{\rm min} \sim 80$ min (Gänsicke et al. 2009), is accounted for as the result of mass transfer from a hydrogen-rich donor which is driven mainly by GR (Paczynski & Sienkiewicz 1981, Rappaport et al. 1982). The sharp cut-off at $P_{\rm min}$ is explained by the donor star being driven out of TE until it reaches a point where its radius can shrink no further in reaction to mass loss. This results in increased size of the binary orbit in order to accommodate the (now partially degenerate) donor star and leads to a change in the direction of the system's evolutionary period. The systems that have evolved beyond $P_{\rm min}$ towards longer periods are called period bouncers. Thus $P_{\rm min}$ should be seen clearly as a narrow spike with sharp, short-period cut-off, and not as a sudden decrease in numbers. The problem with the standard model is that it predicted more short-period and period bounce systems around $P_{\rm min}$. Also the earlier version of period distribution diagrams showed roughly equal number of systems below and above the period gap (Figure 4.1 of Hellier 2001). This has changed recently with more systems being found below the period gap and a significant amount of CVs clustering around $P_{\rm min}$. The other problem with this model is that it predicted that the minimum period should be around $P_{\rm min} = 65$ min, but this is shorter than the observed $P_{\rm min}$. Knigge (2006) estimated the value of $P_{\rm min} \approx 75$ min, and recently Gänsicke et al. (2009) located the period spike at $P_{\rm min} \simeq 82$ min from the Sloan Digital Sky Survey (SDSS) sample which made the standard model even more unsatisfactory.

Recently Knigge et al. (2011) proposed a new evolutionary model for CVs based entirely on the properties of the donor star, hereafter "the best-fit model". This best-fit model was first described and developed by Knigge (2006), and further improved in Knigge et al. (2011). The best-fit model predicts a lower percentage of short period, pre-bounce CVs, and a significantly higher percentage of period bouncers. Knigge et al. (2011) located the position of the period minimum at $P_{\rm min} \approx 81.8 \pm 0.9$ min (see Figure 1.2), in excellent agreement with the observed location of the period spike from the sample of CVs in the SDSS, 82.4 ± 0.7 min (Gänsicke et al. 2009). According to the best-fit model, the upper gap edge occurs at $P_{\rm gap,+} = 3.24 \pm 0.05$ h, whereas the bottom edge of the period gap is found at $P_{\rm gap,-} = 2.15 \pm 0.03$ h, both in excellent agreement with the observed location of the gap edges above and below the period gap (see Knigge 2006). In addition, Knigge et al. (2011) find consistent results when comparing the spectral types of the donor stars to those of the MS stars. The mass-losing stars were always found at longer orbital periods and inflated radii compared to the equivalent Roche-lobe-filling MS star in TE.

It is clear from Figure 1.2 that short-period CVs are basically dominated by dwarf novae, but this drops through the period gap, reaches a minimum just before the upper gap edge, and then rises again towards $P_{\mathrm{orb}} \approx 4$ h. The nova-likes exist both above and below the period gap, but dominate the CV population above the period gap.

1.2 Dwarf nova outbursts and nova-likes

1.2.1 Accretion discs in cataclysmic variables

In Section 1.1.1, we have seen that the material falling into the Roche-lobe of the primary will have sufficient angular momentum to form an accretion disc before the material is accreted by the WD. Some form of viscosity is needed to transport angular momentum between adjacent orbits, and drive accretion through the disc.

The accretion discs in CVs are long and thin, so that the molecular viscosity is negligible (Pringle 1981). Thus the term viscosity refers to any processes that transport angular momentum in the accretion disc. Lynden-Bell (1969) brought forth the idea of viscosity as the energy transport mechanism in the accretion discs of quasars. Shakura & Sunyaev (1973) parameterized the viscosity (ν_K) as

$$\nu_K = \alpha c_s H, \tag{1.2}$$

where α denotes the size of the viscosity as a fraction of the limiting case, and $\alpha < 1$, c_s is the sound speed and H is the vertical height of the disc. Eq. 1.2 is called the α-prescription for disc viscosity and was used to develop accretion disc models. These discs are called "alpha discs". They are thin discs, where the height of the disc is very small compared to the radius of the disc. Kotko & Lasota (2012) found that $\alpha \sim$ 0.1-0.2 in an ionized dwarf novae accretion disc.

The most probable cause for viscosity in the accretion disc is magnetic turbulence (see Lynden-Bell 1969), and this can be included in the α-prescription (Shakura & Sunyaev 1973). The theory of magnetic turbulence in the accretion disc was developed by Hawley & Balbus (1998). It suggests that turbulence in the accretion disc arises from the instabilities in the magnetic field. This is simply the enhancement of the magnetic field between adjacent bubbles at different radii, which result in the breaking-up of flow into turbulence. This process is called the Balbus-Hawley instability, and requires a strong pairing between the magnetic field and the disc material, which can only occur when the disc is hot and ionized. The problem with the magnetic turbulence model is that electrons can recombine with nuclei to form neutral atoms when the disc is in the cold state and completely stops the Balbus-Hawley instability. The outbursts in dwarf novae, however, can only be explained by a mechanism that is able to flip the disc between hot and cold states.

The interaction between the secondary star and the accretion disc around the WD may also cause angular momentum to be transported in the accretion disc through tidally-induced spiral waves. These shock waves may provide an angular transport mechanism, since the material passing through them will lose angular momentum and energy. But this happens during the high states in dwarf novae when the accretion disc radius has expanded and comparable to the tidal radius. The presence of tidally induced spiral structures was first noted by Sawada et al. (1986) in the two-dimensional (2D) numerical simulations of the accretion disc of CVs. But this lacked observational evidence for at least a decade, until Steeghs et al. (1997) found two arc-like structures in the Doppler maps of IP Pegasi (IP Peg). These were interpreted as the proof of the spiral shock waves in CVs. The problem with this interpretation is that the observed spiral structures were not symmetric, whereas the 2D hydrodynamic spiral wave models predict perfectly symmetrical waves. This was later resolved in the Smak (2001) model, based on the simple mechanically restricted three body approximation, which explains the presence of the asymmetrical waves as well as the asymmetry of the structures seen in Doppler maps of CVs.

1.2.2 Dwarf nova outbursts

Dwarf nova outbursts correspond to rapid increase in the brightness of a dwarf nova by 2-6 magnitudes or more in a period of a day or so, lasting up to 20 days before declining back to quiescence. These outbursts have recurrence timescales of about 20-300 days, e.g. the outbursts in U Geminorum (U Gem) repeat on average after every 100 days, while those of SS Cygni (SS Cyg) repeat on average every 50 days (Hellier 2001). Dwarf nova outbursts are divided into two types: normal outbursts and superoutbursts. The normal outbursts are narrow, last no longer than 20 days, and have amplitudes not greater than 6 mag, and no superhumps (low-amplitude brightness variations) are observed. Superoutbursts are brighter, last longer than normal outbursts, and superhumps are seen during the process (see Osaki 1996).

It is well understood that dwarf nova outbursts are caused by a sudden brightening of the accretion disc which result in the rapid increase in the mass transfer rate onto the surface of the WD. Two models were proposed in the 1970s to explain the non-steady accretion onto WD: the mass-transfer instability model (Bath 1969, 1972, 1973), and the disc-instability model Osaki (1974). These two models competed until Hōshi (1979) discovered a mechanism responsible for disc instability. He found that the accretion-disc theory allows double solutions in the outer parts of the accretion discs: the low-viscosity optically thin cool disc where hydrogen is neutral, and the high-viscosity hot disc where hydrogen is fully ionized. This was further developed into a thermal instability model by Meyer & Meyer-Hofmeister (1981) by including convective transport of energy while solving the vertical structure of the accretion discs. The most recent review of the thermal-instability model is given by Osaki (2005).

The thermal instability model explains the outbursts of dwarf novae based on the S-shaped thermal equilibrium curve (see Figure 1.3). The ionization of hydrogen occurs at temperature of $\sim 10^4$ K. Consider the mass transfer rate through the accretion disc, $\dot{M}_d$. This is set by the viscosity value, and in general this value will not be equal to the value of the mass transfer rate from the secondary, $\dot{M}_2$. Thus if $\dot{M}_2 > \dot{M}_d$, material will be accumulated

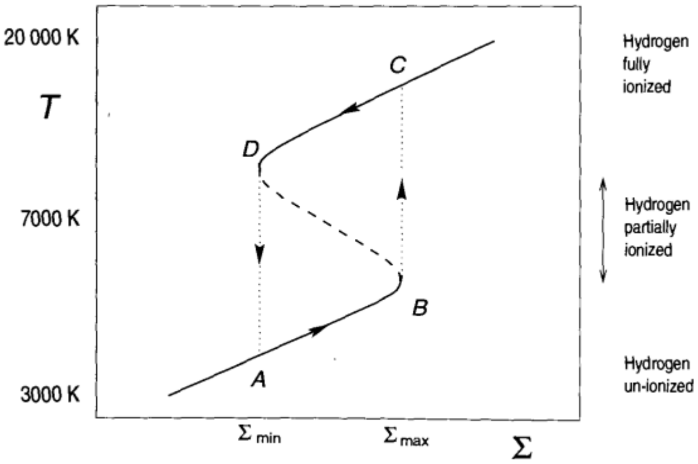

Figure 1.3: Disc temperature-surface density ($T-\Sigma$) diagram showing the limit cycle S-curve followed by a dwarf nova. (Adopted from Figure 5.7 of Hellier 2001.)

in the accretion disc. Figure 1.3 is explained by first considering a disc annulus with T $\approx$ 4000 K (at point A). If $\dot{M}_2 > \dot{M}_d$, more material will be dumped onto the disc and build up, resulting in the increase of surface density ($\Sigma = 2\int \rho dz$, where ρ is the volume density and z is the direction perpendicular to the orbital plane), viscosity, and the temperature of the annulus along path A towards B until some surface density, $\Sigma_{\rm max}$, is reached. At point B (T $\approx$ 5000 K) the material is partially ionized, and the increase in temperature causes a huge increase in opacity. At point B the opacity is higher than at point A, and more energy goes into heating the gas which in turn causes a further increase in the opacity of the disc. However, the surface density increases at a slower pace until it reaches $\Sigma_{\rm max}$, and the further increase in temperature causes the new equilibrium state to be reached, point C. At this high state the gas is completely ionized (T $\approx 10^4$ K), and the opacity drops due to higher temperature and viscosity. Consequently, the $\dot{M}_d$ is greater at point C and the luminosity of the system increases. The material is drained slowly along path C-D due to increased $\dot{M}_d$, reducing viscous heating. At point D, the material is again partially ionized, but the Σ is reduced to $\Sigma_{\rm min}$, and high opacity returns; while reduced energy results in the drop in temperature and viscosity in the disc. The ions recombine and the disc changes from its high state through path D-A, returning to the quiescent low viscosity state. This happens in such a way that the instability in one disc annulus causes instability in another. The higher viscosity spreads hot material from one disc annulus to the next, resulting in a heating wave spreading throughout and sending the whole disc into outburst.

The evolution of the outburst depends on the distribution of material in the disc when the instability was first triggered, as well as on the radius at which the outbursts start. At low $\dot{M}_2$, the material is attracted inward, causing a build-up at small radii. Thus the Σ reaches $\Sigma_{\rm max}$ in the inner disc first, causing the inside-out outburst. This occurs if the instability was first triggered in the inner part of the accretion disc, where the heating front propagates from the inside to the outside. But, if $\dot{M}_2$ is higher, the material does not have enough time to diffuse inwards, thereby accumulating at larger radii and triggering the instability in the outer disc, which results in the outside-in outburst. This happens if the instability was first triggered in the outer part of the accretion disc, and the heating front propagated from the outside to the inside (Smak 1984). The increased accretion onto the WD drains the disc of its material until Σ is reduced to $\Sigma_{\rm min}$ at some annulus in the outer disc, since $\Sigma_{\rm min}$ is highest there. This annulus drops out of the outburst and spreads the cooling wave to adjacent annuli which in turn drops out of the outburst. The cooling wave propagates inwards returning the whole disc to a quiescent state (Hellier 2001).

1.2.3 Optical spectroscopy of cataclysmic variables

In this section we review the general spectral characteristics of non-magnetic CVs (i.e., dwarf novae and nova-likes). Optical spectra of most CVs characteristically show emission lines from the low ionization states, e.g. Balmer lines, HeI, HeII, CaII, FeII lines, and CIII and NIII blend at 4650Å (the Bowen blend). The other elements are too weak to be detected in the spectra of CVs due to line broadening caused by disc rotation. The different ionization states of these lines indicates that they are produced in different regions: the WD, secondary star, the accretion disc, the bright spot, and from the chromosphere. For example, the equivalent width of HeII 4686Å in dwarf novae increases during outbursts due to large increase in HeII flux from the expanded accretion disc, whereas the flux of Balmer lines remains unchanged.

The spectra of dwarf novae (DNe) in low state are characterized by strong Balmer emission lines on a blue continuum, and weak emission from HeI, HeII lines, and other heavier elements. These stars show shallow or negative Balmer decrement, indicating optically thick conditions (Warner 1995). In addition, the ratio of H_β to HeII 4686Å is always much larger than unity, and the Bowen blend is always weak or absent. But in cases where the WD contribute much to the optical light, its broad absorption lines are seen as shallow troughs on either side of the Balmer emission lines.

DNe during outbursts are simply recognized by the transition from mostly emission-line to mostly absorption-line spectra. But in most DNe, the emission cores appear with narrower widths than the emission lines at quiescence. Some systems shows no change in the Balmer emission flux from low state to high state, e.g. SU UMa . Thus the spectra of DNe in outbursts exhibit different behaviours from star to star which repeat on different outbursts of the same object (see Warner 1995, for more details). The strength of HeII 4686Å is enhanced during outbursts, whereas that of the Balmer lines is reduced. Furthermore, most DNe during outburst show emission from the heated face of the secondary star which is revealed by comparing the radial velocity curves of the primary with that of the secondary. This becomes more clear in the Doppler maps and a luminous spot is always seen in the position of the secondary star, e.g. IP Peg (Harlaftis et al. 1999).

Nova-likes on the other hand, show no outbursts at all but they occasionally show low

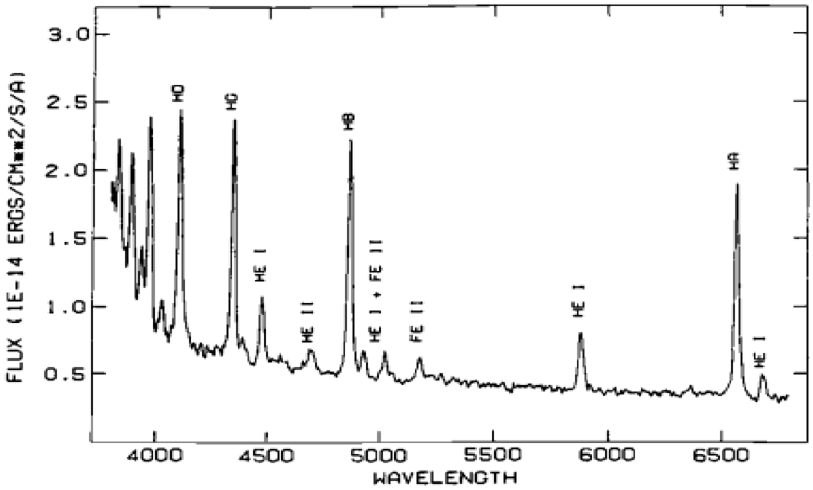

(a) YZ Cancri in quiescence. (Adopted from Figure 2(c) of Shafter & Hessman 1988).

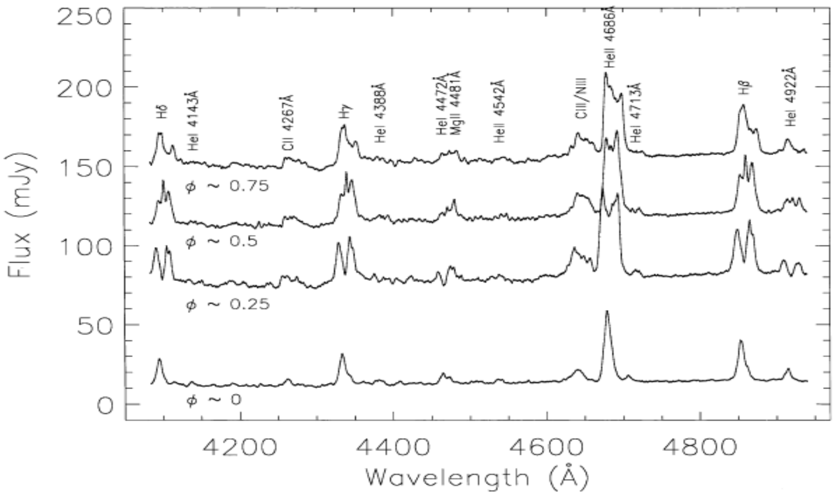

(b) IP Peg in outburst. (Adopted from Figure 2 of Morales-Rueda et al. 2000).

Figure 1.4: Examples of the spectra of dwarf novae in (a) quiescence and (b) outburst.

and high states. Their optical spectra shows a variety of spectral characteristics varying from broad and shallow Balmer and helium absorption lines with superimposed emission through pure weak emission of Balmer, HeI, HeII lines and Bowen blend to strong emission of Balmer and HeII lines, and Bowen blend (see Figures 1.5 to 1.8). In general, the optical spectra of NLs show signs of higher excitation conditions, e.g. HeII 4686Å and CIII/NIII are stronger than those in DN. The ratio between HeII 4686Å to H_β is mostly always greater than unity. The low excitation lines seen in DN are also present in the spectra of NLs but with additional weak lines (see Table 4.3 of Warner 1995). But FeII emission is absent in the spectra of NLs. Most NLs show little or no evidence of the emission-line S-wave from the bright spot even where there is clearly a bright spot continuum affecting eclipse profiles. Their high disc luminosity makes it difficult to detect any spectra from the secondary, even in high inclination systems. Nova-likes have optically thick discs.

From the above discussion, it is clear that optical spectral features of nova-likes are very similar to those observed in DNe during quiescent and outburst state. Low-inclination nova-likes show strong absorption-line spectra that are similar those seen in low-inclination DNe during outbursts (see Figure 1.5). In addition, high-inclination nova-likes show strong emission-line spectra that are very similar to those observed in high-inclination DNe during outbursts. Thus there is no significant difference in the spectra shown in Figure 1.4 compared to those shown in Figures 1.5 to 1.8. The differences arises from the different components of the binary system that are visible in optical light as well as due to the inclination of the system. The spectrum of the WD shows broad absorption lines in the blue continuum, whereas the red dwarf spectra shows wide and complex absorption features in the red wavelengths. Both the WD and the red dwarf are sometimes seen in spectra of DNe during quiescence, and almost impossible to detect in DNe during outbursts and most nova-likes.

The spectra from the accretion disc is flatter and most spectral features are often in emission, and they change states from optically thick to optically thin conditions. But at some stage an accretion disc can be both optically thin and optically thick. This is supported by the existence of both absorption and emission due to an accretion disc which is optically thick and also surrounded by optically thin corona. The optical spectra of DNe and nova-likes are dominated by emission and absorption lines from the accretion disc and are seen as double-peaked profiles in which the peaks are shifted from the line centre by the velocity typical of the outer disc. Since the disc is centred on the WD, the whole double-peaked follows as S-wave with the WD. But during eclipse, the blueshifted peak is eclipsed first followed by the redshifted peak.

The other component that contribute much to the optical light is the brihgt spot, defined as the the impact point between the stream of materials from the secondary and the outer rim of the accretion disc. The impact create a shock-heated area that radiate as much or more energy at optical wavelengths as all the other components (i.e., primary, secondary and accretion disc). Its position is determined by the intersection of the stream trajectory with the outer edge of the accretion disc (see Warner 1995). The bright spot is responsible for most of optical light we see in CVs and hence the emission lines observed in their spectra. It appears at phases 0.7 to 0.95 for eclipsing systems and contribute much light in quiescence DNe. It is visible in quiescent DN, and also follows an S-wave as its position vary with the orbital phase. But it is difficult to detect in high state DN and nova-likes.

1.2.4 Nova-like stars

Nova-likes (NLs) are disc-dominated CVs characterized by a higher mean mass transfer rate with nearly constant accretion luminosity, and are, unlike most other CVs, almost always observed in the outburst state (Noebauer et al. 2010). Thus NLs are like DN in outburst. Their absolute magnitudes are also similar to those of DN in outbursts (Patterson 1984, Warner 1987). NLs have orbital periods just above the period gap in non-magnetic CVs (see Figure 1.2), where magnetic braking is thought to reproduce the largest mass transfer rates in the long-term evolution of CVs (Howell et al. 2001). However, there are NL systems that are found below the period gap, e.g. BK Lyncis[1] (Patterson et al. 2013).

NLs show short timescale spectroscopic and photometric variability that is similar to those of DN between outbursts. Optical spectra of NLs show a wide range of distinctive features which varies from wide, shallow Balmer and helium absorption lines with superimposed weak emission to strong emission of H, HeII and CIII/NIII (Warner 1995). These features depend on a variety of conditions, such as the temperature of the WD, inclination angle, and $\dot{M}_2$. Based on their spectroscopic and photometric behaviour, NLs are classically divided into four distinct sub-types: UX Ursae Majoris (UX UMa), RW Triangulum (RW Tri), SW Sextantis (SW Sex), and VY Sculptoris (VY Scl).

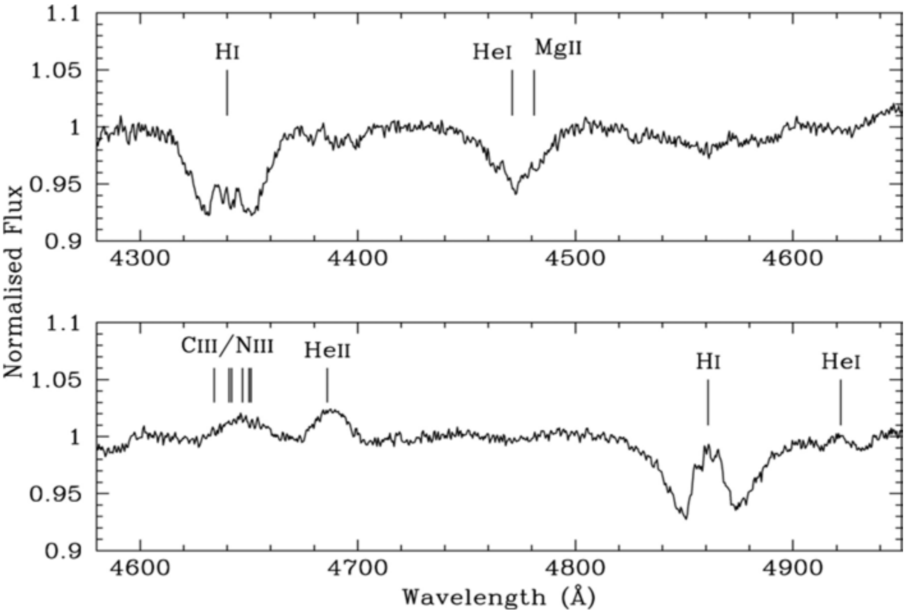

Figure 1.5: The average blue spectrum of V3885 Sagittarius (top and bottom panels). (Adopted from Figure 1 of Hartley et al. 2005).

UX UMa stars are non-eclipsing binaries that are generally of low inclination. Their optical spectra sometimes show pure absorption-line profiles containing the Balmer lines, HeI lines and CaII lines with no signs of the high excitation features (HeII 4686Å and the CIII/NIII blend at 4650 Å). These features are seen when the Balmer lines become strong. UX UMa spectra show a steep Balmer decrement and sometimes this result in H_α being seen in pure emission with the rest of the Balmer series showing strong progressive absorption

---

[1] BK Lyncis is a nova-like variable with an orbital period of 108 min discovered in the Palomar-Green (PG) survey (Green et al. 1986), and was listed as PG 0917 + 372 in the early compilation of the PG survey (Green et al. 1982).

troughs. The spectra of UX UMa stars show broad and shallow absorption from an optically thick disc (see Warner 1995). Figure 1.5 shows a typical UX UMa spectra: both absorption and emission lines are present. Emission is due to the presence of the accretion disc and bright spot, and absorption account for low-inclination and optical thick conditions.

RW Tri stars have light curves that show deep and variable eclipses, and their brightness varies intrinsically between eclipses (see Winkler 1977, and references therein). The deep eclipses in RW Tri stars is evidence or implication of high inclination. Optical spectra of RW Tri stars show pure emission from the Balmer lines and HeII lines. CII is seen when the system is out-of-eclipse, whereas the CIII/NIII blend at 4650 Å is barely detectable. But, during eclipse, the strength of HeII and CII lines are reduced suggesting that these lines originate from near the WD or the inner disc (Warner 1995). Figure 1.6 shows the average spectrum of RW Tri: it is a pure emission-line spectrum at all phase, typical of a high-inclination system with disc emission. But there are absorption features in the top spectrum most noticeable in the blue below 4000Å: this is caused by the bright spot which is visible at phases 0.75 to 0.95 (see figure 14 of Groot et al. 2004).

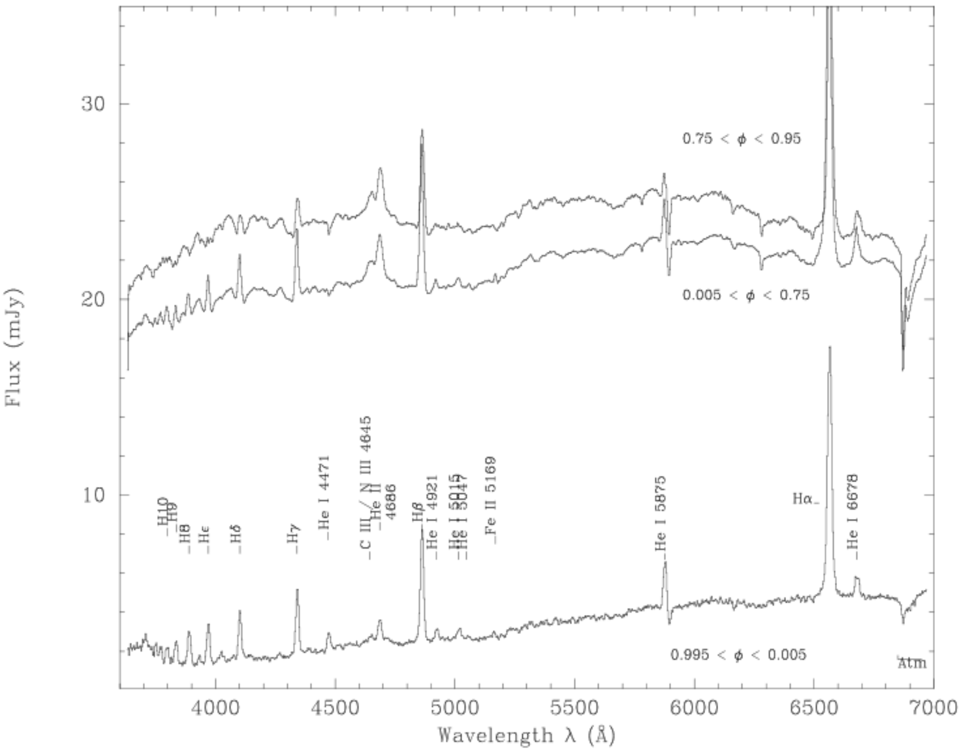

Figure 1.6: The average spectrum of RW Tri at three different phase intervals. (Adopted from Figure 2 of Groot et al. 2004).

SW Sex was originally defined over two decades ago as an eclipsing system, and which showed common but inexplicable properties (Szkody & Piche 1990, Dhillon 1990, Thorstensen et al. 1991). But recently, large numbers of lower-inclination and non-eclipsing SW Sex stars have been found, contributing about half of the SW Sex population, which demand revision of the original membership criteria (Rodríguez-Gil et al. 2007a,b, Dhillon et al. 2013). SW Sex stars have periods in the range 2.8 h $\leq P_{\rm orb} < 4$ h (Gänsicke 2005, Schmidtobreick et al. 2012). The light curves of eclipsing SW Sex stars show deep continuum eclipses, implying a high-inclination accretion disc. The optical spectra of SW Sex stars show single-peaked emission lines profiles in the Balmer and HeI lines, superimposed on the emission lines is a transient narrow absorption feature that is seen around phase 0.5 (Warner 1995). The low excitation lines (H and HeI) suffer little or no eclipse at phase zero, whereas the higher excitation lines (HeII, CIII/NIII, and CII) are single-peaked at all phases and are almost totally eclipsed at phase zero. SW Sex stars have bright accretion discs, and in some cases they show occasional VY Scl-type low states. In addition, SW Sex stars show large phase lags ($\sim 70°$) in the radial velocity curves of both high and low excitation lines relative to the photometric ephemeris (Warner 1995). Figure 1.7 shows a typical spectrum of SW Sex with single-peaked emission in the Balmer, HeI and HeII lines, as well as the Bowen blend.

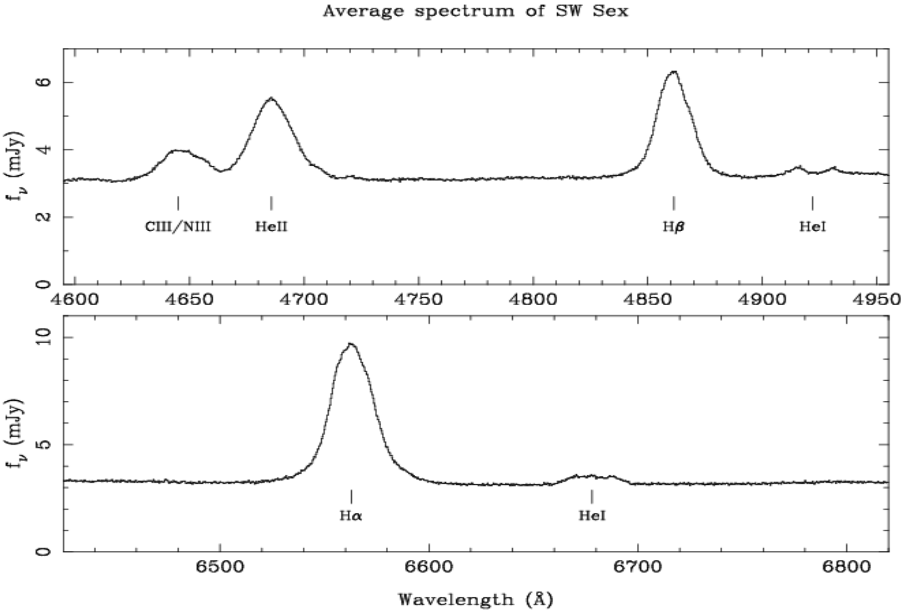

Figure 1.7: The typical average blue and red spectrum of SW Sex star (top and bottom panels). (Adopted from top panel of Figure 1 of Dhillon et al. 2013).

VY Scl stars were defined based on their photometric behaviours and are non-eclipsing and bright magnetic NLs which occasionally undergo a decrease in brightness of more than one magnitude, which seems to arise from the decrease in mass-transfer rate (Lasota & Hameury 2004). No outbursts are observed in VY Scl stars, and their light curves show no activity at all during descents and rises. However, their low states are sometimes interrupted by epochs of activity which their characteristic timescales are much longer than those of the thermal-viscous instability timescales that operates in DNe. These stars at maximum light resemble those of UX UMa, RW Tri, or SW Sex. During low states, their broad accretion disc optical lines are replaced on the blue continuum by very narrow strong Balmer emission and weaker HeI and HeII emission lines in their optical spectra. Figure 1.8(a) shows an example of a VY Scl-type star in a low state (DW Cnc), with strong narrow Balmer emission lines. But during high states, their optical spectra show narrow Balmer emission lines in the cores of broad and shallow absorptions, as well as emission from HeI, HeII and the CIII/NIII blend. An example of VY Scl in a high state is shown in Figure 1.8(b), with the Balmer emission lines in the cores of broad and shallow absorption.

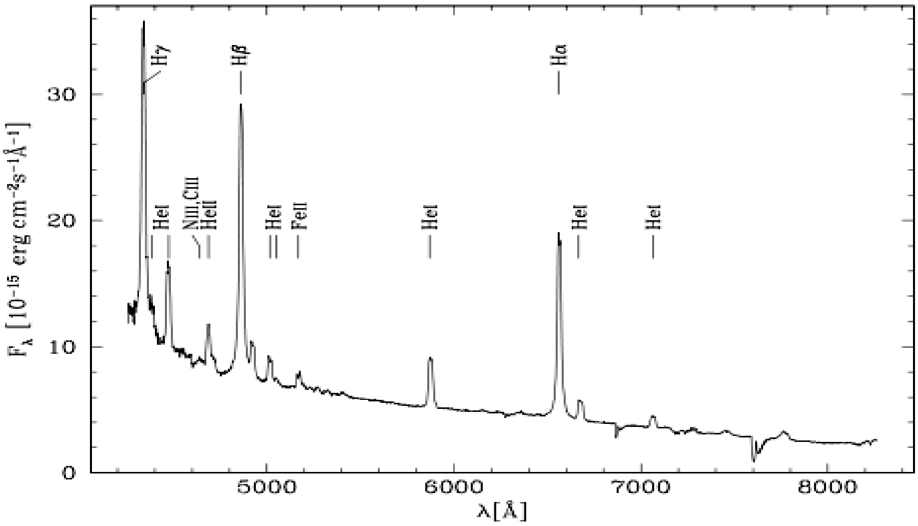

(a) DW Cancri during low states. (Adopted from Figure 5 of Rodríguez-Gil et al. 2004).

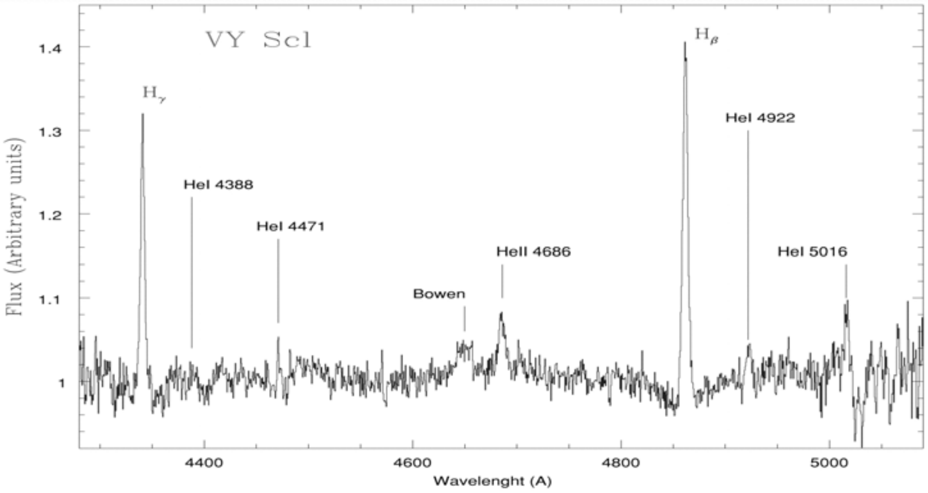

(b) VY Scl during high states. (Adopted from Figure 1 of Martínez-Pais et al. 2000).

Figure 1.8: Typical spectra of VY Scl stars: (a) DW Cancri in low state and (b) VY Scl itself in high state.

This classification of NLs is still valid today, but Dhillon et al. (2013) proposed a simplified classification for NLs base on the variation in mass transfer rate ($\dot{M}_2$). They suggest that all NLs should just be referred to as UX UMa stars. This is based on some of the observational characteristics seen in NLs. Individual UX UMa stars have now been found to show different behaviour from one observation to the next due to the change in mass transfer rate at the time of observation, e.g. DW UMa (Dhillon et al. 1994, 2013). Secondly, UX UMa itself was shown to exhibit some SW Sex-like behaviour (Neustroev et al. 2011). In addition, the majority of non- or weakly magnetic CVs in the orbital range 2.8 h $\leq P_{\rm orb} \leq$ 4 h belong to the SW Sex sub-class and, as such, experience a higher rate of mass transfer (Rodríguez-Gil et al. 2007a, Schmidtobreick et al. 2012).

Since CV evolution is governed by AML which results in the decrease of the orbital period in evolutionary time scales, all long-period CVs need to cross the SW Sex regime of the orbital period distribution before reaching the period gap. Schmidtobreick (2013) proposed that the SW Sex phenomenon must be an evolutionary stage in the life of a CV. Finally, the difference between UX UMa and RW Tri stars is largely a matter of inclination. Therefore, Dhillon et al. (2013) propose that all non-magnetic NLs should be called UX UMa stars (excluding AM CVn systems). Since some UX UMa stars show low states which look like VY Scl stars, they should be referred to as VY Scl stars. On the other hand, some UX UMa stars show SW Sex characteristics, in which case they should be referred to as SW Sex stars. Hence a UX UMa star can be either a VY Scl star or an SW Sex star.

1.3 Doppler tomography of cataclysmic variables

Doppler tomography is an indirect imaging technique that has been used for almost thirty years in a wide range of systems containing a compact and non-compact object. The application was first implemented in the late 1980s by Keith Horne and Tom Marsh (Marsh & Horne 1988), and has found use in a wide range of astrophysical objects, including CVs, X-ray, and gamma-ray binaries, to produce 2D images of the accretion structures.

The dynamics of the accretion flow provides a direct kinematic signature of the accreting structure (Marsh & Horne 1988). Observing line profiles at each orbital phase provides a projection of the accretion flow along the line of sight and, given sufficient observed projections, these profiles can be inverted into a 2D image. It is from these images that evidence is revealed of the gas stream from the donor star; of symmetric and asymmetric accretion disc; of bright spot (shocked regions) where the stream impacts the accretion disc; of magnetic structures associated with the secondary; and of gas flowing along the magnetic field lines on the WD. Figure 1.9 shows the Doppler map of CE 315 with various components such as the bright spot and accretion stream labelled.

The following five assumptions are made when performing Doppler tomography (Steeghs 2003):

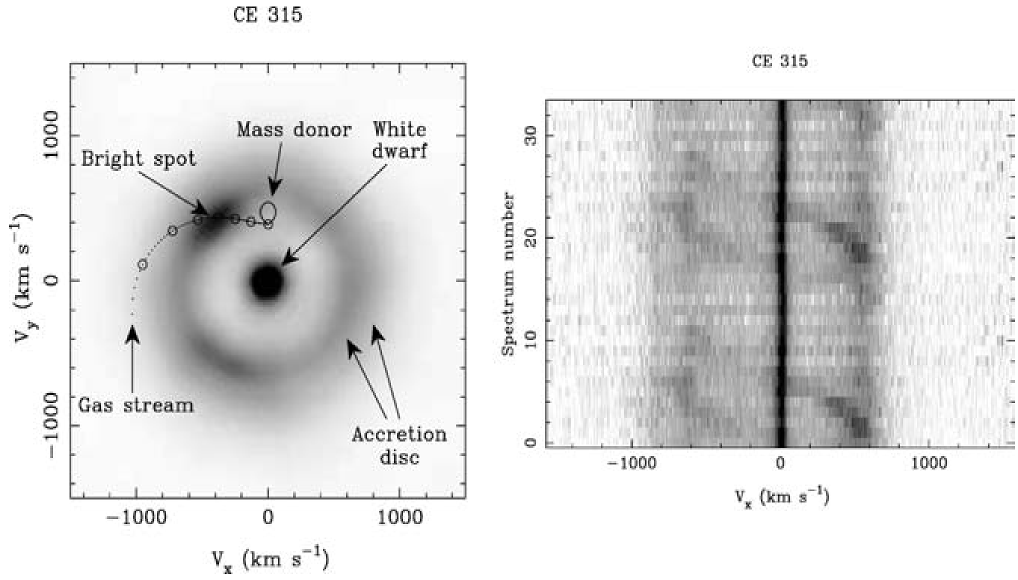

Figure 1.9: An example of a Doppler map showing various components of the binary system. (Adopted from Figure 3 of Marsh 2005).

1. the intrinsic line profile width is negligible;
2. all velocity vectors co-rotate in the binary;
3. motion is mapped parallel to the orbital plane only;
4. all points are equally visible at all times;
5. the flux from any point is constant in time.

These assumptions must be taken into consideration when interpreting the reconstructed accretion flows. In the Doppler map coordinate frame, each emission line source is described by its inertial velocity vector in the orbital plane, $\mathbf{V} = (V_x, V_y)$, where the binary centre of mass is at the origin, the x-axis points from the WD to the secondary, and the y-axis points in the direction of motion of the secondary, as viewed in the co-rotating frame of the binary.

In Eq. 1.3, $V(\phi)$ describes the velocity as a function of orbital phase (ϕ), where γ is the systemic velocity of the binary

$$V(\phi) = \gamma - V_x cos2\pi\phi + V_y sin2\pi\phi, \tag{1.3}$$

where $\phi = 0$ is defined as the time when the donor star is closest to us (i.e., during mid-eclipse for eclipsing binaries). The observed line profiles are the projection of the radial velocities (v_r) and intensities of all velocity vectors considered:

$$F(v_r, \phi) = \int I(V_x, V_y) * g(V - v_r) dV_x dV_y, \tag{1.4}$$

where $g(V - v_r)$ describes the local line profile intensity at a Doppler shift of $V - v_r$, $I(V_x, V_y)$ is the image value (intensity) of the Doppler map at the corresponding velocity grid point, and (dV_x, dV_y) is the width of each velocity element. The inversion from data-set to Doppler map is achieved by regularized fitting using the maximum entropy method or a similar quantity as the regularizing function (Marsh & Horne 1988).

A violation of any of the five assumptions mentioned above does not suggest that Doppler tomography cannot be performed, or that the maps are meaningless. See Steeghs (2003) for an example where the last of these assumptions was modified to allow a flux modulation applied to IP Peg. This technique has also been applied in the X-ray nova XTE J1118+480 (Calvelo et al. 2009) and IP Peg (Papadaki et al. 2008).

1.3.1 The Fast Maximum Entropy method

There are three method that can be used to obtain Doppler maps namely: the Fourier-filtered back-projection (Rowland 1979), the Maximum Entropy Method (MEM) developed by Marsh & Horne (1988), and the Fast Maximum Entropy Method (FMEM) code written by Spruit (1998). The most commonly used Doppler tomography method is the Fourier-filtered back-projection, not only because it is fast but because it is very easy to implement. The disadvantages of using the Fourier-filtered back-projection is that it produces noticeable artifacts in the form of "radial spokes" in the Doppler maps. The best Doppler maps are achieved by implementing the MEM method, but its implementation is slow and only small maps can be processed. The FMEM method uses the fast algorithm and solves the same maximum entropy problem. It derives from the Richardson-Lucy maximum-likelihood algorithm, but solves a different problem (Spruit 1998). This code has been used to produce the Doppler maps of many other CVs, e.g. WZ Sge (Spruit & Rutten 1998) and it is the code I have used to create the Doppler maps of EC21178-54 (Section 4.4).

Spruit (1998) made five assumptions similar to those by Steeghs (2003), previous section, when developing the FMEM code. The method take Cartesian coordinates $v = (v_x, v_y)$ in space describing the velocity of the material in the orbital plane (x, y). It separates this in velocity space into bins of size $(\Delta v_x, \Delta v_y)$. Each bin numbered $j = 1...m$ has an emissivity ψ_j, which is the Doppler map. The distribution of emission in velocity space produces a phase-dependent line profile $\varphi(v_{||}, \phi)$, where $v_{||}$ is the line of sight velocity and ϕ is the orbital phase. The transformation from the emission distribution in velocity space (ψ_j) to the line profile (φ) is then given by a linear matrix P:

$$\varphi_i = \sum_j P_{ij}\psi_j, \tag{1.5}$$

where i is separated to n points. If the observed spectrum is $\tilde{\varphi}_i$, the objective of the reconstruction process is to determine a Doppler map ψ such that φ matches $\tilde{\varphi}$ within the observational uncertainties, while making as few assumptions on the nature of the map as possible. In the maximum entropy formulation, this is an optimization problem in which a single scalar quantity Q is maximized:

$$Q = H(\varphi, \tilde{\varphi}) + \alpha S(\psi). \tag{1.6}$$

Here H is the likelihood and, is a number which maximizes when the observations are matched exactly (i.e., $\varphi = \tilde{\varphi}$), and the entropy S, maximizes to produce smooth maps. For the likelihood, two forms are in current use:
i), the logarithmic form advocated by Lucy (1994) for positive definite images:

$$H = \sum_i \tilde{\varphi}_i \ln \varphi_i, \tag{1.7}$$

ii) and a χ^2-based likelihood:

$$H = -n \sum_{i=1}^{n} (\varphi_i - \tilde{\varphi}_i)^2. \tag{1.8}$$

For the entropy, they use the form with floating defaults introduced by Horne (1985)

$$S = -\sum_j \left(\psi_j \ln \frac{\psi_j}{\chi_j} + \chi_j \right), \tag{1.9}$$

where χ_j is the default image created from the map ψ by a smearing operation. Here, a simple Gaussian smearing is used in velocity space with an adjustable width. The default is used to bias the resulting map to a smooth map without necessarily biasing it toward a completely flat one. The value of α regulates how close a fit to the input data is obtained. An example of the application of the FMEM code to NLs has revealed the presence of the spiral structures in the accretion disc of UX UMa (Neustroev et al. 2011).

1.4 Radio observation of nova-likes

Astrophysical jets have been found in nearly all types of accreting objects, from supermassive black holes and X-ray binaries (XRBs) to supersoft sources (Motch 1998), young stellar objects and novae. Jets have been found in symbiotic stars (Taylor et al. 1986), and there are cases where jets have been imaged directly (Brocksopp et al. 2004). Sokoloski & Kenyon (2003) found that, for CH Cygni, a dip in hard X-rays is always followed by a radio ejection event. This is similar to what has been observed for XRBs. Although the connection between the accretion flow and jets is well documented and studied in XRBs (e.g. Homan et al. 2001, Fender et al. 2004) and active galactic nuclei (AGN) (Ho 2005, Körding et al. 2006), the physics is still not understood. Recently Körding et al. (2008) detected radio emission from a DN, SS Cygni (SS Cyg), and using the analogy between XRBs and CVs, they showed that SS Cyg has a variable high-brightness-temperature ($\sim$ 11000 K) radio counterpart, that is most likely associated with a synchrotron emission from a jet or collimated outflow.

Until recently, NLs have not been solidly detected in the radio regime. Torbett & Campbell (1987) reported a radio detection of $\sim$ 0.4 mJy source and associate this with AC Cancri (AC Cnc). The original detection was offset by 3.4 arcsec from the optical position of the source and it was never confirmed. Körding et al. (2011) re-reduced the original detection as well as new observations by the Very Large Array (VLA) made in 1989 May 19, and Multi-Element Radio Linked Interferometer Network (MERLIN) made from December 1996 to January 1997. The re-analysed images reveal a 0.37 ± 0.1 mJy source with an offset of more than 14 arcsec, making AC Cnc unlikely to be associated with the radio source. The VLA and MERLIN observations gave no indication of the radio source in AC Cnc.

Körding et al. (2011) reported the first reproducible radio detection of the NL variable V3885 Sagittarius (V3885 Sgr[1]), at 5.5 and 9 GHz from the observations carried out on 2010 February 7 using the Australian Telescope Compact Array (ATCA). This source was detected at both frequencies, its spectral index being $\alpha \sim 0.75 \pm 0.35$ at a flux level of $\sim$ 0.16 mJy at 5.5 GHz. Although the limit on the brightness temperature was relatively low, $T_B \geq 0.73$ K, it did not rule out any emission mechanisms, the source was not variable between the two observations, and no polarized emission was found. However, due to limited observational constraints, they could not possibly establish which emission process was responsible. But, based on the observations alone, the detected radio emission can originate from an unresolved nova shell or from shocks in the wind of V3885 Sgr. In addition, Körding et al. (2011) find V3885 Sgr to have a steep spectrum, typical for the optically thin synchrotron emission.

Deep transient surveys are revealing a wide range of new objects, e.g. faint CVs, especially DNe and NLs. The Catalina Real-time Transient Survey (CRTS) is one such large survey. Thousands of transient objects have been discovered from this survey, including more than 1000 CVs, by searching for variability in images taken with the intention of spotting hazardous asteroids. Without dedicated follow-up studies, we can investigate only a handful of these objects. In addition to that, much of the first five years of the MeerKAT telescope will be dedicated to a large sky survey in the radio regime. The ThunderKAT project is one of MeerKAT's key projects aimed at observing all transient synchrotron sources in the southern sky. Therefore, the MeerKAT radio sky survey will help in unveiling a large number of new CVs not discovered by previous surveys. Its sensitivity will also help in making available a large sample of DNe and NLs, and optical follow-ups will be required for further study of their characteristics.

1.5 EC21178-54

EC21178-54 is a 13.7 magnitude eclipsing NL variable which was discovered in the Edinburgh-Cape survey of blue objects (Stobie et al. 1997). Its orbital period is $P_{\rm orb} = 3.708$ hours (Warner et al. 2003). This orbital period was confirmed by Zietsman (2008) from the high-speed photometric data, where he also analysed the spectroscopic data obtained using the

---

[1] V3885 Sgr is a 9th magnitude NL CV belonging to the UX UMa sub-type which has not been classified as either a polar or intermediate polar (Ritter & Kolb 2005).

Southern African Large Telescope (SALT) in 2006 August 17 during the primary eclipse. The average spectrum of EC21178-54 was found to reveal strong, broad, and double-peaked emission in HeII 4686Å and Balmer (H_α, H_β, and H_δ), and other HeI lines. However, the spectrum was very noisy towards the shorter wavelengths, with a steep slope revealing the presence of a very hot central component in the system. Prior to that, Warner et al. (2003) had found EC21178-54 to be a rich source of dwarf nova oscillations (DNOs) and quasi-periodic oscillations (QPOs), see Warner (2004). The position and finding chart is recorded on the CBASTRO[1] website under the name EC21178-5417 as a NL with magnitude of $\sim$ 13.7 in the V filter, and coordinates (J2000): Right Ascension (RA) of $21^h21^m26.53^s$, and Declination (Dec) of $-54^\circ04'34.7''$. At the time of writing this dissertation, no detailed spectroscopic analysis is recorded in the literature.

1.6 Aim of the project

CVs vary on time scales of few seconds to millions of years. The emission lines in CVs reveal more information about the nature of object and the emission mechanism responsible. It is from these emission line that most of physical properties of CVs are derived. The component masses and radii of these systems are attainable by carefully analysing the emission lines. If there are spectral features attributed to the secondary star, careful modelling makes it possible to derive a distance to the binary (Southworth et al. 2009). In the case of eclipsing systems, carefully measuring the time between two eclipses help in accurately determination of the orbital period of the binary. Furthermore, from eclipse modelling, we can get the mass ratio (q) as well as the orbital inclination.

In this project, we will reduce and analyse phase-resolved photometry and spectroscopy of the eclipsing NL EC21178-54. This object has an orbital period of 3.708 h, and often shows rapid variability associated with magnetically-channelled accretion from the inner edge of the accretion disc onto the WD (Warner et al. 2003). No comprehensive study of this object has yet been made and in this MSc dissertation I will analyse photometric observations over one orbital cycle, in order get an accurate ephemeris that is essential in phasing the spectroscopic data. We have phase-resolved spectroscopy of EC21178-54 over four orbital cycles at two different epochs in 2011 which will be used to create Doppler maps and highlight the origin of the emission lines in this system. We seek the best fitting model of the bright spot from the Doppler maps of EC21178-54 by fitting various values of M_1, i, and q, and constraining the dimension of the accretion disc.

In Chapter 2 we list all the spectroscopic and photometric observations made for this project, as well as the details of the telescopes and instruments used. Chapter 3 describes the in-depth methods and steps followed while performing data reduction, especially the multiple spectroscopic data sets that were used. In Chapter 4 we present all the results obtained from

---

[1] The acronym CBASTRO stands for Center for Backyard Astrophysics and it is a global network of small telescopes dedicated to photometry of CVs. More details can be found at http://cbastro.org/.

the spectroscopic and photometric data reduction, which include the following: the new photometric ephemeris based on the light curve, average spectra of EC21178-54 obtained on different dates, phase-binned spectra, radial velocities of emission lines measured with `IRAF` and that measured using Tom Marsh's software `MOLLY` from two of the three data sets, and lastly the Doppler maps and trailed spectra of EC21178-54 obtained from the FMEM code coupled with `IDL`. Chapter 5 gives an in-depth discussion of the results, conclusions based on the results, and comparison between EC21178-54 and V3885 Sgr, as well as future planned work on our target object. Appendix A gives the original spectra of EC21178-54 after continuum normalization.

Chapter 2

Observations

2.1 Spectroscopy

2.1.1 SAAO 1.9-m Radcliffe reflector

The 1.9-m (74-in) reflector[1] telescope of the South African Astronomical Observatory (SAAO) was built between 1938-1948 by Grubb Parsons as part of the Radcliffe Observatory. The detailed history of the origin of the Radcliffe Observatory and SAAO 1.9-m telescope is available elsewhere (Moore & Collins 1977). This telescope was originally situated in Pretoria (between 1948-1970) but was moved to Sutherland due to bad light conditions in Pretoria. The other contributing factor for the move was the formation of the SAAO through the merging of three of South Africa's observatories: the Cape Observatory (Cape Town), the Radcliffe Observatory (Pretoria), and the Republic Observatory (Johannesburg). The 1.9-m telescope was the largest optical telescope at that time in South Africa, at least until 2004 when the Southern African Large Telescope (SALT) came into use.

The telescope remains operational today. The glass mirror is made of Pyrex and weighs 3.6 tons, and the whole telescope structure containing the mirror weighs about 5 tons. It is used in a Cassegrain configuration at the focal ratio of f/18 and the telescope is equatorially mounted. The instruments that are currently being used in the SAAO 1.9-m telescope are the Grating Spectrograph with SITe CCD, GIRAFFE: a Fibre-Fed Echelle Spectrograph, HIPPO: Photo-polarimeter, the SAAO CCD, and the recently commissioned Sutherland High-speed Optical Camera (SHOC).

2.1.2 Grating Spectrograph

The grating spectrograph has three main components: a SITe CCD (charge coupled device), a collimator slit, and a grating. An f/2.2 camera with an 86 mm beam is used in conjuction with the SITe CCD. The majority of the spectrograph functions are automated and operated from the computer. However, the grating angle adjustment, slit width adjustment,

---

[1] Details of this telescope can be found at http://www.saao.ac.za/science/facilities/telescopes/1-9m/

comparison beam filters, and arc lamps insertion are operated manually in the dome. The spectrograph has a slit scale of 6 arcsec/mm. The normal slit width is 1.5″, matching the typical seeing conditions in Sutherland. Reducing the slit width (in steps of 0.15″) lowers the throughput but increases the spectral resolution. The physical size of the SITe CCD is 1798 × 266 pixels with a pixel size of 15 μm, and is usable over wavelengths ranging from 0.35 to 1.0 μm (i.e., 3500 to 10000Å). Normally fringing effects are not a problem for wavelengths below 0.6 μm but above this wavelength, fringing effects become more severe, and the flat-fields should be obtained at the exact angle used for the observations to correct for this.

This instrument can be equipped with various detector gratings, ranging from 300–1200 lines/mm, giving different spectral resolutions. We only used grating 6 & 7 resulting in a wavelength coverage from approximately 3500-5400Å, and 3000-7000Å, respectively (see Table 2.1 for more details), depending on the grating angle used. The spectrograph uses various arc lamps: Cu-Ar for the blue part of the spectrum and Cu-Ne for red. We used the Cu-Ar arc lamps with either BG38 (for longer wavelength coverage) or BG39 (for shorter wavelength coverage) filters, for all the observations, centred at the blue part of the spectral range.

2.1.3 Spectroscopic observations

Observations of EC21178-54 were made with the SAAO 1.9-m Radcliffe reflector telescope at the SAAO station in Sutherland over four nights. The initial observations were taken on 2002 September 7 by Prof. David Kilkenny as part of the Edinburgh-Cape Blue Object Survey (see O'Donoghue et al. 2013); these are the spectra by which the source was classified as a nova-like (NL). The second set of observations were taken on 2011 September 5 by Dr Kurt van der Heyden covering two orbital cycles of the source with adequate phase resolution (i.e., 12 spectra per orbit). Continued phase-resolved spectra at higher spectral resolution were obtained by Prof. David Kilkenny over two consecutive nights in October 2011. A journal of these observations can be found in Table 2.1.

Table 2.1: Spectroscopic observation log of EC21178-54.

Date of obs.	Start time H:M	End time H:M	No. of spectra	Exp. time (s)	Grating number	Lines per mm	Grating angle (°)	λ_c (Å)	λ range (Å)
2002/09/7	17:03	21:55	7	600	Gr 6	600	14.1	4400	3480 - 5400
2011/09/5	20:47	02:13	24	600	Gr 7	300	17.2	5700	3550 - 7500
2011/10/22	18:11	21:42	12	900	Gr 6	600	14.1	4400	3480 - 5400
2011/10/23	17:41	21:32	12	900	Gr 6	600	14.1	4400	3480 - 5400

Notes: Date of obs. – date of observations; Start and End times are given in Universal Time (UT); No. of spectra – number of spectra taken on that specific night; Exp. time – exposure time; Gr 6 or 7 – grating type used; λ_c – central wavelength used; λ range – wavelength coverage of the spectra taken.

For all the data obtained by Prof. David Kilkenny (2002 and 2011), the SITe CCD was used and the spectra were prebinned 1 × 2 (i.e., 2 pixels were combined into 1 along the spatial axis). A slit width of 1.5$''$ was used. Grating 6 was used with a central wavelength of $\sim$ 4400Å, and a wavelength interval of 3450-5400Å. This range was chosen so that we include the H_β, H_γ, HeII 4686Å lines and the CIII/NIII blend at 4650Å, and also the CaII lines towards the blue part of the spectrum below 4000Å. For the data obtained on 2011 September 5, the same SITe CCD was used (slit width 1.5$''$) with the same prebinning. We used a different (lower resolution) grating so that the central wavelength was $\sim$ 5700Å, with a wavelength interval of 3600-7600Å. This includes the H_α line, and telluric lines towards the red, as well as the spectral range previously covered.

The exposure times were selected in such a way as to balance the requirement for maximum signal while remaining short enough to avoid the effects of velocity smearing. The exposure time for each spectrum was selected to be 600 s, or 900 s for the various observing runs (see Table 2.1). An exposure time of 600 s corresponds to 0.045 in the orbital phase, whereas 900 s corresponds to 0.067 in the orbital phase of EC21178-54, given an orbital period of 0.154525d (13351 s), see Section 4.1. These exposure times allow a sufficient phase resolution and coverage of the orbital cycle.

For the data of 2011 October, a series of 12 spectra were taken on each night, each separated by an arc spectrum with the exposure time of 30 s, in such a way that the observations cover one orbital cycle of the binary per night. Observations of the flux standard star LTT 7987 were also taken on the day of observations (at or close to the zenith) in order to correct for the instrumental response. For the data of 2011 September 5, a series of 24 spectra were taken, with each set of 3 exposures separated by one arc spectrum with 80 s exposure covering about two consecutive orbital cycles of EC21178-54. A spectrum of flux standard star EG21 was taken on that night in order to correct for the instrumental response.

On 2002 September 7, a total of 7 spectra of EC21178-54 were taken separated by one or two arc spectra with 40 s exposure. Since these spectra were intended for classification only, the binary orbit still was unknown and as a result the orbital coverage was poor. The spectra of the flux standard stars, HR 6812 and LTT 7379, were also taken on that night for calibration purposes. In most cases, the arc spectra were taken before and after each exposure to enable the spectra to be wavelength calibrated and to correct for any flexing in the instrument as the telescope tracks the target. A set of flat-fields frames was also taken at the beginning of each night.

2.2 Photometry

2.2.1 Sutherland High-Speed Optical Camera (SHOC)

The SHOC camera is a recently commissioned instrument that can be used on the three SAAO telescopes: 0.75-m, 1.0-m, and 1.9-m (Gulbis et al. 2011b, Coppejans et al. 2013). It is a high-speed, visible-wavelength, system that is mounted at Cassegrain focus, combined with the existing filter wheels employed by the SAAO CCDs. The SHOC design is based on two other instruments: POETS (Portable Occultation, Eclipse, and Transit System; Souza et al. 2006), and MORIS (Massachusetts Institute of Technology Optical Rapid Imaging System, Gulbis et al. 2010, 2011a).

The prime component of the SHOC instrument is an Andor iXon X3 888 UVB camera, which has high quantum efficiency ($>$ 90% from 4800 to 7000Å), low read noise, low dark current, and 2048 × 1024 (13 μm) pixel detectors operated in frame-transfer mode (imaging area of 1024 × 1024 pixels). The camera is controlled by a computer capable of recording data at high speed (subsecond). It also uses a global positioning system (GPS) for accurate timing and can take exposures at microsecond speed ($<$ 10 μs using frame-by-frame GPS triggering). The UVB component consists of a back-illuminated CCD with UV phosphor (elevating the quantum efficiency to $\sim$ 35% below 3800Å) as well as an uncoated fused silica window. The camera is thermo-electrically cooled, typically operating at -70° C (Gulbis et al. 2011b).

The SHOC camera has a new unique feature, electron-multiplying technology, where electrons are transferred through an extended register and undergo impact ionization. This strengthens the observed signal and reduces read noise to subelectrons levels thereby increasing the quality of the data. The SHOC camera features a selection of custom binning and subframing, and readout amplifiers: 1 MHz and 3 MHz in conventional mode or 1 MHz, 3 MHz, 5 MHz, and 10 MHz in electron-multiplying (EM) mode, each having multiple preamplifier gain settings. The field of view varies with the telescope in use, from 1.3 × 1.3 arcmin on the 1.9-m telescope, to 2.9 × 2.9 arcmin on the 1.0-m telescope, and 3.8 × 3.8 arcmin on the 0.75-m telescope of the SAAO (see Gulbis et al. 2011b). For more details of the SHOC camera see also Coppejans et al. (2013).

2.2.2 Photometric observations

Photometric observations of EC21178-54 were made on the night of 2011 October 5 with the SAAO 1.9-m telescope using the SHOC camera for the purpose of a refined 2011 ephemeris of EC21178-54. A record of observation is given in Table 2.2. The observations were made in white light (unfiltered) mode. The SHOC camera was mounted below the filter wheel of the 1.9-m reflector telescope. The field of view is 1.3 × 1.3 arcmin^2, and the data were binned 8 × 8 for a plate scale of 0.61 arcsec pixel^{-1}. Sky flat-fields were obtained at the beginning of the night with the same binning of the CCDs.

For the observations of EC21178-54, the exposure time was 0.5 s, and the detectors were used in frame transfer mode. The 1 MHz electron-multiplying (EM) mode was used with an EM gain of 20 and a pre-amplifier gain of 7.5 e^{-}pixel^{-1}. An effective read noise $\sim$ 1 e^{-}pixel^{-1} is achieved by using these settings. The camera was thermo-electrically cooled at -70° C, resulting in a dark current of $<$ 0.001 e^{-}pixel^{-1}.

Table 2.2: Photometric observation log of EC21178-54.

Run No.	Date of start of night	Start time HJD = 2450000.0 +	End time HJD = 2450000.0 +	Length (hrs)	t_{int} (s)	Telescope
S8097	2011/10/5	5840.27376	5840.45088	4.15	0.5	1.9-m.

Notes: Run No. – observational run number and t_{int} is the integration time.

Figure 2.1 shows an example of a simple exposure of EC21178-54 with the SHOC camera. EC21178-54 is marked clearly by "EC" on the right side of each panel; the other bright star (left of each panel) in the field is used for relative photometry (Section 3.2). From simultaneous g', r', and i' photometry of EC21178-54 by Dr Takahiro Nagayama using TRIPOL on the 0.75-m telescope, we determined the brightness of the comparison star as $r' = 13.07$ mag (Nagayama, priv. communication). The image on the left panel of Figure 2.1 was taken when the binary was out-of-eclipse, whereas the one on the right panel was taken during eclipse; EC21178-54 changes in brightness substantially. See Figure A.1 for more details.

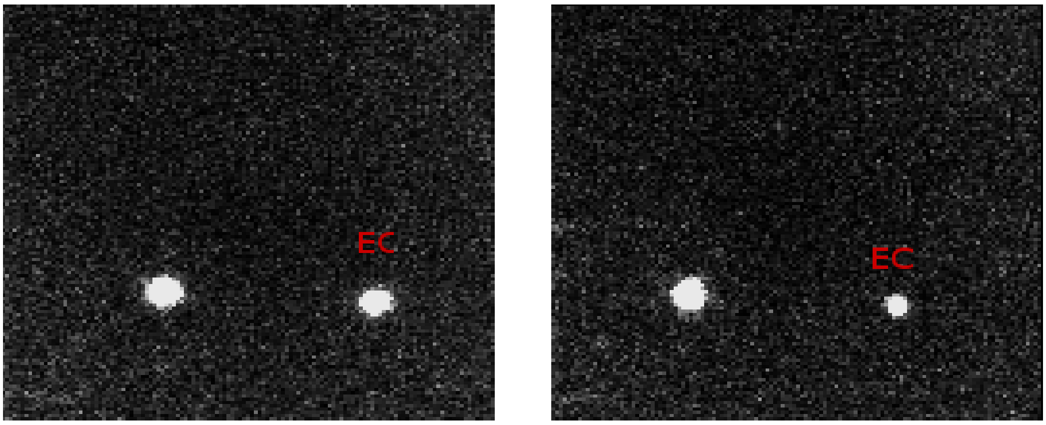

Figure 2.1: An example of a photometric exposure of EC21178-54 (right star on each panel) and comparison star (left star on each panel) using the SHOC camera. The image on the left was taken when the system was out-of-eclipse whereas the one on the right was taken during the eclipse.

Chapter 3

Data reduction

3.1 Spectroscopy

The spectroscopic data of EC21178-54 were reduced using the `IRAF`[1] data reduction package. This section describes all the steps in the data reduction process such as spectral extraction, wavelength calibration, and flux calibration.

3.1.1 Extraction

The first thing that was done was to clean the CCD images, and to remove the variation in pixel-to-pixel response – a process known as flat-fielding. This was achieved by using the `FLATCOMBINE` and `CCDPROC` tasks under the `CCDRED` package in `IRAF`. The former combines all the dome flat-fields into one master flat-field frame, which ensured a cosmic-ray-free final flat-field, and the latter subtracts the value of the overscan regions from the CCDs and trims the selected area of interest.

The next task was to normalize the flat-field obtained from `FLATCOMBINE`. To do this the `RESPONSE` task under the `LONGSLIT` package was employed. The resulting normalized flat-field was used to flat field all the object, standard star, and arc lamp frames. Figure 3.1 shows an example of a 2-dimensional spectrum after the image was cleaned, overscan-subtracted, trimmed and flat-fielded. The approximate position where the object's spectrum was extracted is indicated by "object" in Figure 3.1. The lower line corresponds to the spectrum of the reference star shown in Figure 2.1.

All the spectra were extracted using `IRAF's` implementation of optimal extraction (variance-weighted) using the `APALL` task in the `KPNOSLIT` package in `IRAF`. The spectra of the object and standard star were extracted using the `APALL` task in interactive mode. The interactive mode requires the following steps: re-adjusting the aperture to the centre, editing the aperture, tracing the aperture along the dispersion axis, fitting the polynomial to the aperture

---

[1] `IRAF` is distributed by the National Optical Astronomy Observatories, which are operated by the Association of Universities for Research in Astronomy, Inc., under cooperative agreement with the National Science Foundation

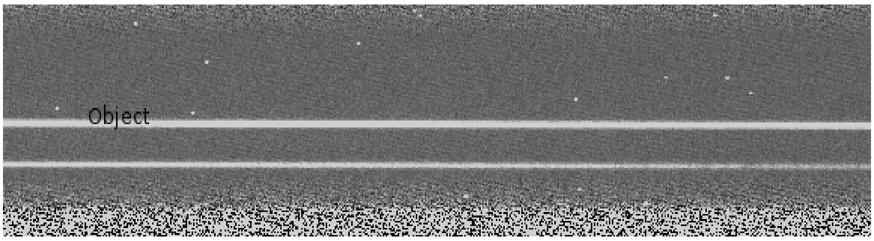

Figure 3.1: The 2-dimensional spectrum of EC21178-54 after being overscan-subtracted, trimmed, and flat-fielded.

until the RMS is ~ 0.03 pixels, writing the aperture to the `database` directory (created by `IRAF` when running `APALL`), and extracting aperture spectra.

In preparation for this procedure, we ran the `APALL` task, and the `IRAF` graphics terminal appeared (see Figure 3.2(a)). The region where the spectra of EC21178-54 were extracted is marked by "`1`". Another feature, shown on the left of Figure 3.2(a), is the noise (see also the bottom of Figure 3.1). The next steps were to edit, then trace the aperture; the latter is done automatically in `IRAF`. We fit a polynomial to the aperture (see Figure 3.2(b)) and occasionally remove points that lie too far away from the polynomial. A typical value of the RMS of such a fit is ~ 0.03 pixels. At this stage, the writing of the aperture to the `database` occurs automatically within the program. We then extracted the aperture spectra to a new frame. Figure 3.3(a) gives an example of an aperture spectrum after running `APALL`. The aperture spectra of the standard star were also extracted in the same way as those for the object.

The arc lamp aperture spectra (Figure 3.3(b)) were extracted using the `APSUM` task which is also within `KPNOSLIT`. `APSUM` is a short version of `APALL` that uses the object's spectra as a reference to extract the arc lamp aperture spectra from the same region of the CCD where the spectra of the object have been extracted. Note that the wavelength ranges from red to blue in Figure 3.3 (from left to right). The SITe CCD is more sensitive at red wavelengths than it is in the blue. On the grating spectrograph with the SITe CCD, the spectra always start from the red wavelengths to the blue wavelengths (with pixel number 1 at longer wavelengths and 1798 at shorter wavelengths). The resulting spectra are given in Figure 3.3(a) and (b).

3.1.2 Wavelength calibration

After extraction, the spectra were ready for wavelength calibration. This was done using a task called `IDENTIFY` employing the standard Cu-Ar arc lamps. A total of ~ 20 arc lamp lines with known wavelengths were identified on one arc frame. Figure 3.4(a) shows an example of the arc lamp spectrum (grating 6) before wavelength calibration, whereas in Figure 3.4(b)

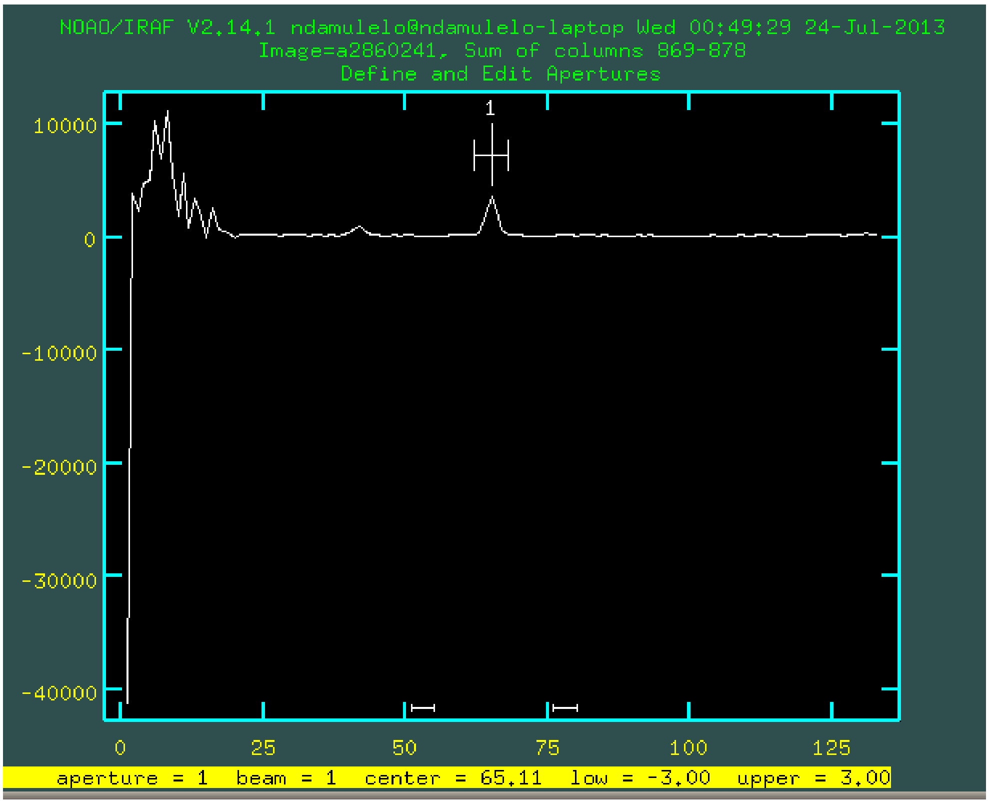

```
NOAO/IRAF V2.14.1 ndamulelo@ndamulelo-laptop Wed 00:49:29 24-Jul-2013
Image=a2860241, Sum of columns 869-878
Define and Edit Apertures
```

```
aperture = 1  beam = 1  center = 65.11  low = -3.00  upper = 3.00
```

(a) Aperture

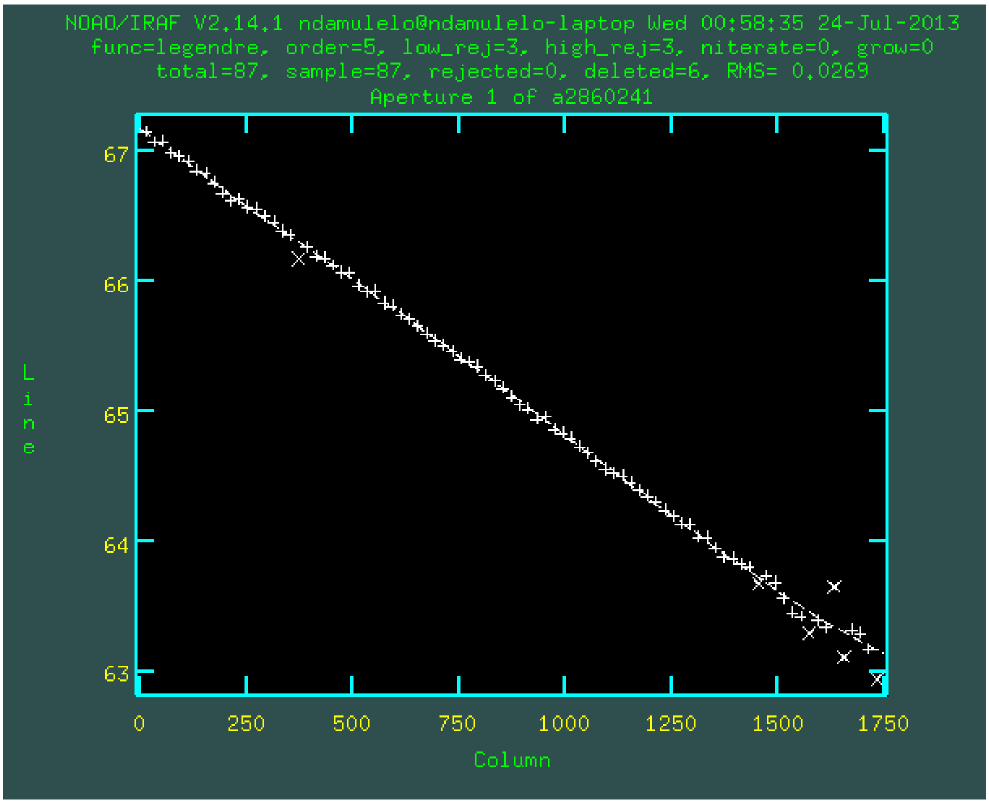

```
NOAO/IRAF V2.14.1 ndamulelo@ndamulelo-laptop Wed 00:58:35 24-Jul-2013
func=legendre, order=5, low_rej=3, high_rej=3, niterate=0, grow=0
total=87, sample=87, rejected=0, deleted=6, RMS= 0.0269
Aperture 1 of a2860241
```

(b) Fitting curve to aperture

Figure 3.2: An example of how an aperture spectrum appears when the `APALL` task in `IRAF` is performed. Top panel: defining the aperture; lower panel: tracing the aperture.

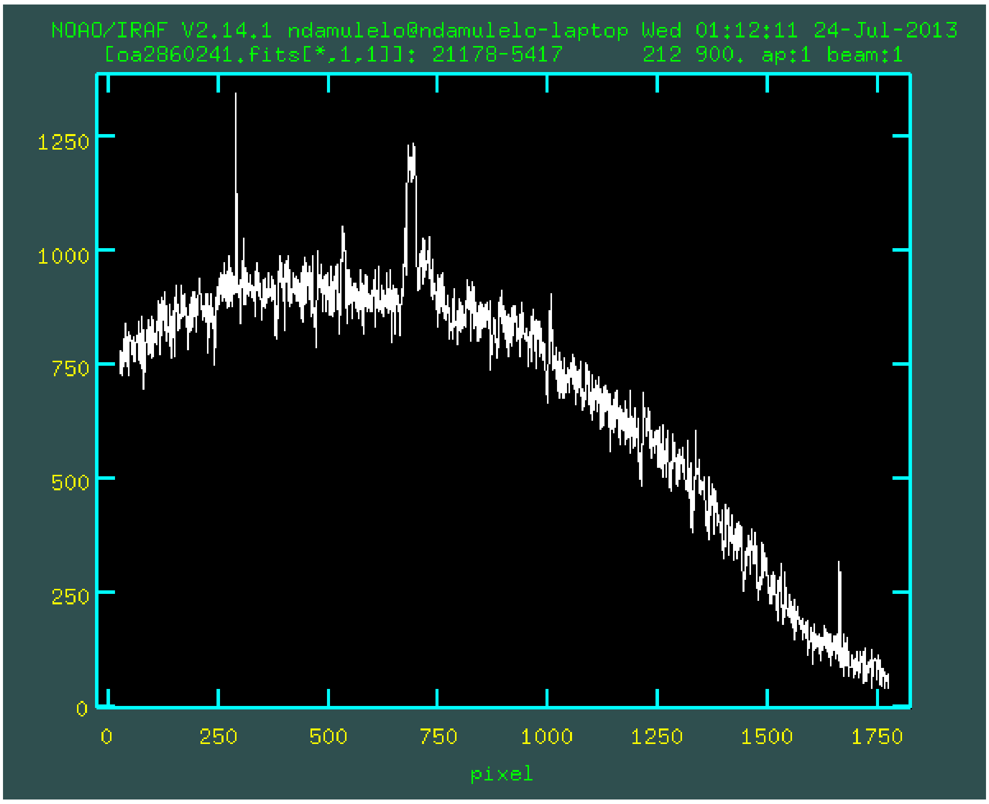

(a) Extracted aperture object spectra

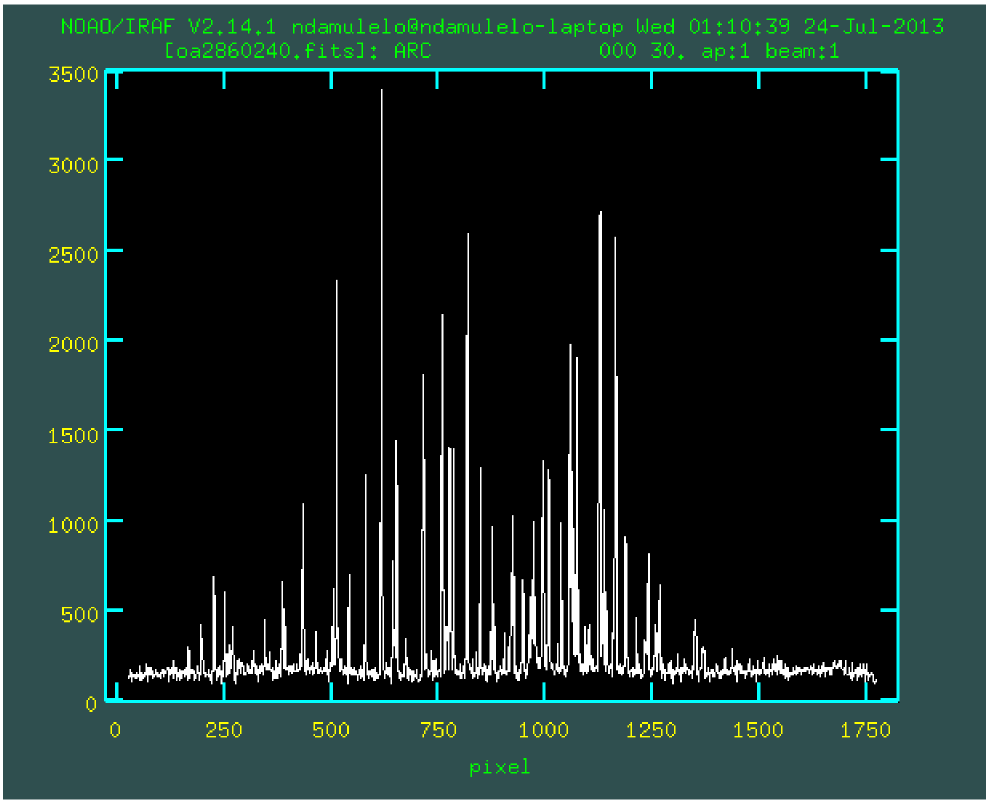

(b) Extracted aperture arc lamp spectra

Figure 3.3: An example of the extracted aperture spectra for the object (top panel) and the Cu-Ar arc lamp (bottom panel). These spectra were taken on 2011 October 22 using grating 6.

we show the arc lamp spectrum with marked arc-lines after wavelength calibration. After wavelength calibration, the arc lamp spectrum is flipped in the wavelength axis. All arc lamp spectra were fitted with a fifth-order linear polynomial until an RMS of ≈ 0.04 Å was achieved (see Table 3.1 for further details). The rest of the arc lamp spectra were identified using the `REIDENTIFY` task, and were also fitted with the fifth-order linear polynomial until RMS ≈ 0.04Å was attained using the first arc lamp spectrum as reference.

The arc lamps were then assigned to a specific object's spectra using the task `REFSPECTRA` in such a way that each spectrum had two reference arc lamps (one taken before and one after each spectrum). Before that, we updated the airmass information in the header using the `SETAIRMASS` task. We then ran `DISPCOR` to assign the Cu-Ar wavelength solution to each matching object spectrum. Before running `DISPCOR`, the spectrum of the target star would appear as shown in Figure 3.5(a). Following wavelength calibration, having run `DISPCOR`, we obtained the spectrum of the object (see Figure 3.5(b)). The spectra are also flipped. The wavelength-calibrated standard star spectra were also obtained the same way as those of the object's spectra. We removed cosmic rays (see e.g. Figure 3.5(a) at around 250 pixels) from the spectra by hand using `SPLOT`; inspecting each individual spectrum and marking both sides of each cosmic ray with "x", then replacing the original with the new spectrum free of cosmic rays under the same name, in order to eliminate confusion.

Table 3.1: Spectroscopic reduction parameters obtained for EC21178-54 spectra.

Date of obs.	Start time H:M	End time H:M	No. of spec.	Exp. time (s)	Grat. angle (°)	λ_c (Å)	RMS Å	Pixel Res. Å/pixel	λ range (Å)
2002/09/7	17:03	21:55	7	600	14.1	4400	~ 0.04	1.11	3480 - 5400
2011/09/5	20:47	02:13	24	600	17.2	5700	~ 0.08	2.29	3550 - 7500
2011/10/22	18:11	21:42	12	900	14.1	4400	~ 0.04	1.11	3480 - 5400
2011/10/23	17:41	21:32	12	900	14.1	4400	~ 0.04	1.11	3480 - 5400

Notes: Date of obs. – date of observations; Start and End times are given in Universal Time (UT); No. of spec. – number of spectra taken on that specific night; Exp. time – exposure time; Grat. angle – grating angle of the filters used; λ_c – central wavelength used; RMS - root-mean-square of wavelength calibration in units Å; Pixel Res. – pixel resolution; λ range – wavelength coverage of the spectra taken.

While running `DISPCOR`, we noticed that these spectra had different pixel resolutions depending on wavelength coverage, grating type and grating angle used. The different resolution spectra noted in Table 3.1, are due to the fact that a different grating was used in the 2011 September 5 spectra (according to Table 2.1), not due to the grating angle only. For all the observations, the Cu-Ar arc lamp was used. The grating angle for the observations taken in 2002 September and 2011 October was set to ∼ 14.1°, giving a reciprocal dispersion of 1.11 Å/pixel. From the high resolution spectra obtained, we measured the full widths at half maximum (FWHM) for some of the arc lamp emission lines. We estimated the average resolution of ∼ 3.4 Å for each of H_β, HeII 4686Å, and H_γ, for the 2011 October and 2002 September data, respectively. For the observations taken in 2011 September, the grating angle was set to ∼ 17.2°, giving a reciprocal dispersion of 2.29 Å/pixel. From measurements

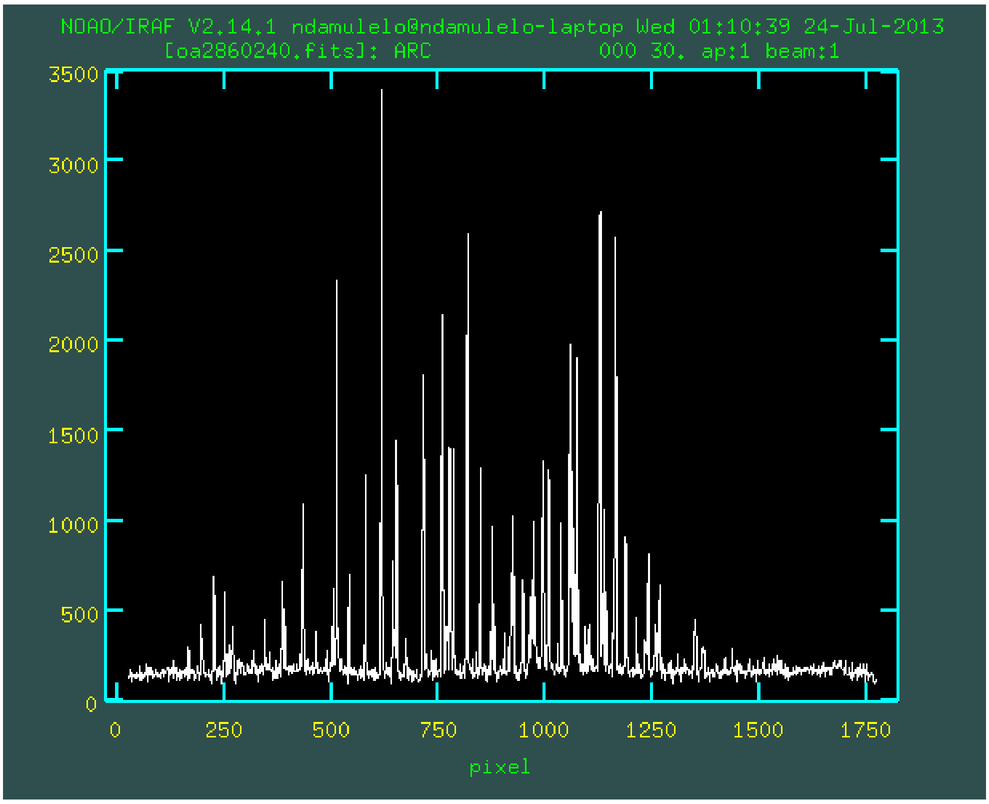

(a) Before wavelength calibration

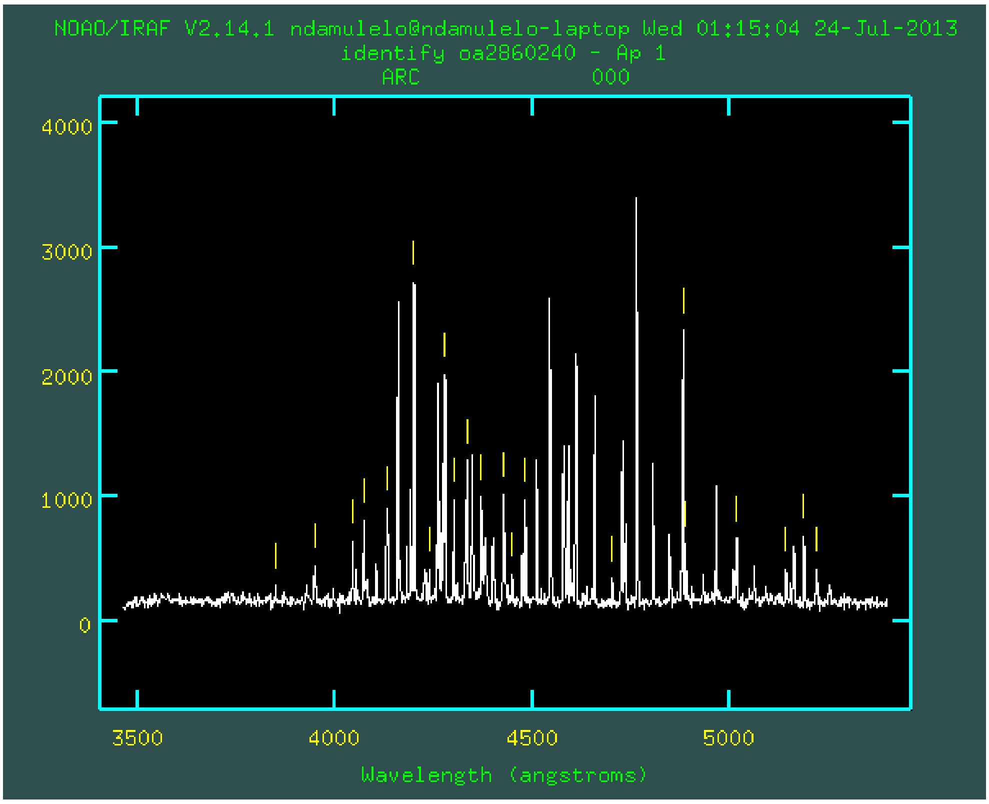

(b) After wavelength calibration

Figure 3.4: An arc lamp spectrum before (top panel) and after (bottom panel) wavelength calibration.

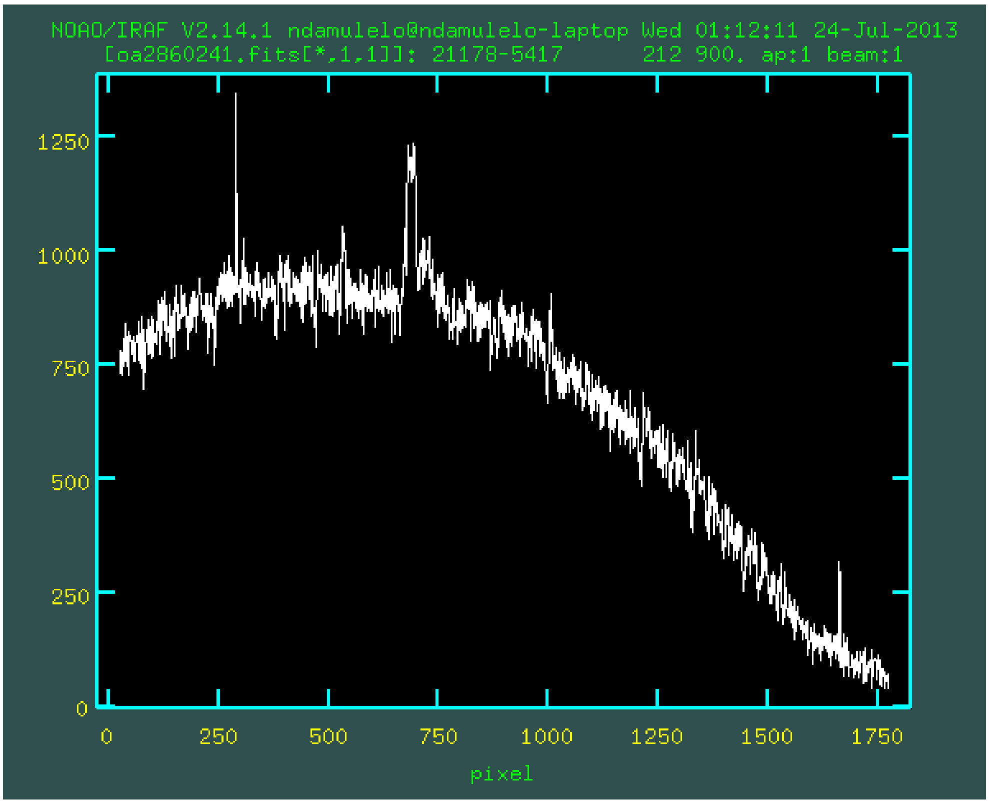

(a) Before wavelength calibration

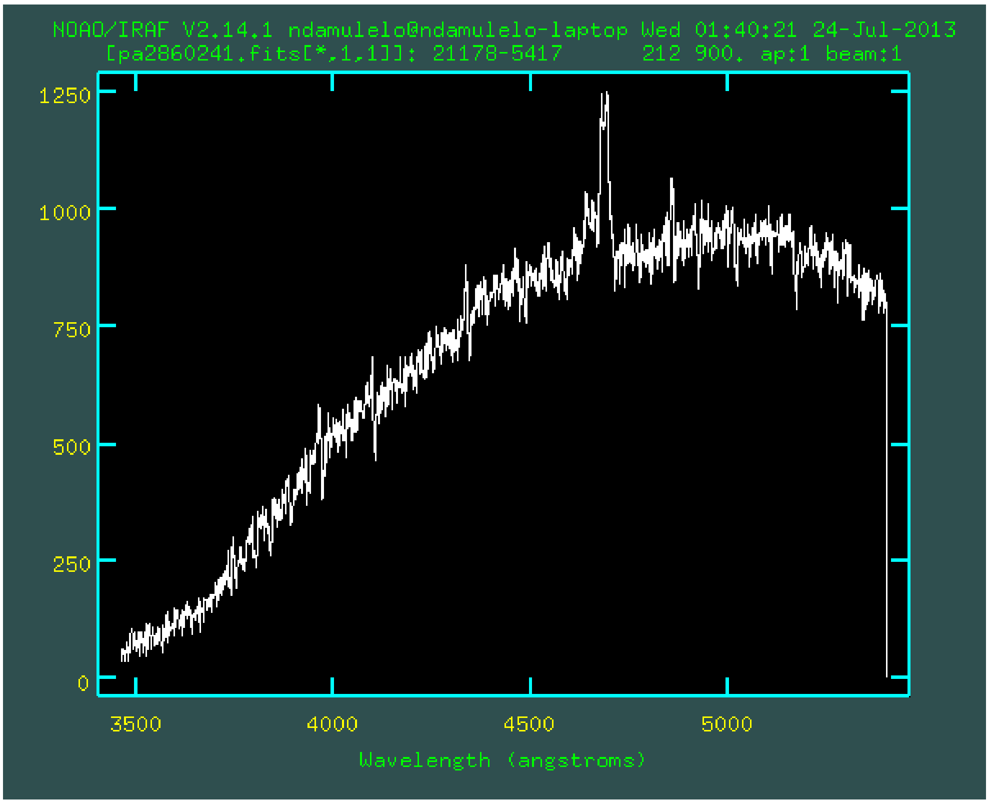

(b) After wavelength calibration

Figure 3.5: The spectrum of EC21178-54 before (top panel) and after (bottom panel) wavelength length calibration.

of FWHM of the arc lamp emission lines, we estimated the average resolution of $\sim$ 5.0 Å for each of H_α, H_β, HeII 4686Å, H_γ, and H_δ, respectively. Table 3.1 gives an overview of the spectral range and resolution of the observations.

3.1.3 Flux calibration

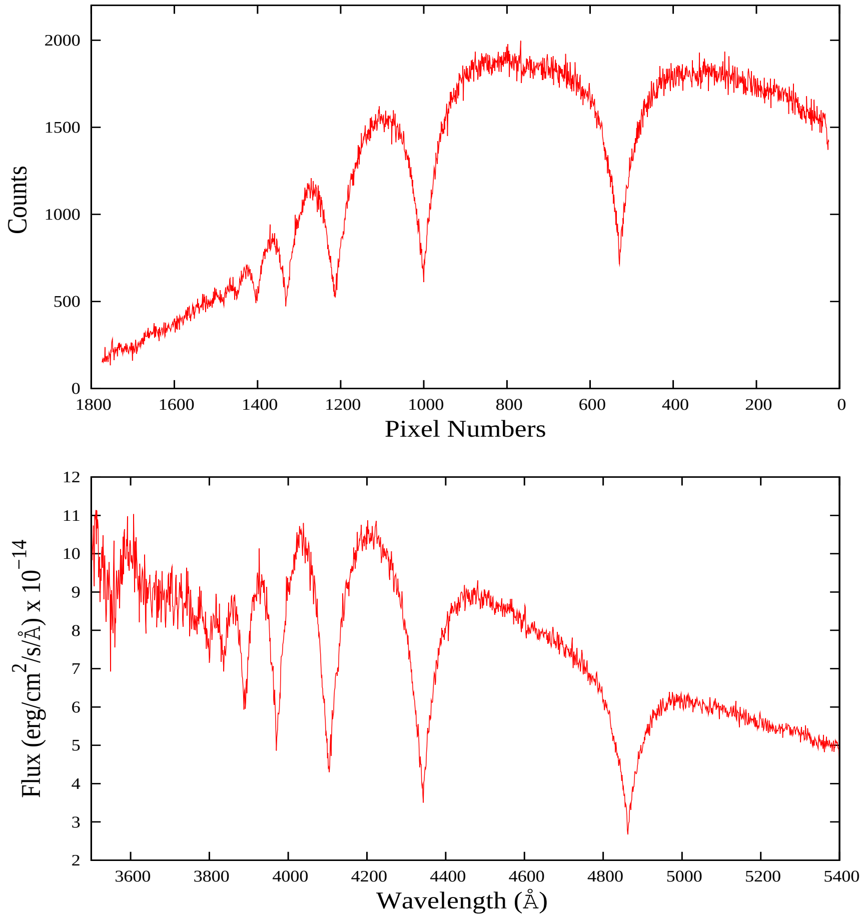

Figure 3.6: The spectrum of LTT 7987 before flux and wavelength calibration (top panel) and after flux and wavelength calibration (bottom panel). Grating 6 was used in this example.

The flux calibration was based on the spectrum of the spectrophotometric standard stars LTT 7987, EG21, LTT 7379, and HR 6812 (Baldwin & Stone 1984). In order to flux calibrate each spectrum, we ran the task `STANDARD` which compares the instrumental response flux of the standard star, e.g. LTT 7987, Figure 3.6 (top), with the flux stored in the `IRAF library` for the same star, giving the output file called `std`. The next task was to run the `SENSFUNC` task, which uses the `std` file to compute the sensitivity function thus producing the `FITS` file

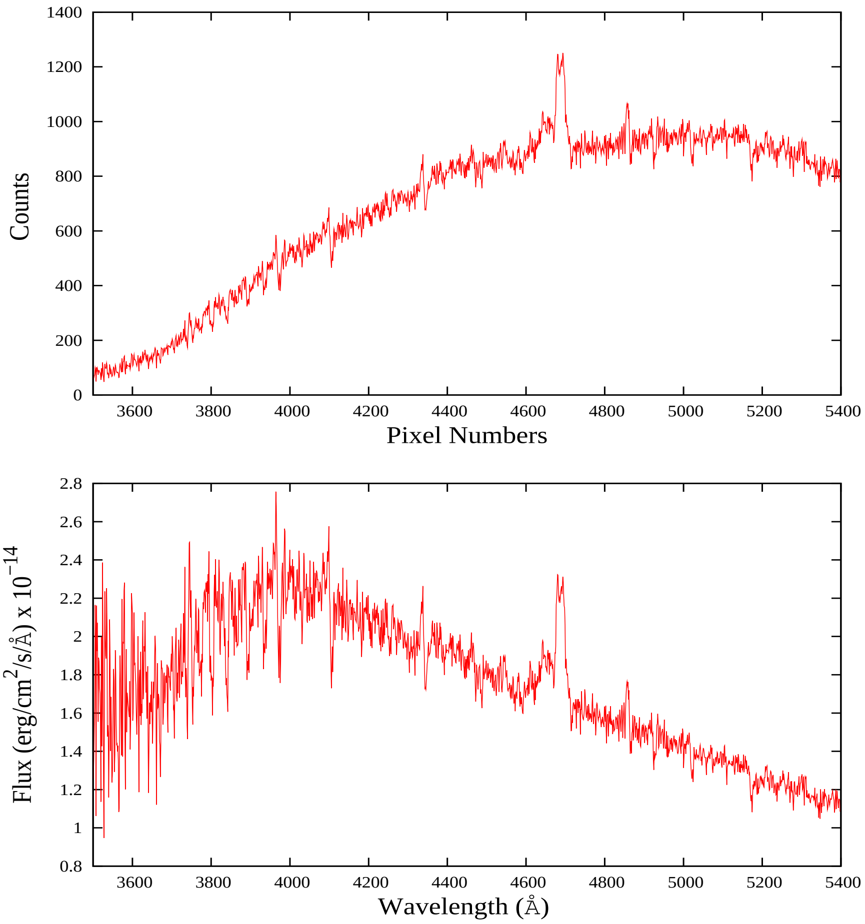

Figure 3.7: The spectrum of EC21178-54 before flux calibration (top panel) and after flux and wavelength calibration (bottom panel). Grating 6 was used in this example.

called `sens.fits`. Using the `sens.fits` file, we introduced the `CALIBRATE` task in `IRAF` to calibrate/correct the instrumental flux to the normal flux. The effect of this task is shown in Figure 3.6, the top panel showing the instrumental flux of LTT 7987 before flux calibration, and the bottom panel showing the calibrated flux of the same star matched to the input `IRAF library` value. The top panel horizontal axis is inverted because in this example spectrum the wavelength calibration had not yet taken place. Flux calibration was done to the object's spectra as well. Figure 3.7 shows the spectrum of EC21178-54 before (top) and after (bottom) flux calibration. The features below 3800 Å (bottom panel of Figures 3.6 and 3.7) are attributed to noise caused by divisions by very small numbers (the CCD used is very insensitive in the blue regions). The read-out noise (6.5 e^-(rms)) and photon gain (1 e^-/ADU) necessary for the extraction were calculated from the flat-field frames. At this stage the spectra obtained were not yet transformed to the heliocentric rest-frame. The spectra were then continuum normalized using the `CONTINUUM` task and fitting a fifth-order polynomial. No interstellar extinction correction was applied to the spectra, and no local extinction values for Sutherland were used in the flux calibration.

3.1.4 Signal-to-Noise

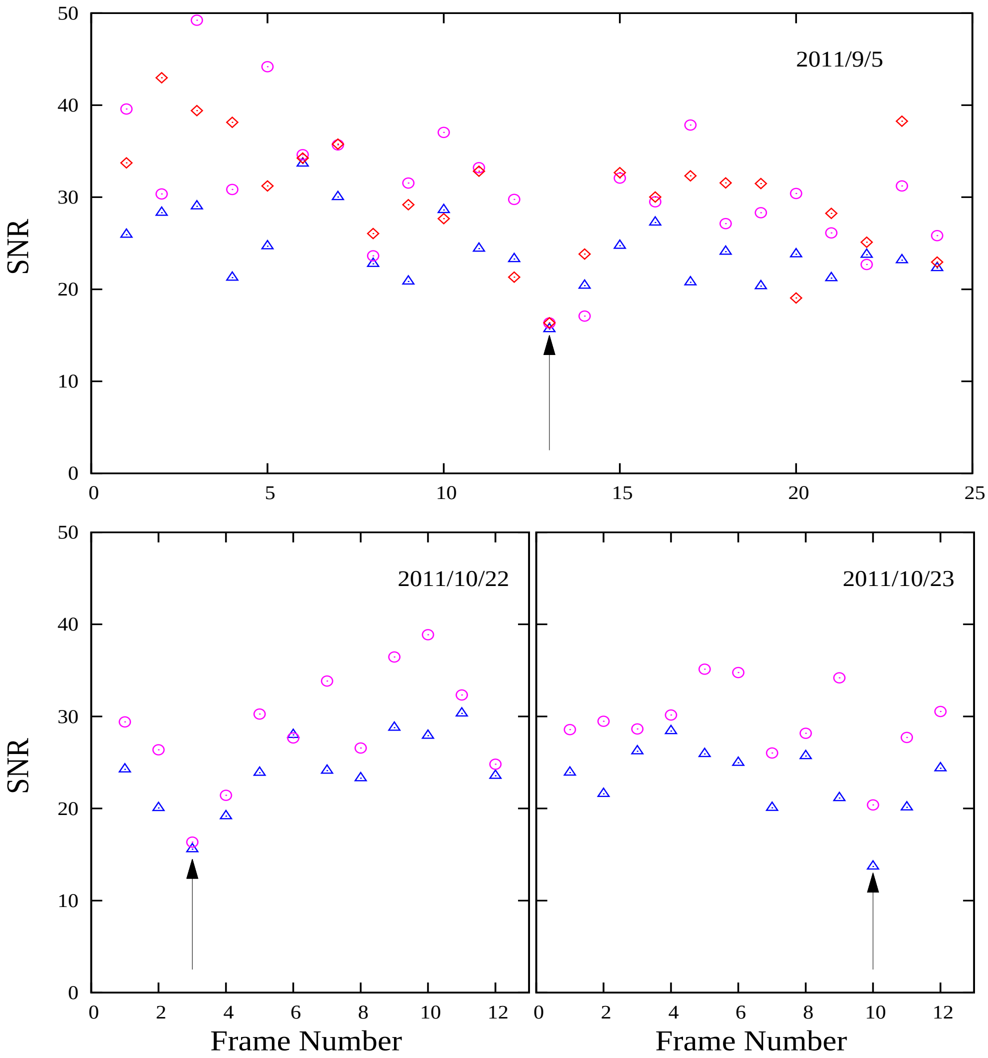

Figure 3.8: Signal-to-noise ratio as a function of frame number for both spectra from 2011 October 22-23 and 2011 September 5. The regions used are 4450-4550 Å (open blue triangles), 4725-4825 Å (open magenta circles), and 6350-6450 Å (open red rhombus). Observations taken during an eclipse are marked by the vertical arrows.

The signal-to-noise ratio (SNR) determination for each spectrum was performed using `SPLOT` in `IRAF`. The regions of the spectrum corresponding to 4450-4550 Å, 4725-4825 Å, and 6350-6450 Å were chosen respectively, because they contains few, if any, detectable features, with the exception of the blue region which contains an absorption feature associated with HeI 4471Å. However, the regions between 4100 and 4300 Å were available, but also contained two broad emission features which would have affected our results.

In Figure 3.8 the open blue triangles, open magenta circles, and open red rhombus show the SNR obtained for the 4450-4550 Å, 4725-4825 Å, and 6350-6450 Å parts of the spectrum, as a function of frame number. The horizontal axis on each panel in Figure 3.8 represents the spectrum/frame number from the first spectrum to the last taken on that day (see Table 2.1). The SNR calculated from both data sets average to $\gtrsim 20$. The black arrow in each panel marks the SNR obtained from the spectra taken close to the primary eclipse. Most of this dissertation concentrates largely on the 2011 October 22-23 data for the analysis in Chapter 4 (Section 4.2) since these observations have a better wavelength resolution.

It is clear from the top panel of Figure 3.8 that the SNR for the three regions considered (4450-4550 Å, 4725-4825 Å, and 6350-6450 Å for 2011 September data) never rises above 50. The SNR drops below 20 mid-way through the observations due to the eclipse. The bottom panels of Figure 3.8 (2011 October data) reveals that the SNR was greater than 20 for most of the points plotted, with the exception of the spectra taken close to the eclipse, where the SNR dropped below 20. The SNR was always higher in the 4725-4825 Å region (~ 30) compared to the 4450-4550 Å region (~ 25).

3.2 Photometry

The images from the SHOC instruments are obtained in `FITS` (Flexible Image Transportation System) data cubes. The data cubes can be reduced as a whole or split up into individual fits files and update their headers with the correct information for each fits image. Data reduction can be done on-the-fly during the observations using SHOCpipeline scripts.

We used `IRAF` to reduce the SHOC data. First an average flat-field is created. For this we split the data cube into individual fits files with the task `IMSLICE` and use `FLATCOMBINE` to create the averaged flat-field. This image is then normalized by the mean pixel value. Next the data cube of the EC21178-54 observations was split up into individual images. The images were flat-fielded by dividing each fits image by the normalized flat-field. EC21178-54 and the comparison star were identified on each image, e.g. with the `IRAF` task `DAOFIND`, and aperture photometry was obtained for both stars, using `PHOT` in the `DAOPHOT` package. Multiple apertures were used and an aperture correction was applied using `MKAPFILE` in `IRAF` (Stetson 1990). The aperture correction corrects for variations in seeing and allows for accurate photometry especially for bright stars.

The heliocentric julian dates (HJD) for each observation was calculated using the `SETJD` task in `IRAF`. For the final light curve (see Figure 3.9) a differential correction was applied to the photometry of EC21178-54 by assuming that the comparison star in the field is constant and has a brightness of $r' = 13.07$ mag. Even though our observations are taken in white light, details of variability and eclipse depth match that of the light curve in the r' band obtained by Dr. Nagayama with TRIPOL at the same time, hence we roughly calibrate the magnitude on the r' filter system. Note that these observations are only used to determine the time of mid-eclipse for the 2011 ephemeris so precise photometry calibration is not essential.

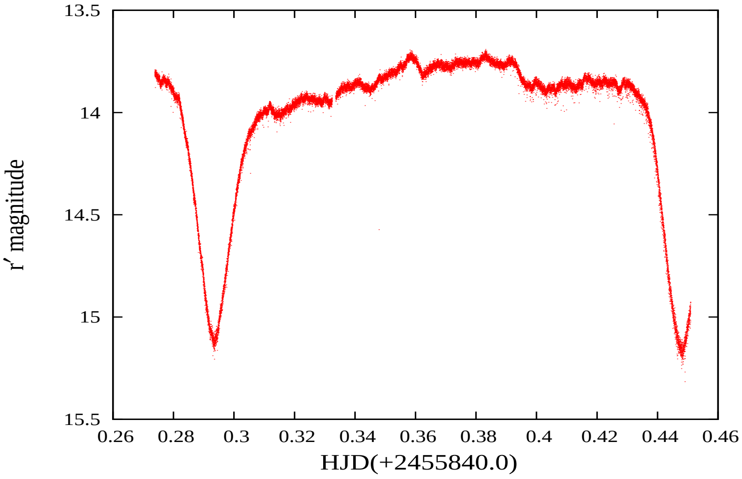

Figure 3.9: Photometric light curve of EC21178-54 obtained from our 2011 October 5 observations.

Chapter 4

Analysis

4.1 Photometric ephemeris

The light curve of EC21178-54 (Figure 4.1) obtained on 2011 October 5 shows deep symmetrical V-shaped primary eclipse minima, with out-of-eclipse magnitudes of $\sim$ 13.8 mag and a depth of the primary eclipse of about 1.3 mag. The light curve has been folded on the orbital period of 0.154525 days and $\phi = 0.0$ corresponds to mid-eclipse (see Eq. 4.2). The brightness of EC21178-54 is consistent with previous observations made for this system in 2002 September and 2006 August (Warner et al. 2003, Zietsman 2008). The total width of the eclipse is $\sim$ 0.1 in orbital phase. There is some short time-scales variability present in the light curve, but this appears to be mere flickering. No DNOs, lpDNOs or QPOs (Warner et al. 2003) were detected in the 2011 October observations.

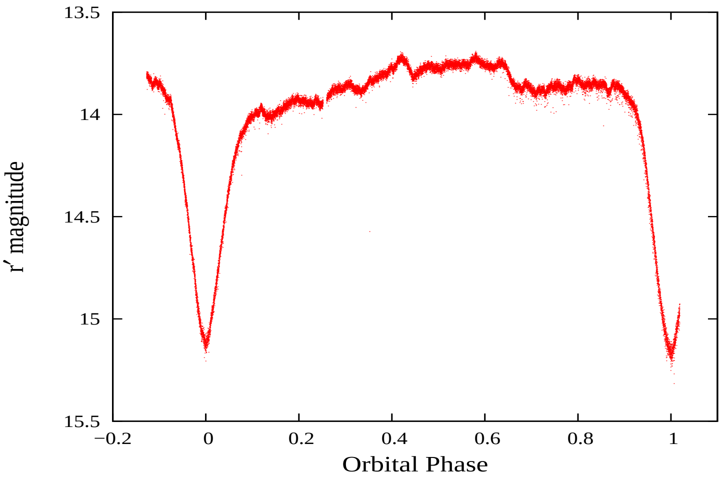

Figure 4.1: The photometric light curve of EC21178-54 obtained from our 2011 October 5 observations, showing the deep eclipse. The orbital phases were calculated using the new ephemeris (Eq. 4.2).

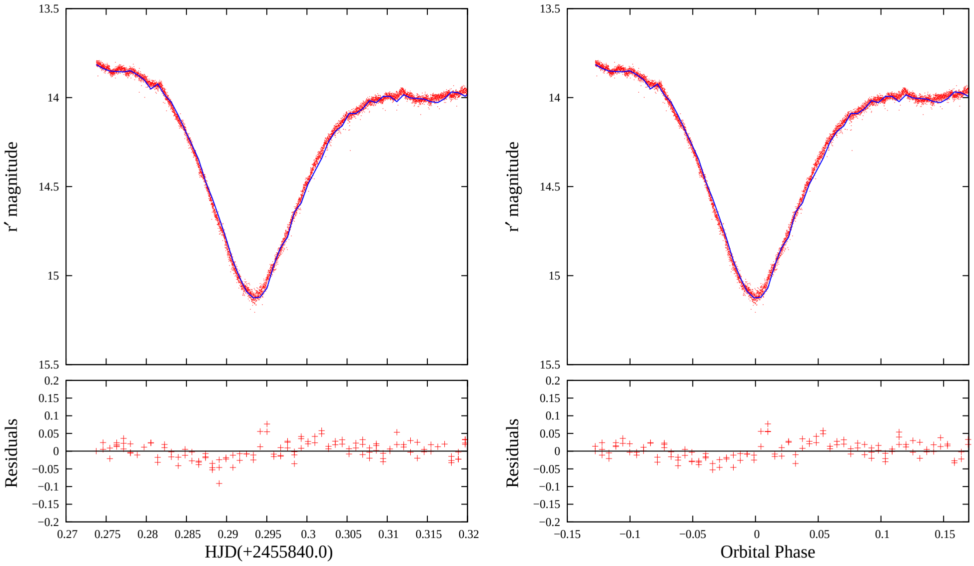

Figure 4.2: The photometric light curve of EC21178-54 (left and right) used to find the first minimum ($\mathrm{HJD_{min}}$) of the eclipses. The red small dots represent the original data and superimposed is a cubic spline (solid blue line) function that was fitted to the data. The left panel shows magnitude and time in HJD, whereas the right panel shows magnitude and orbital phase.

In order for accurate orbital phases to be calculated for our spectra, a new orbital ephemeris was required. The ephemeris is measured using the minimum brightness during eclipse, but in CVs this can occur at an imprecise time due to flickering, noise and other factors that may cause non-uniform brightness distribution in the accretion disc. To calculate the time of mid-eclipse, a computer program was written in `Python` which uses a third-order smooth cubic spline function from `Matplotlib` to calculate the new magnitude based on the light curve given in Figure 4.1. The resulting light curve (blue) is shown in Figure 4.2 superimposed on the original data (red dots). The Heliocentric Julian Date (HJD[1]) that correspond to the eclipse minimum was located by finding the lowest point corresponding to the first minimum of the magnitude given by the cubic spline light curve.

The value of the HJD that correspond with the minimum magnitude was then used as $\mathrm{HJD_{min}}$ associated with cycle (E) zero of the new ephemeris, Eq. 4.2. This is reflected in the resulting phased light curve of EC21178-54 in the right panel of Figure 4.2 with $\phi = 0.0$ coinciding with the eclipse minimum. We adopted the orbital period and its errors given by Zietsman (2008) obtained from the 2002 photometric data (Eq. 4.1):

$$\mathrm{HJD_{min}} = 2452525.374416\ (\pm\ 2 \times 10^{-4}) + 0.154525\ (\pm 1 \times 10^{-6})\mathrm{E}. \tag{4.1}$$

---

[1] The Heliocentric Julian Date is the Julian Date (JD) corrected for differences in the Earth's position with respect to the Sun.

The new ephemeris of EC21178-54 based on the light curve shown in Figure 4.2 and cubic spline fitting is therefore:

$$\mathrm{HJD_{min}} = 2455840.2935 \ (\pm \ 6 \times 10^{-4}) + 0.154525 \ (\pm 1 \times 10^{-6})\mathrm{E}. \tag{4.2}$$

The numbers in parenthesis indicate the uncertainty in the orbital period and phase zero point. The uncertainty in the phase zero point of Eq. (4.2) was calculated by assuming that the function fitted to the eclipse is a symmetric Gaussian function. Taking the minimum and maximum magnitude to be at 15.13 and 13.8 mag around the eclipse, 63% of the eclipse depth occurs at 14.64 mag. I identified the corresponding values in HJD on the x-axis that correspond to 14.64 mag and calculated the standard deviation (2 σ) between those two intervals and finally converted this into the standard deviation of the mean using $\bar{\sigma} = 2\sigma/2\sqrt{N}$, where N is the number of points used. The uncertainty in the phase zero point (Eq. 4.2) may underestimate the true errors since they do not include systematic effects and random errors and since the eclipse of EC21178-54 is asymmetric. Improved results may be achieved by using other methods such as least-squares fitting.

4.2 Spectral analysis

All the individual continuum-normalized spectra are shown in Appendix A. In this section we will discuss phase-resolved spectroscopy of EC21178-54 of the different data sets.

4.2.1 Average spectrum of EC21178-54

The average continuum-normalized spectrum of EC21178-54 in 2011 October and 2011 September is shown in Figure 4.3 (top, middle and bottom panels). All the identified lines are marked and labelled. The blue spectrum (Figure 4.3 top and middle panels) is dominated by the emission line from HeII 4686Å (strongest feature). The strength of the HeII 4686Å emission line is typical of a NL system with a high rate of mass-transfer (Szkody et al. 2004). The Balmer lines (H_β, H_γ, H_δ down to H_{10}) are clearly present with an increasing absorption component towards the blue end of the spectrum. Balmer emission was more pronounced in 2011 October in H_β, H_γ, H_δ, and H_ϵ. The HeI lines (at 4026 Å, 4471 Å, 4921 Å, and 5015 Å) all have a strong absorption component. The CIII/NIII blend at 4640-4650 Å and CII at 4267 Å are clearly seen in emission. In addition, the blue spectrum shows absorption and emission of HeII (at 4200 Å and 4542 Å, part of the HeII Pickering series) as well as absorption from MgI at 5175 Å. Also visible are the CaII lines (at 3933 Å and 3969 Å) towards the blue part of the spectrum in absorption. The red spectrum (Figure 4.3 bottom panel) is dominated by H_α in emission; HeII 5411Å and HeI at 5875 Å and 6678 Å are seen in emission with an absorption core.

In Figure 4.4 we compare the average continuum-normalized blue spectra of EC21178-54 over three different epochs. The average spectrum of 2011 October (Figure 4.4 bottom

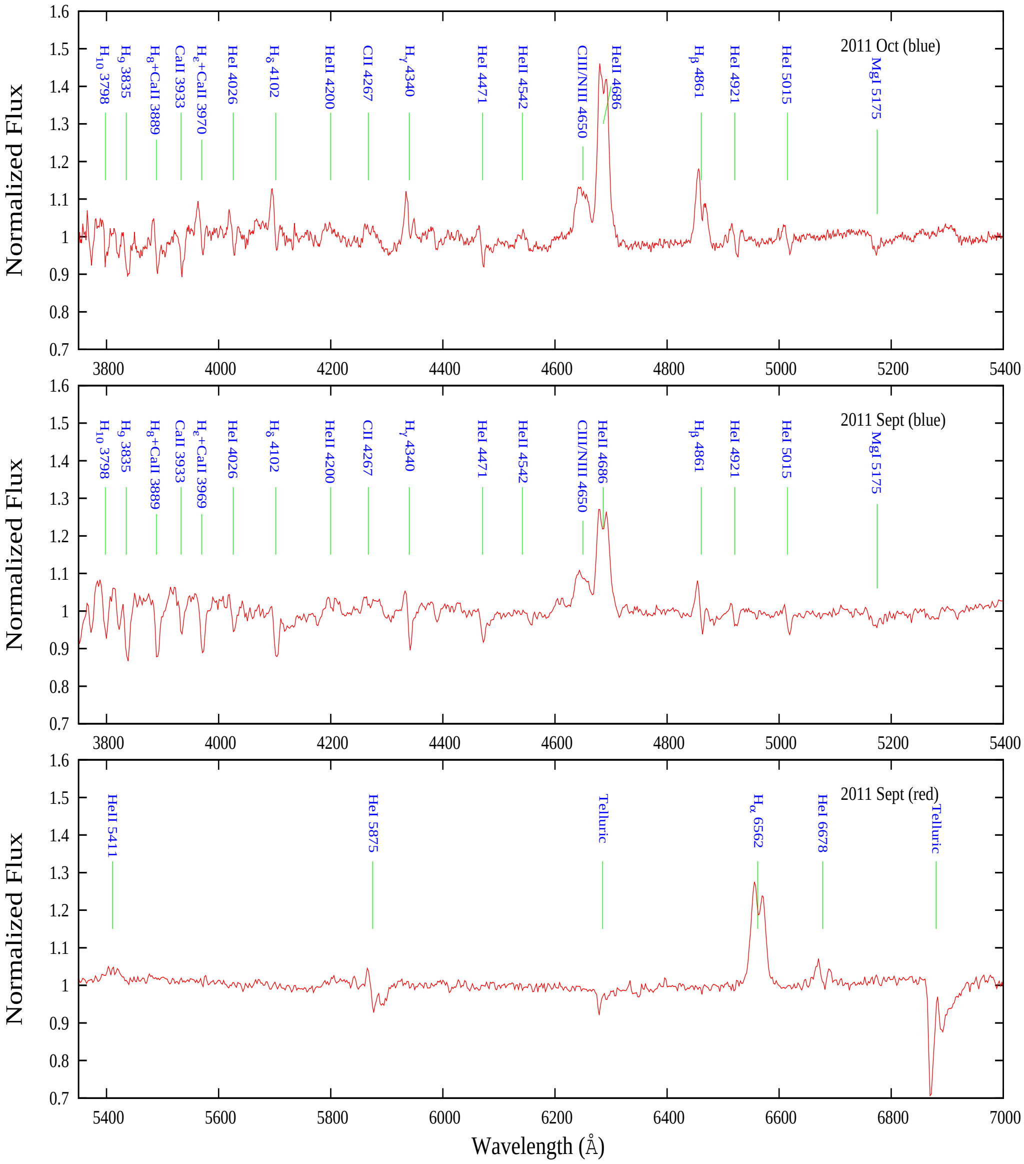

Figure 4.3: The average continuum-normalized spectrum of EC21178-54 from two different data sets. The top panel is from the 2011 October 22-23, the middle and bottom panels are from 2011 September 5. The prominent lines have been marked and labelled.

panel) shows double-peaked and broad emission features from the Balmer lines (H_β and H_γ), which suggest that these lines originate in an accretion disc. H_δ and H_ϵ show two peaks (one peak in absorption and the other in emission), with the redshifted peak in absorption and the blueshifted peak in emission. The blueshifted peaks of the Balmer lines (H_β and H_γ in particular) are stronger than the redshifted peaks. This effect has been observed in other CVs such as the dwarf nova V2051 Oph (Steeghs et al. 2001) but they did not attempt an

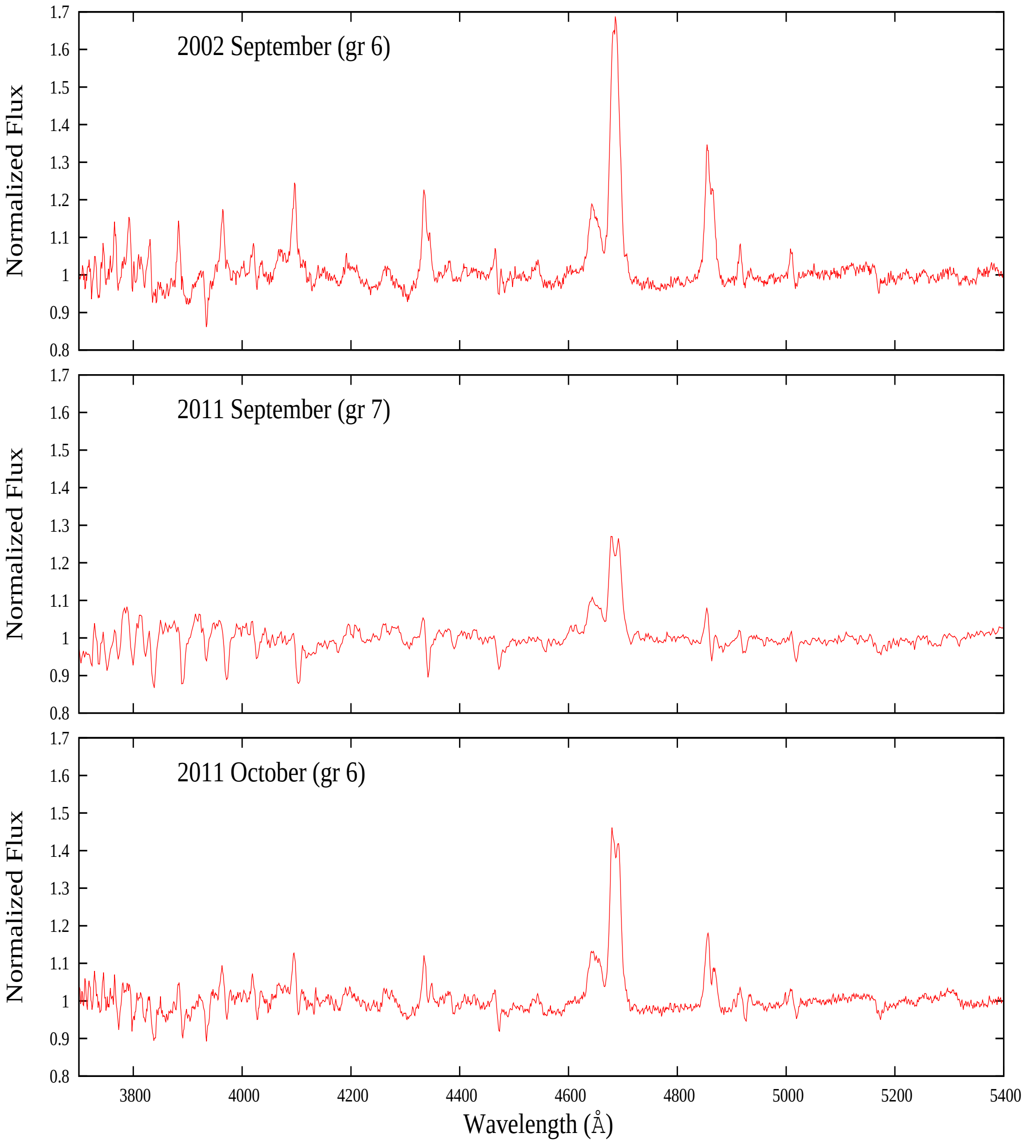

Figure 4.4: The average spectrum of EC21178-54 at three different epochs. The top panel is from 2002 September 7, the middle panel is from 2011 September 5, and the bottom panel is from the 2011 October 22-23 data.

interpretation other than that the blue side of the accretion disc could be making a larger contribution to the emission. The same effect is also seen in H_δ and H_ϵ where the blueshifted components in emission dominate the redshifted components in absorption.

The spectral features of EC21178-54 discussed above are different for different epochs, e.g. Figure 4.4 (top panel) shows a spectrum dominated by emission with very little absorption, whereas in Figure 4.4 (middle panel) more absorption features are seen from HeI 4471Å down to H_{10}. The bottom panel of Figure 4.4 shows the intermediate state, where both emission and absorption are present in the average spectrum. Thus this system changes from mostly emission (2002 September), to absorption (2011 September), and then to mixed absorption and emission a month later in 2011 October. This is somewhat unexpected given that the out-of-eclipse brightness of EC21178-54 is similar in 2002 September and 2011 October (see Section 4.1). This would exclude large variations in mass-transfer rate as a dominant source for the spectral variations.

4.2.2 Phase-binned spectra of EC21178-54

Figures A.2 to A.6 in Appendix A show the 55 individual spectra of EC21178-54 obtained from 2002 September to 2011 October folded on to the orbital phase according to the ephemerides given in Section 4.1 (Eqs. 4.1 and 4.2). The orbital phase increases from bottom to top, with $\phi \simeq 0.0$ at the bottom of each figure and $\phi \simeq 0.95$ at the top for each figure. We placed all the spectra with $\phi > 0.95$ at the bottom not only because they contains the strongest emission features but because they are closely associated with the primary eclipse, see also Figure 4.2 (right panel). The spectral features in the five figures are similar even though they vary from one observation to the next.

All the spectra from the three data sets (2002 September, 2011 September, and 2011 October) were then averaged into 10 separate phase bins using the ephemeris and orbital period given by Eqs. (4.1) and (4.2). The phase bin centred at $\phi = 0.0$ includes spectra around orbital phase $0.95 \leq \phi < 0.05$, the bin centred at $\phi = 0.1$ includes all spectra around phase $0.05 \leq \phi < 0.15$, etc. The results are shown in Figures 4.5 to 4.7 with the phases labelled on each spectrum. The discussion of the individual figures follows below.

We managed to find four phase bins ($\phi = 0.1$, 0.2, 0.3, and 0.8) from the seven spectra obtained in 2002. Unfortunately there were no spectra taken just before and during the eclipse (see Figure 4.5). The spectra in Figure 4.5 revealed that the Balmer lines are double-peaked in emission from $\phi = 0.1$ to 0.8. The higher Balmer lines, H_δ, H_ϵ, H_8 and H_9, at $\phi = 0.8$ each show two components, the redshifted absorption and the blueshifted emission peak. HeII 4686Å is also double-peaked and shows strong emission. The HeI lines appear in emission either double- or single-peaked from $\phi = 0.1$ to 0.3, and in absorption at $\phi = 0.8$, but HeI 4471Å has a central absorption dip throughout the orbital phases.

Figure 4.6 shows the phase-binned spectra from 2011 September observations folded into one orbital cycle of EC21178-54. HeII 4686Å is also double-peaked and shows strong emission throughout the orbital cycle as before. The Balmer lines are double-peaked and appears in emission at phase zero. At $\phi = 0.1$ to 0.2, H_β and H_γ are in emission, whereas the other lines in the Balmer series are in absorption. From $\phi = 0.3$ to 0.9, H_γ and all the higher Balmer series are seen in absorption, which increases in strength with the orbital phase until phase 0.8. The HeI lines show similar behaviour as that of the higher Balmer series, they appear in emission at $\phi = 0.0$ to 0.1, and then progress in absorption for the

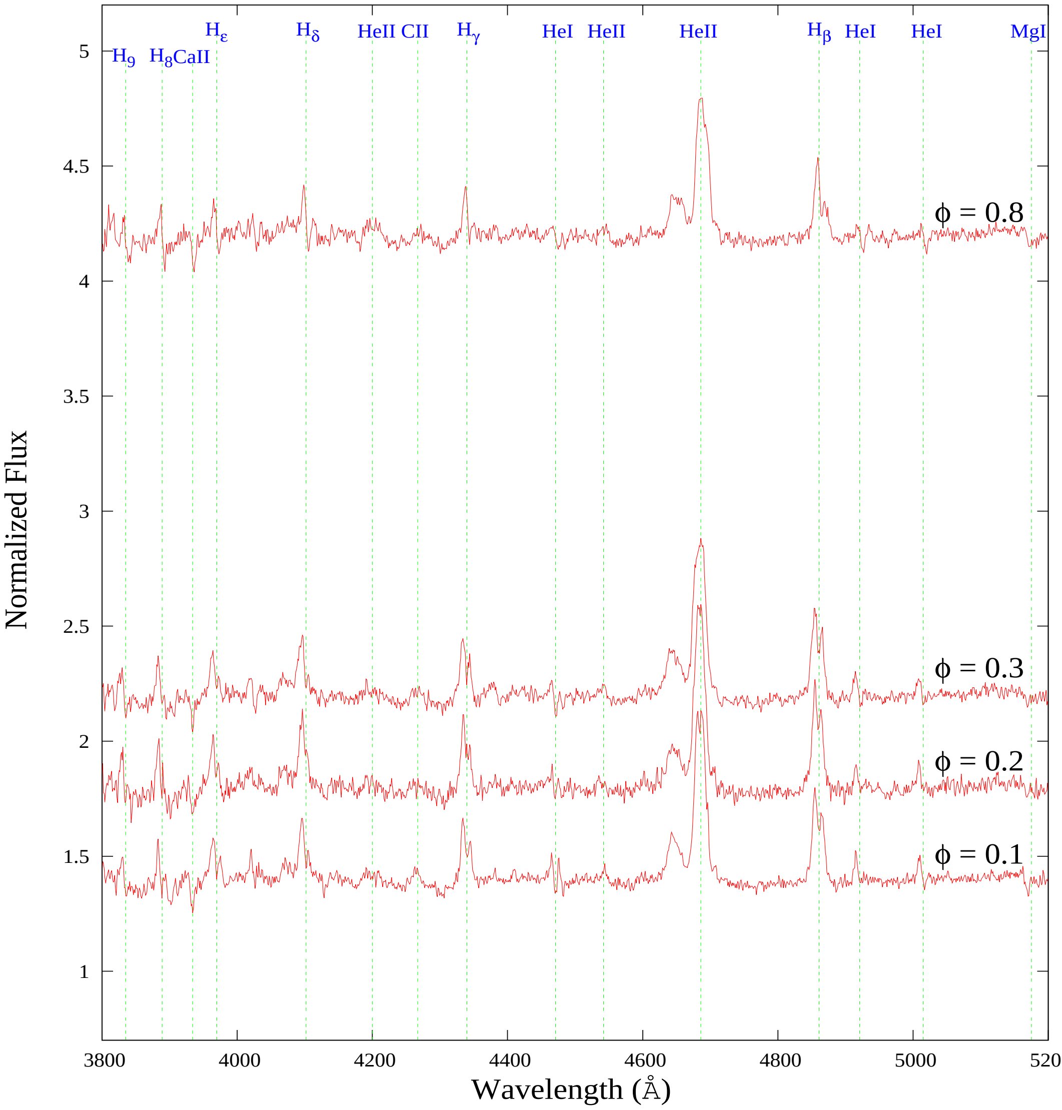

Figure 4.5: The phase-binned spectra of EC21178-54 taken on 2002 September 7 arranged in orbital phase from bottom $\phi = 0.1$ to top 0.8. All spectra have been normalized to the continuum level and the flux of each spectrum has been shifted from bottom to top by $\Delta flux = 0.4$ for display purpose.

remainder of the orbital phases. H_β shows double-peaked emission from 0.0 to 0.4 which weakens with the increase in the orbital phase. But at phases 0.6, 0.8, and 0.9 absorption dominates. We also note that MgI 5175Å appears in absorption around phases 0.7-0.9.

We generally found similar results from the data obtained in 2011 October (see Figure 4.7). It is clear from the figure that the spectra of EC21178-54 vary in both absorption and emission features throughout the orbital phase. At $\phi = 0.0$, the Balmer lines, HeII 4686Å, and HeI lines are seen in pure emission. This happens because the secondary star

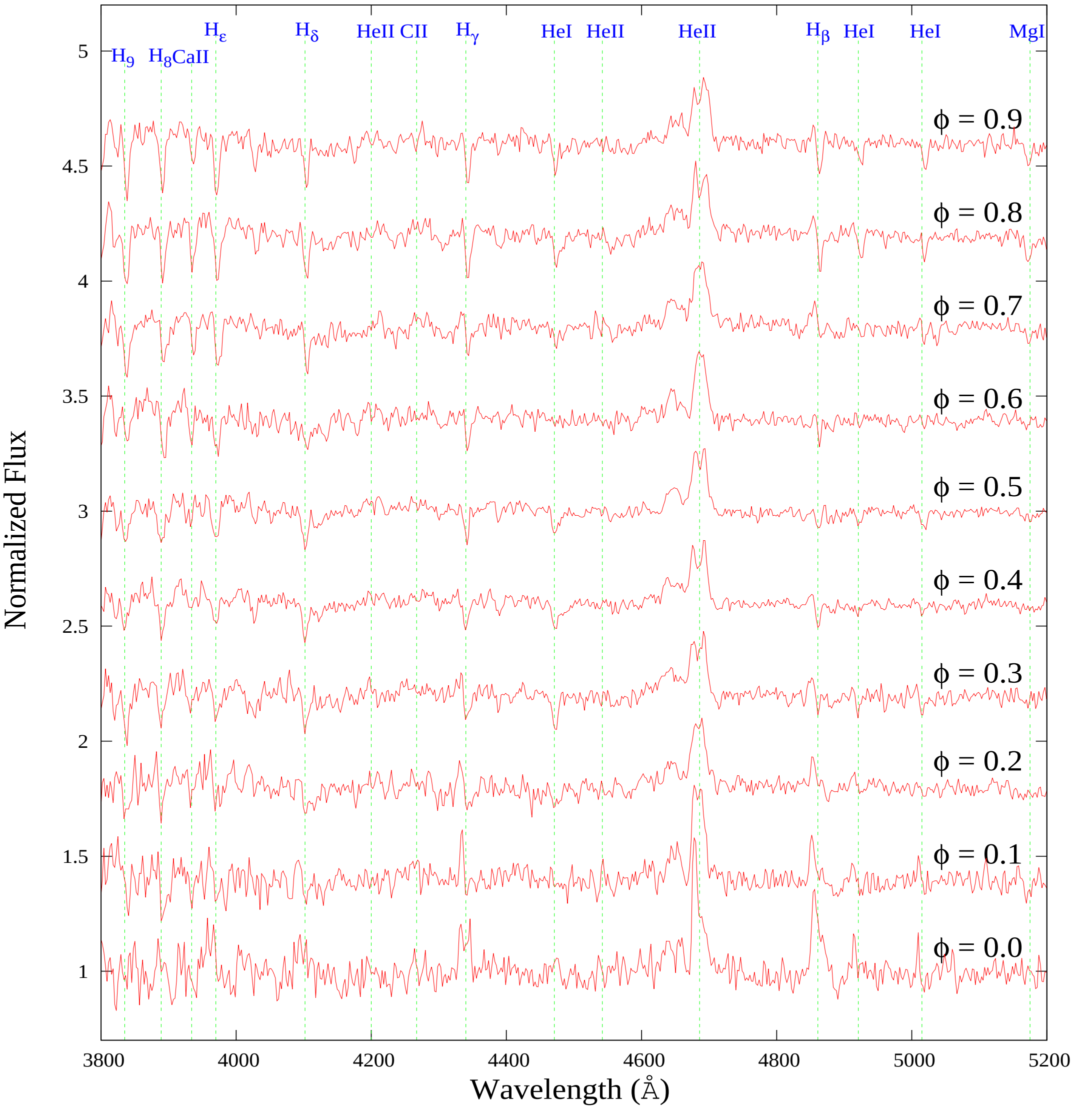

Figure 4.6: The phase-binned spectra of EC21178-54 taken on 2011 September 5 arranged in orbital phase with $\phi = 0.0$ at the bottom and $\phi = 0.9$ at the top. All spectra have been normalized to the continuum level and the flux of each spectrum has been shifted from bottom to top by $\Delta flux = 0.4$ for display purpose.

has partially eclipsed the bright spot and part of the accretion disc. But as the orbital phase increases, $\phi = 0.1$-0.8, absorption and emission lines are observed. In 2011 October, H_β, H_γ, and HeII 4686Å were always double-peaked in emission, with the exception of $\phi = 0.8$ where the former appear single-peaked. The other Balmer series, H_δ and H_ϵ, switches from emission ($\phi = 0.0$ to 0.5) to absorption ($\phi = 0.5$ to 0.9). The HeI lines behave in the same way as the Balmer series beyond H_β, but for HeI lines, absorption occurs starting at $\phi = 0.3$, weakens until phase 0.5, and then increases again and reaches maximum at phase 0.9.

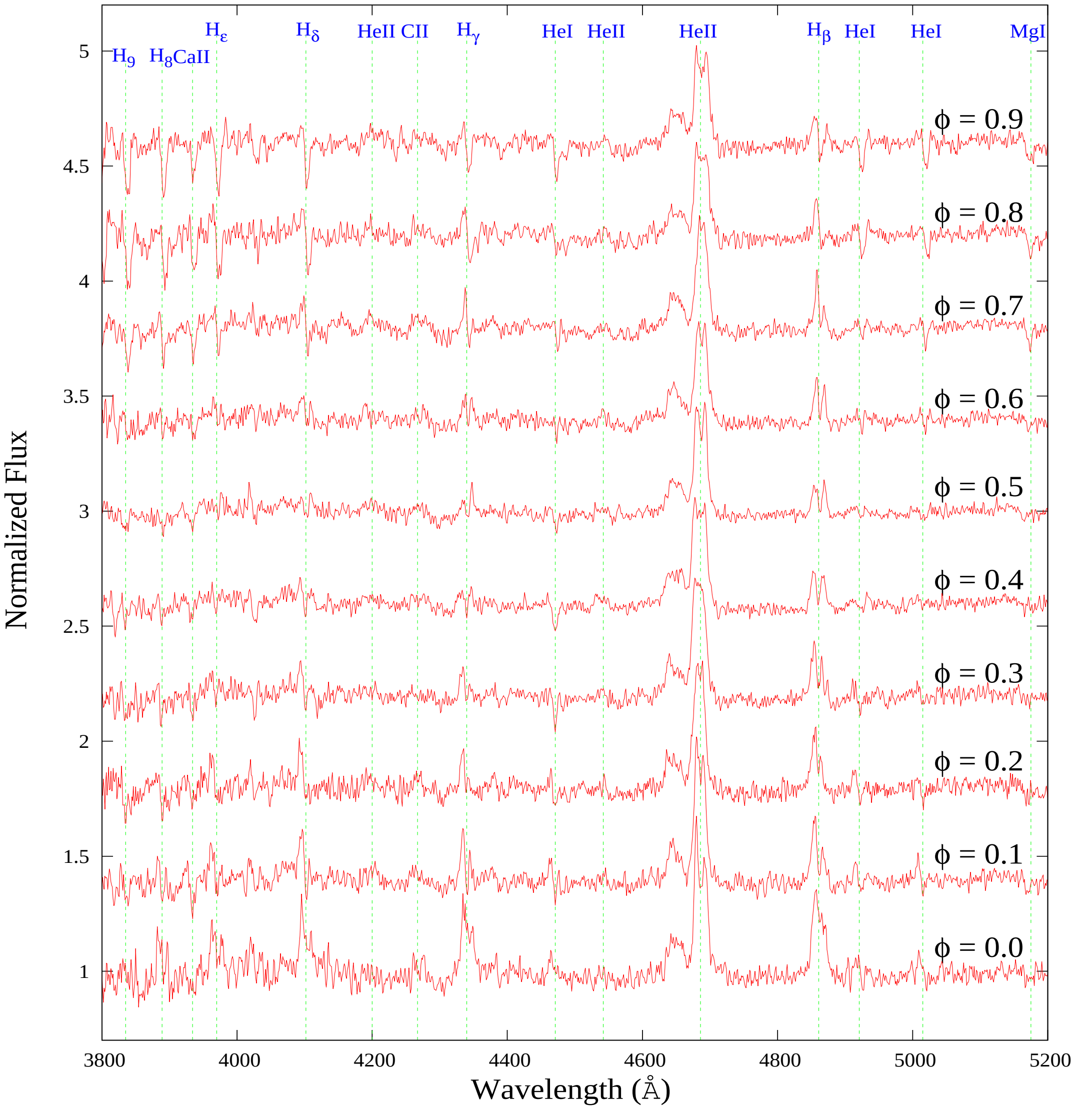

Figure 4.7: The phase-binned spectra of EC21178-54 taken on 2011 October 22-23 arranged in orbital phase with $\phi = 0.0$ at the bottom and $\phi = 0.9$ at the top. All spectra have been normalized to the continuum level and the flux of each spectrum has been shifted from bottom to top by $\Delta flux = 0.4$ for display purpose.

Again, we see the MgI 5175Å line appear in absorption only around phase $0.75 < \phi < 0.9$, prior to eclipse.

Generally, the spectra of EC21178-54 show strong emission in 2002 September (Figure 4.5), strong absorption in 2011 September (Figure 4.6), and mixed absorption and emission in the higher Balmer series (H_β to H_ϵ) and the HeI lines in 2011 October (Figure 4.7). This could be attributed to a change in mass transfer rate between the individual observations but could also be due to the varying strength of the absorption component. The other spectral features that are present also vary from one observation to the other. In addition, one peculiar aspect of the 2011 October data, is that the higher Balmer series show a change to strong absorption at phase 0.7-0.9. This was also observed for SW Sex (Groot et al. 2001). We discuss this further below.

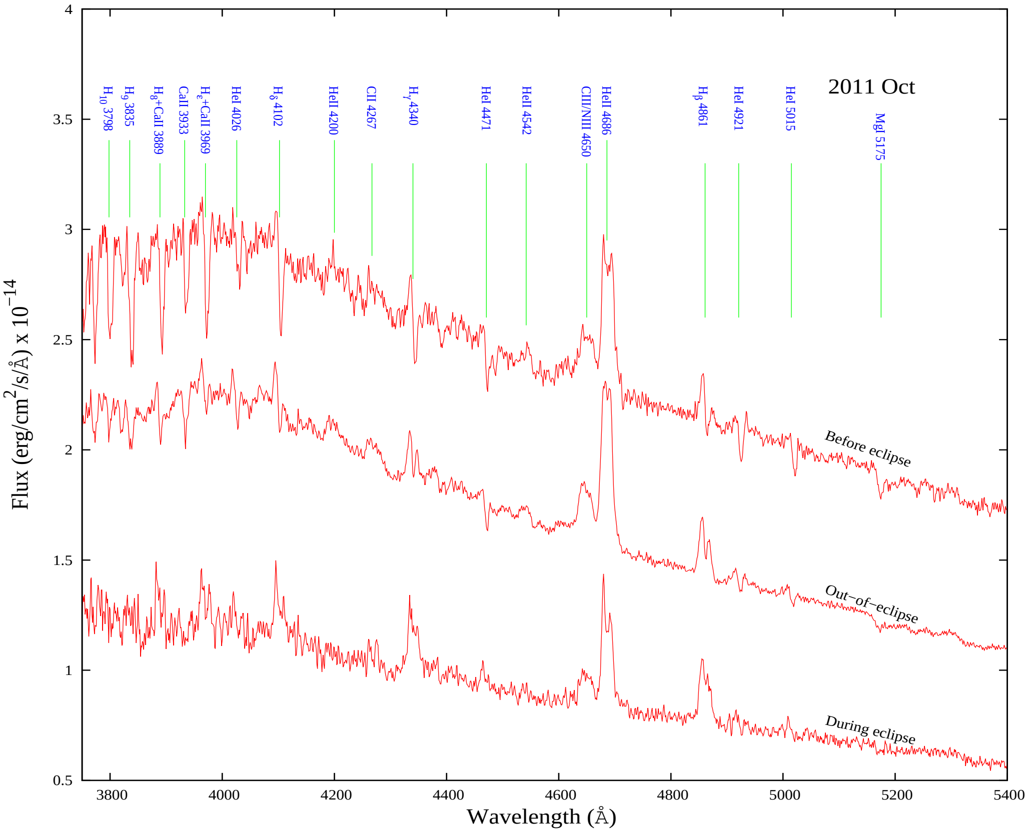

Figure 4.8: The average spectrum of EC21178-54 at phase intervals $0.75 \leq \phi < 0.95$ (top, offset by $+7 \times 10^{-15}$), $0.05 \leq \phi < 0.75$ (middle) and $0.95 \leq \phi < 1.05$ (bottom). The prominent lines have been marked and labelled.

In Figure 4.8, we plot the average flux-calibrated spectrum of EC21178-54 (2011 October) at three different phase bins: before the eclipse ($0.75 \leq \phi < 0.95$), during the eclipse ($0.95 \leq \phi < 0.05$), and out-of-eclipse ($0.05 \leq \phi < 0.75$). It is clear from the figure that the spectrum changes substantially with orbital phase. The continuum shape of the spectrum obtained during mid-eclipse (bottom of Figure 4.8) is slightly flatter than the other two; this was also observed by Zietsman in 2006 (Zietsman 2008). The Balmer series, HeII 4686Å, HeI lines, and CIII/NIII (blend at 4650 Å) are present and double-peaked in emission. The strength of the HeII 4686 line and the CIII/NIII blend are reduced during eclipse, whereas that of the Balmer lines are enhanced. This indicates that the former lines originate close

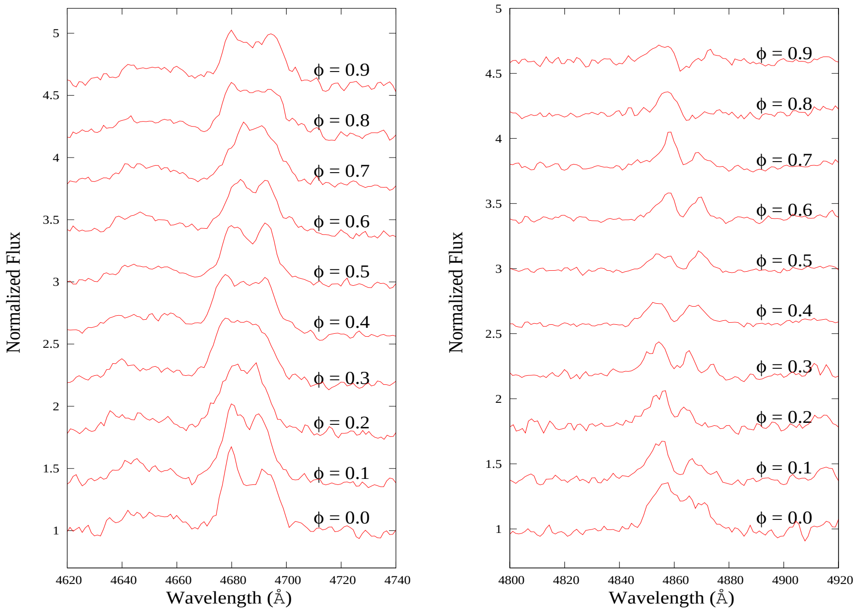

(a) HeII 4686Å (b) H_β

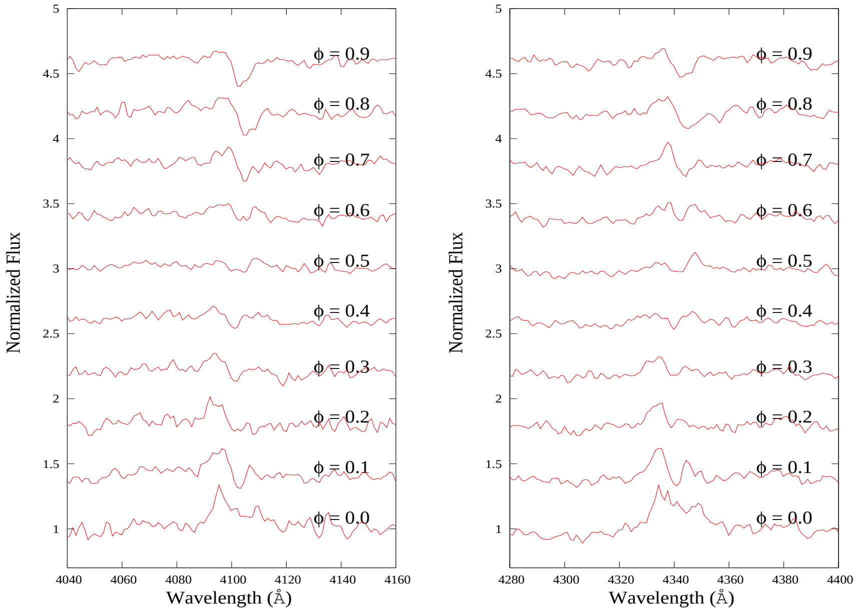

(c) H_δ (d) H_γ

Figure 4.9: The phase-binned line profiles (clockwise from top left) of HeII 4686Å, H_β, H_γ, and H_δ for comparison of the orbital cycle S-waves. All spectra have been normalized to the continuum level and the flux of each spectrum has been shifted from bottom to top by $\Delta flux = 0.4$ for display purposes. The spectra are from the 2011 October 22-23 data set.

to the WD and the inner accretion disc, and they are more affected by the eclipse.

The out-of-eclipse spectrum of EC21178-54 (Figure 4.8 middle) is similar to the average spectrum shown in Figures 4.3 (top panel) and 4.4 (bottom panel) with strong and broad double-peaked emission lines from the Balmer and HeII 4686Å lines. HeI lines and CIII/NIII blend at 4650 Å are also present in broad emission and/or absorption on a steep continuum. The ratio of HeII 4686Å over H_β is larger than unity, and the presence of HeII 5411Å, suggest that this emission lines are formed in a region with a higher than usual level of ionization (Groot et al. 2001).

The spectrum of EC21178-54 obtained before the eclipse (Figure 4.8 top) revealed that the higher Balmer lines (H_ϵ to H_{10}) change from general emission between phases $0.05 \leq \phi < 0.75$ to absorption at phases $0.75 \leq \phi < 0.95$. This has been observed during the low state of SW Sex (Groot et al. 2001) and recently in UX UMa (Neustroev et al. 2011), and is attributed to contribution from the bright spot. Thus the higher Balmer lines likely originate from the vicinity of the bright spot which is clearly visible at phases $0.75 \leq \phi < 0.95$, see e.g. Figure 15 of Groot et al. (2001). The high excitation features, HeII 4686Å, CIII/NIII blend at 4650 Å and CII 4267Å, do not change in strength compared to the continuum and each other. However, H_β, H_γ and H_δ, each have two components: the redshifted absorption peak and the blueshifted emission peak. But the absorption is stronger than the emission, which is the opposite of what was seen for H_δ and H_ϵ at earlier phases. Furthermore, the HeI lines also change from emission and broad absorption to strong absorption.

Finally, in Figure 4.9 we take a closer look at some of the strongest spectral features that are seen in the average spectrum of EC21178-54 in 2011 October to further investigate their variations with the orbital phase. Figure 4.9(a) show phase-binned line profiles of HeII 4686Å. It is clear that the HeII 4686Å line is variable with the orbital phase and it is always present in emission. It is double-peaked at most orbital phases, yet the position and the separation between the two peaks varies (smaller at $\phi = 0.2$ and largest around $\phi = 0.4$). The width of the profile also varies slightly (narrow at $\phi = 0.5$). The H_β line, Figure 4.9(b), shows similar broad variable double-peaked emission profile in most orbital phases except at $\phi = 0.8$, where the redshifted peak is absent or in absorption. It shows a central absorption dip which get deeper with increasing orbital phases. The blueshifted peak of the double-peaked profile dominates over the redshifted peak at almost all the phases except at $\phi = 0.4$ to 0.6, where the two peaks are comparable in strength. The H_γ and H_δ line profiles, Figures 4.9(d) and (c) respectively, reveals a similar structure to that of H_β. These two lines show broad variable double-peaked emission profiles at most orbital phases with the exception of $\phi = 0.7$-0.9, where only one emission peak is seen. The absorption dip seems stronger and increases with increasing orbital phase. At most phases the blueshifted component dominates over the redshifted component except at $\phi = 0.4$ to 0.6, where the redshifted component appear stronger (see Figure 4.9(c) and (d)).

4.3 Radial velocities of emission lines

The average spectrum of EC21178-54 (Figures 4.3 to 4.4) shows strong emission at the wavelengths of the Balmer lines (H_α and H_β in particular) and helium lines (e.g. HeII 4686Å). These lines are produced in the accretion disc which surrounds the WD, so variation in their velocity hold information on the motion of the WD (see Southworth et al. 2009, 2007a,b, and references therein). However, spectroscopic studies of CVs often show a phase difference between the variation of radial velocities of emission lines and the orbital phases measured using other methods (Thorstensen 2000, Thoroughgood et al. 2005, Unda-Sanzana et al. 2006, Steeghs et al. 2007). This has casts some doubts as to whether emission lines are good indicators of the motion of the WD, and as such the physical properties of the system derived from emission lines radial velocities is unreliable (Southworth et al. 2009).

Two methods were implemented to measure radial velocities from the strongest spectral features of EC21178-54 namely: using `SPLOT` routines in `IRAF`, and using `RVEL` in `MOLLY`[1] to measure radial velocities from the wings of the emission lines. These methods are discussed below:

4.3.1 Using `SPLOT` in `IRAF`

To measure radial velocities of the line profiles, I used the `IRAF` task `SPLOT`; `SPLOT` can be used for blended lines as well as single lines. For single-peaked lines, I marked two positions on either side of the emission lines with the letter “k”, and `SPLOT` automatically fits a single Gaussian and writes the results in a log file. In the case of a double-peaked emission lines, there are three fitting functions available: a “Gaussian”, a “Lorentzian”, and a “Voigt” profile. This is an interactive task and care was taken as to select the correct line, the best approximation of the centre; the two points were aligned to avoid skewed or different flux level.

I chose a Gaussian function for all the double-peaked lines and marked the two positions on either side of the emission lines with the letter “d” and then mark the centre of each peak with the letter “g”. `SPLOT` fits both lines simultaneously and ignores background fitting. This task writes the name of the frame, central wavelengths of the two double-peaked lines, flux, equivalent width, and the flux width at half maximum to a log file, which is easily accessible for further analysis of the radial velocities. A simple program was then written in `Python` that reads the log files (i.e., the file created above, and another file, which contains the header of the images, e.g. frame name, UT (universal time), HJD, Exposure time, RA (right ascension) and Dec (declination), and computes the radial velocity (V_r) of each lines using Eq. (4.3) below:

$$V_r = \left(\frac{\lambda_{\text{centre}} - \lambda_{\text{rest}}}{\lambda_{\text{rest}}} \right) \times c \tag{4.3}$$

---

[1] MOLLY and PAMELA (not used here) are software written by Tom Marsh and can be obtained from http://www.warwick.ac.uk/go/trmarsh

where $\lambda_{\rm rest}$ is the laboratory rest wavelength, $\lambda_{\rm centre}$ is the central/observed wavelength, and c is the speed of light.

4.3.2 Results using `SPLOT` in `IRAF`

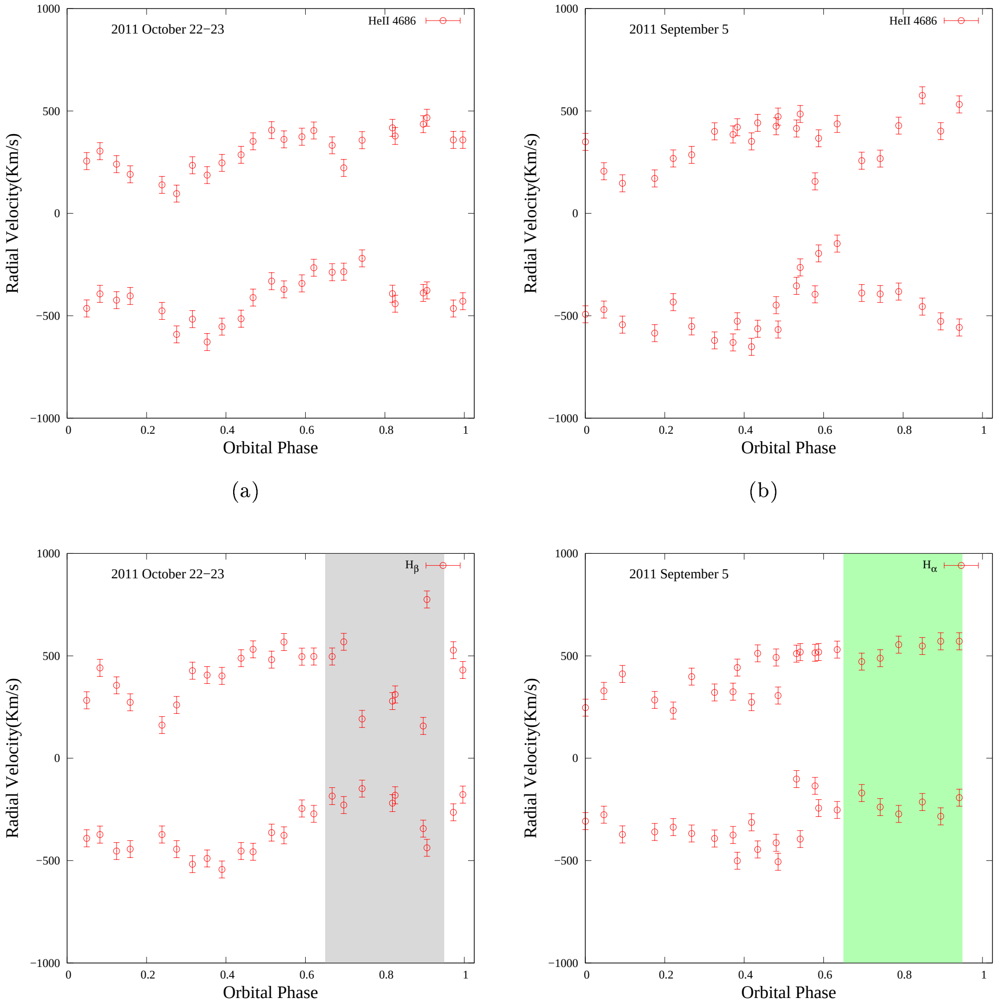

(a) (b)

(c) (d)

Figure 4.10: Radial velocity curves of HeII 4686Å (top panels), H_α (bottom right), and H_β (bottom left). The curves on the left panels are from the 2011 October 22-23 data, whereas the curves on the right panels are from the 2011 September 5 data. The vertical area shown in green and grey marks the radial velocities affected by the absorption component.

The top panels of Figure 4.10 show the radial velocity (RV) curves of the HeII 4686Å line for all the 48 spectra obtained from using `SPLOT` routines in `IRAF`. Figure 4.10(a) show the RV curve from 2011 October 22-23. It is clear from the figure that the RV curve shows a sinusoidal variation in both the blueshifted and redshifted components. The two components are moving in phase with each other from $\phi = 0.0$ to 0.6, but after $\phi = 0.6$ the two components appear to move in anti-phase. The same behaviour is seen in Figure 4.10(b) (2011 September 5), but in this case the two components appear to move in anti-phase from phase 0.2 onwards. We suspect that at $\phi \approx 0.7$ in Figure 4.10(a), the redshifted component crosses to become blueshifted, whereas the blueshifted component crosses to become redshifted, but this is not very clear because there were few spectra. This becomes clearer in Figure 4.10(b), where the two RV curves come close to within 200 km/s of each other around phase $\gtrsim 0.6$. The errors in the radial velocities were propagated using the standard formalism for propagating uncertainty and includes the measurement errors from `SPLOT` and the RMS uncertainty of the wavelength calibration. These errors may underestimate the true errors since they do not include systematic errors.

The bottom panels of Figure 4.10 show the RV curves for the Balmer lines also measured from `SPLOT` routines in `IRAF`. Figure 4.10(d) show RV curves of the H_α line from the spectra obtained on the 2011 September 5. Figure 4.10(c) show the RV curves of the H_β line from 2011 October 22-23 spectra. The RV curve of the H_β line shows a sinusoidal variation which becomes disrupted after $\phi \geq 0.7$. The reason for this is that at this orbital phase ($\phi \sim 0.7$) the redshifted emission peak switches to absorption. The blueshifted peak remains sinusoidal in shape. In general, the RV curves from one observation show similar variation which become disrupted after $\phi \approx 0.7$ where absorption dominates in the Balmer lines, e.g. the left panels of Figure 4.10 looks very similar for orbital phases smaller than 0.7. Similar results are seen in the right panels of Figure 4.10. `SPLOT` allows a first look at the behaviour of the radial velocities, but a better way to measure RV variations is using `RVEL` in `MOLLY` (next Section).

4.3.3 Using `RVEL` in `MOLLY`

We measured radial velocities from the HeII 4686Å and the H_α line, which are the strongest emission lines, using the double-Gaussian method (Schneider & Young 1980) as implemented in `MOLLY`. The full width at half maximum (FWHM) of the Gaussian was set to 600 km/s. This is a good compromise between resolving noise and emission-line features and also minimizing the random noise in the radial velocities measurement (Southworth et al. 2009). The separation of the two Gaussians, ξ, was varied from 800 km/s to 3000 km/s in intervals of 100 km/s. For each value of ξ, a spectroscopic orbit was fitted to measured radial velocities using the Spectroscopic Binary Orbit Program (SBOP[1], provided by John Southworth[2], priv. communication), which was written by Wolfe et al. (1967) and was modified and expanded by Etzel (2004) to allow for the solution of any combination of orbital parameters, simultaneous solution of double-lined binaries, and provide a more robust treatment of high orbital eccentricities. It gives reliable error estimates for the optimized parameters

---

[1] The Spectroscopic Binary Orbit Program, is a Fortran 77 Code with a very long history considerably modified and extended by Etzel (2004). More details can be found at http://mintaka.sdsu.edu/faculty/etzel/.

[2] John Southworth is a lecturer and Science & Technology Facilities Council Advanced Fellow working in the Astrophysics Group at Keele University, UK.

(Southworth et al. 2005). The orbital period was fixed at the ephemeris given in Section 4.1 (Eq. 4.2). A circular orbit was assumed, and the phase zero-point was included as a fitted parameter. Radial velocities between phases 0.9 and 0.1 were not rejected since we had only 24 spectra per epoch even though they are affected by the eclipse of the accretion disc.

4.3.4 Results using `RVEL` in `MOLLY`

The radial velocities of HeII 4686Å and H_α line were measured using `MOLLY` for two of the three data sets (i.e., 2011 October 22-23 and 2011 September 5). We have constructed three diagnostic diagrams for EC21178-54, shown in Figures 4.11 to 4.13 (Shafter 1983, Shafter et al. 1986). They show that the properties of the spectroscopic orbit of EC21178-54 changes slowly for ξ = 1100 - 1800 km/s. The lowest scatter in the residuals (σ_{rms}) occurs for ξ = 1300-1700 km/s in Figure 4.11 (HeII, 2011 October), 1400-1800 km/s in Figure 4.12 (HeII, 2011 September), and 1200-1700 km/s in Figure 4.13 (H_α, 2011 September). We have adopted ξ = 1500 km/s (marked by a black arrow) for each figure for the spectroscopic orbit since they give the reasonable σ_{rms}, and these quantities are given in Table 4.1. The RV curves and the best fitting model are shown in Figure 4.14.

The left panel of Figure 4.14 shows the RV curve of HeII 4686Å obtained for the 2011 October data. It varies sinusoidally and crosses from blue to red at $\phi \sim 0.46$ and again crosses from red to blue at $\phi \sim 0.97$. The velocity centre is at ~ -57 ± 6 km/s (heliocentric). The middle panel of Figure 4.14 shows the sinusoidal RV curve of HeII 4686Å line obtained for the 2011 September data. It crosses from blue to red at $\phi \sim 0.45$ and crosses again from red to blue at $\phi \sim 0.96$. The velocity centre for this curve is at ~ -47 ± 8 km/s (heliocentric). The right panel of Figure 4.14 show the RV curve of the H_α line obtained in 2011 September. It is clear from Figure 4.14 that the RV curve varies sinusoidally with the orbital phase. The velocity centre is at ~ -47 ± 9 km/s (heliocentric). The fit crosses the zero-point from blue to red at $\phi \sim 0.44$ and again passes the zero-point from red to blue at $\phi \sim 0.94$.

However, the RV curves shown in Figure 4.14 are not completely circular. This is reflected by the values of the eccentricities given in Table 4.1, which are consistent with zero. We fixed the orbital period and the ephemeris when determining the best fitting spectroscopic parameters with the SBOP code, whereas the other parameters were allowed to vary. The results obtained for the systemic velocity and the velocity amplitude are consistent for the two data sets used. The average heliocentric systemic (γ) velocity was found to be -50 ± 14 km/s and the average velocity amplitude (K_1) of 143 ± 19 km/s (see Table 4.2). The errors in this two parameters were propagated using the standard errors determined during SBOP fitting and they most likely underestimate the true errors since they do not include systematic effects.

Whilst the results from `SPLOT` revealed the general behaviour of the lines, the `RVEL` method and results conform to the standard analysis of radial velocity variations in compact binaries and gives reliable error estimates when doing a multi-parameter fit.

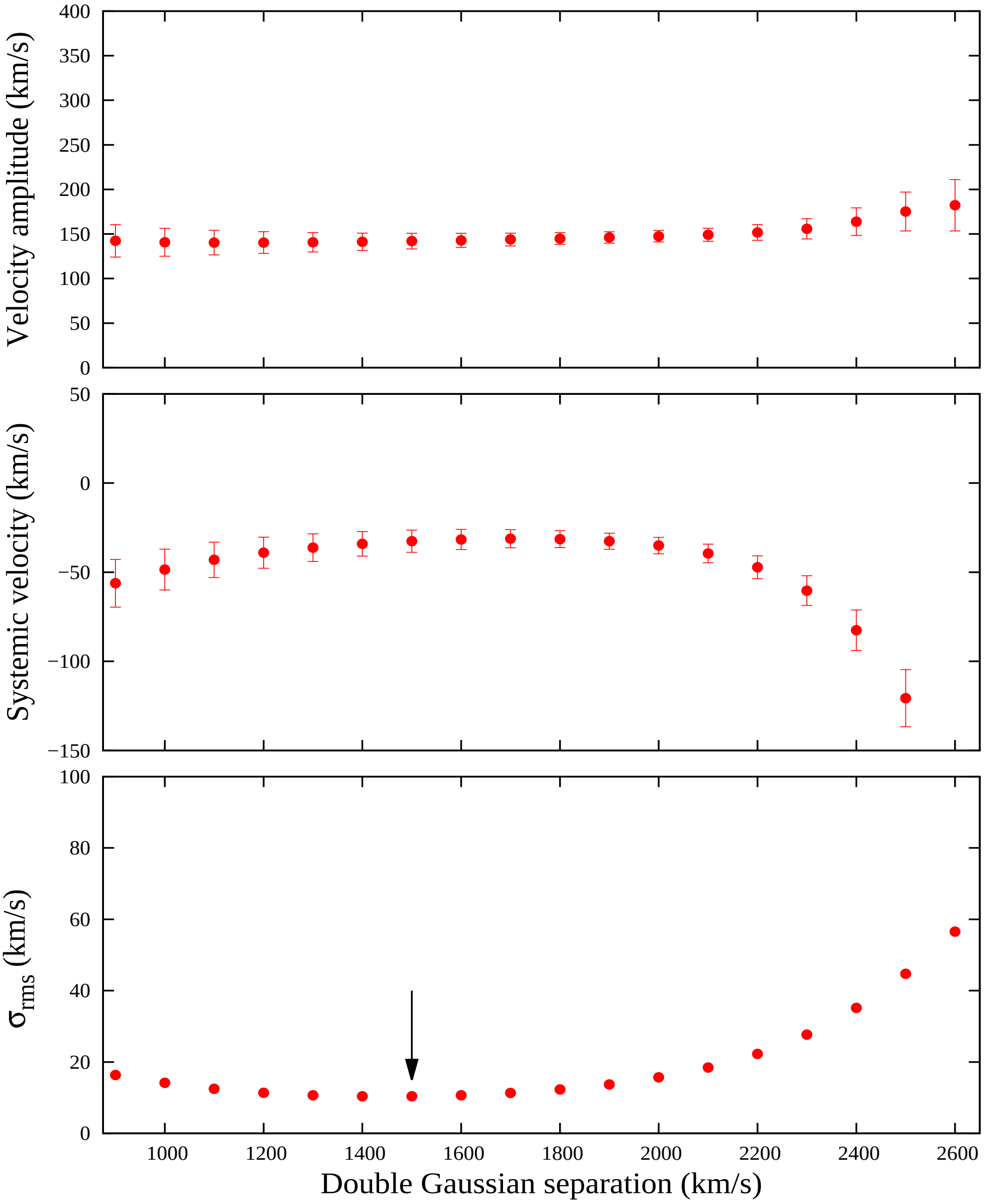

Figure 4.11: A diagnostic diagram showing the variation of the best-fitting spectroscopic orbital parameters for radial velocities of HeII 4686Å measured with a range of separations using the Double Gaussian function. σ_{rms} denotes the scatter of radial velocity measurements around the fitted orbit (2011 October 22-23).

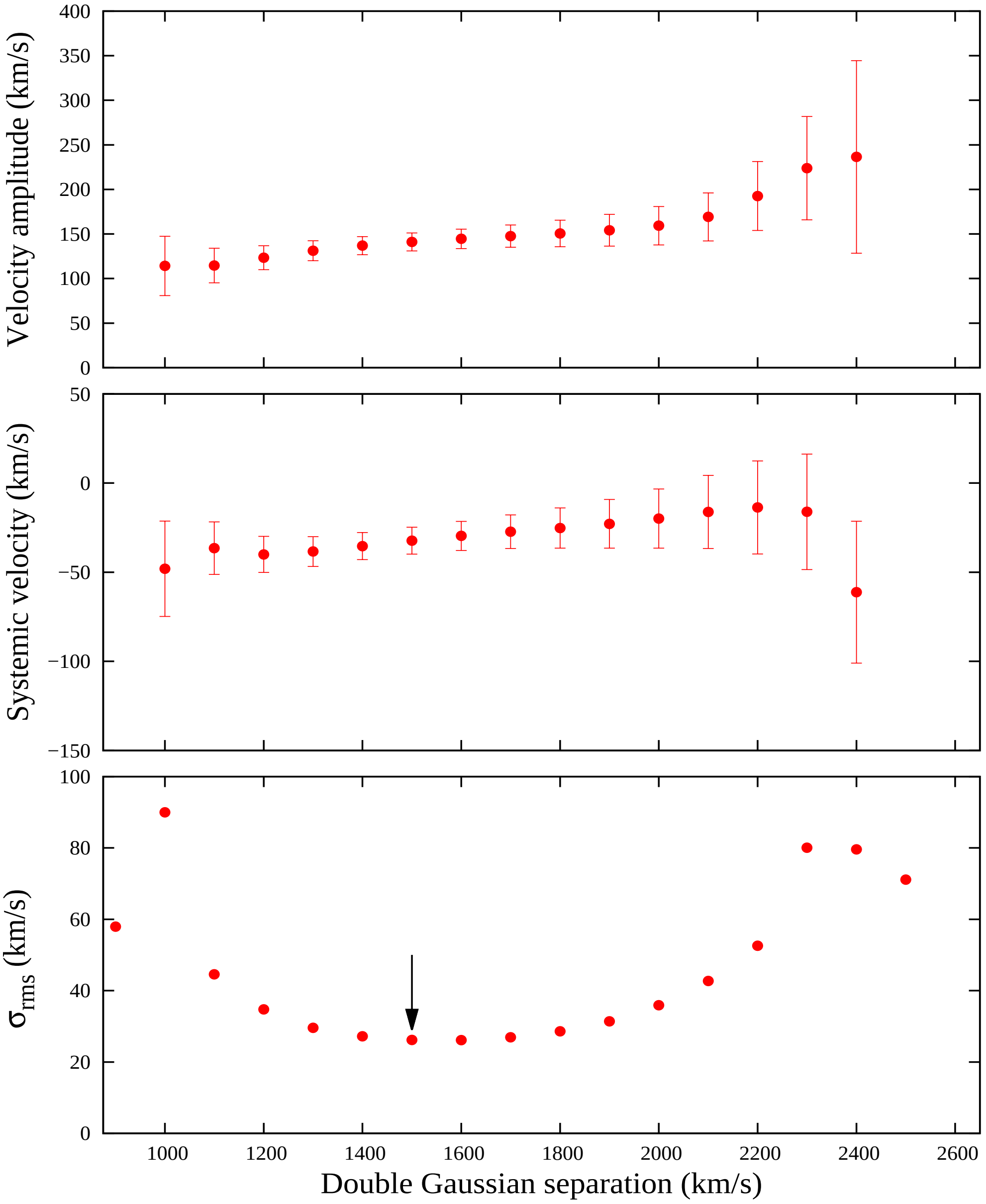

Figure 4.12: A diagnostic diagram showing the variation of the best-fitting spectroscopic orbital parameters for radial velocities of HeII 4686Å measured with a range of separations using the Double Gaussian function. σ_{rms} denotes the scatter of radial velocity measurements around the fitted orbit (2011 September 5).

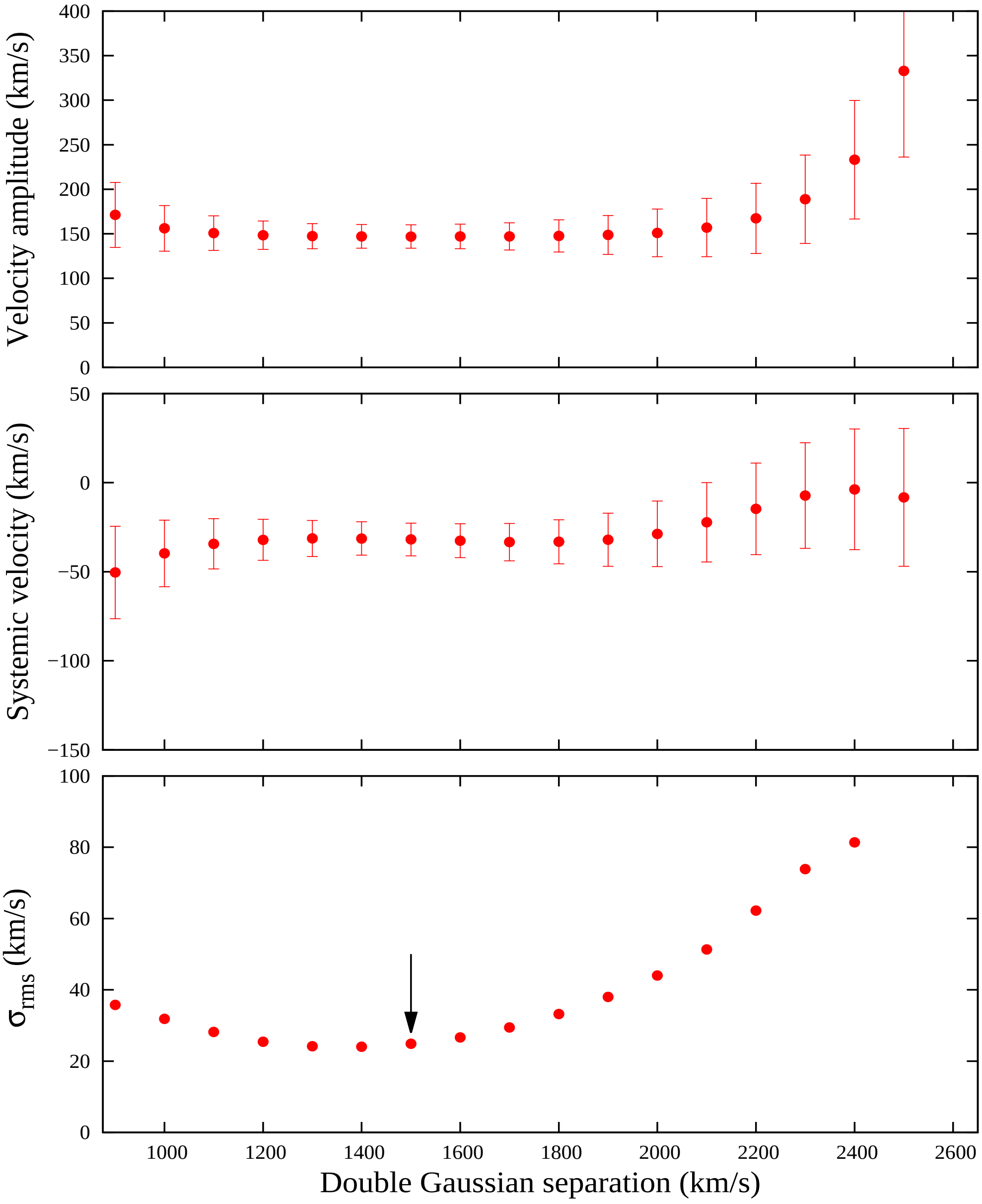

Figure 4.13: A diagnostic diagram showing the variation of the best-fitting spectroscopic orbital parameters for radial velocities of H_α measured with a range of separations using the Double Gaussian function. σ_{rms} denotes the scatter of radial velocity measurements around the fitted orbit (2011 September 5).

Table 4.1: Best-fitting spectroscopic orbits found using the SBOP code.

HeII 4686Å	
(2011 October 22-23)	
Orbital period (d)	0.154525 (fixed)
Eccentricity	0.06 ± 0.07
Reference time (HJD)	2455840.2935 (fixed)
Velocity amplitude K_1 (km/s)	142 ± 9
Systemic (γ) velocity^a (km/s)	-57 ± 6
σ_{rms} (km/s)	10

HeII 4686Å	
(2011 September 5)	
Orbital period (d)	0.154525 (fixed)
Eccentricity	0.02 ± 0.09
Reference time (HJD)	2455840.2935 (fixed)
Velocity amplitude K_1 (km/s)	141 ± 10
Systemic (γ) velocity^a (km/s)	-47 ± 8
σ_{rms} km/s	26

H_α	
(2011 September 5)	
Orbital period (d)	0.154525 (fixed)
Eccentricity	0.03 ± 0.08
Reference time (HJD)	2455840.2935 (fixed)
Velocity amplitude K_1 (km/s)	147 ± 13
Systemic (γ) velocity^a (km/s)	-47 ± 9
σ_{rms} (km/s)	25

[a] The measured systemic γ velocities of each line are in the heliocentric reference frame.

Table 4.2: System parameters of EC21178-54 from spectroscopy

Orbital period (d)	0.154525 (fixed)
Eccentricity	0.04 ± 0.1
Reference time (HJD)	2455840.2935 (fixed)
Velocity amplitude K_1 (km/s)	143 ± 19
Systemic (γ) velocity^a (km/s)	-50 ± 14
σ_{rms} (km/s)	20 ± 5

[a] The mean value of the γ velocity was obtained after correction for the solar motion.

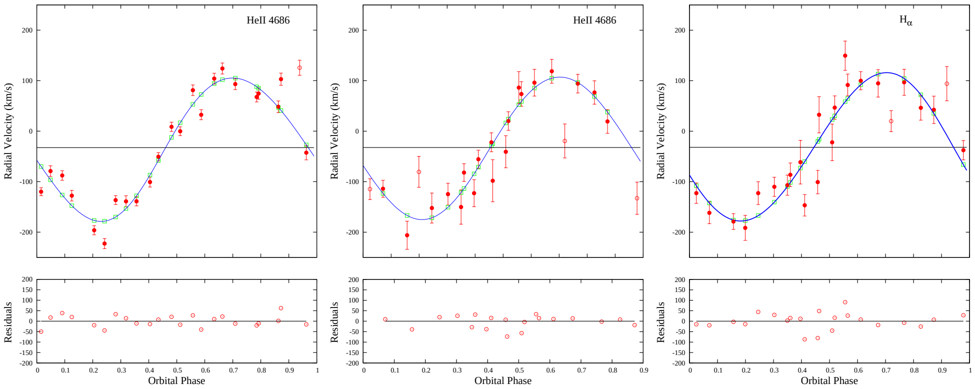

Figure 4.14: The measured emission-line radial velocities (open and closed red circles) of HeII 4686Å and H_α, calculated emission-line radial velocities (open green squares). The solid blue lines show the spectroscopic orbit fitted to the measured radial velocities (closed red circles). The closed red circles indicate data included when fitting the curves. The open red circles are data omitted during fitting because they lie further away from the fit (solid blue line) and when included they cause the fit to be asymmetric. The panel on the left is from the observations of 2011 October 22-23 and the middle and right panels are from the 2011 September 5 spectra.

4.4 Doppler tomography

The final analysis in this Chapter discusses the Doppler tomograms of the strongest emission lines.

4.4.1 Doppler maps

We constructed Doppler maps using the fast maximum entropy method (FMEM[1]) code developed by Spruit (1998), based on Doppler tomography problem by Marsh & Horne (1988). The method and/or procedure used is described below.

We used `IDL`[2] and a `Fortran` code to compute the Doppler maps of EC21178-54. I prepared ascii files which contained the wavelengths and fluxes of EC21178-54 for all spectra using listpix in `IRAF` and combined these with other ascii files which contained all the names and orbital phases of the individual spectra. Then ran the program "foldspec.pro" which sorts all the spectra according to the orbital phase into a trailed spectra folded over two orbital phase/cycle. Next, "dopin.pro" was ran, which require three inputs: the systemic (γ) velocity in cm/s (see Table 4.1), the central wavelengths of the line of interest, and the range of wavelengths that need to be included in the Doppler map. This program (dopin.pro) gives an average spectrum on the screen centred on the line of interest where one uses the cursor to click the two positions, on the left and right of the central wavelength i.e., the section of

---

[1] http://www.mpa-garching.mpg.de/∼henk/pub/dopmap/

[2] The acronym IDL stands for Interactive Data Language and is a trademark of ITT and/or exelis Visual Information Solutions. For further details see http://www.exelisvis.com/ProductsServices/IDL.aspx.

the average spectrum around the line of interest that need to be included in the Doppler map.

The next step was to run the "dopmap.pro" program which calls the `Fortran` code "dop.f" and compute the Doppler maps and plot the results in a postscript file "dopmap.ps" as well as two trailed spectra. The reduced χ^2 obtained ranged between 1 to 1.6, and the specified χ^2 is 1.6. Note that there is no weighting done between the observed and reconstructed trailed spectra, thus all the wavelength bins and phase bins have the same weight (Henk C Spruit, priv. communication). But this can be changed in principle. This means that the results we obtained are accurate since a χ^2 value of zero would mean a perfect fit. In practice a reduced χ^2 of 1 is considered acceptable but this is usually not achieved with Doppler mapping because of a number of assumptions that are made when performing Doppler tomography. For example, a disc is assumed to be perfectly stationary, whereas in reality it fluctuates due to flickering of the hot spot and turbulent in the flow. In addition, it is assumed that the emission is optically thin, but this is not usually the case in the cores of Balmer lines (see Horne & Marsh 1986). Furthermore, it is assumed that the disc is a flat surface, and this becomes problematic for high-inclination systems, where the rim may be obscuring the parts of the disc.

The final step was to fit different models to the Doppler maps using the program "stream.pro". This program requires different input parameters which need to be specified when running it, e.g. mass of the primary (M_1), mass ratio (q) = M_2/M_1, orbital period ($P_{\rm orb}$) and the binary inclination (i). This program also marks the location of the primary and secondary with a "×" and the location the centre of mass of the binary is marked with a "+". The location of the accretion stream trajectory is indicated by a solid blue line and marks the trajectory followed by the materials moving at stream velocity; the location along the stream is marked in units of r/a. The Roche-lobe of the secondary star is also indicated.

Figures 4.15 to 4.18 (top panels) show the Doppler maps of HeII 4686Å, H_α, and H_β for EC21178-54 with the following parameters: $q = 0.36$, $M_1 = 0.75\ M_\odot$, $M_2 = 0.27\ M_\odot$ and $i = 70°$. We used Eq. 15 of Patterson et al. (2005) to approximate the mass of the secondary star given the orbital period, and assumed that the mass of the WD primary must be $\sim$ 0.75 $M_\odot$ (e.g. Rodríguez-Gil et al. 2007a). These parameters were used to compute the Roche-lobe and the stream overlaid on the Doppler maps. The phase resolution was set to 0.05, since we had few spectra. This is not quite good enough to accurately determine any detailed disc structure, but it does provide information on the disc extent, the bright spot, the stream, and any other global feature.

Figures 4.15 and 4.16 (top panels) show the Doppler maps obtained from the HeII 4686Å lines. The two figures (Figure 4.15 and 4.16) reveal an asymmetric accretion disc, with no evidence of the bright spot emission. But there is evidence of a spiral structure which is interpreted as the indication of the presence of the spirally-induced shock waves in the accretion disc such as that observed in the DN IP Peg (Steeghs et al. 1997, Armitage &

Murray 1998, Harlaftis et al. 1999, Steeghs & Stehle 1999). There is a strong two-armed disc asymmetry visible, especially in Figure 4.15, which is reminiscent of the two-armed spiral structure that have been observed and simulated in the accretion disc of DNe during outburst (Armitage & Murray 1998, Steeghs & Stehle 1999). The emission in Figure 4.16 is concentrated in the first and third quadrant, and result from the effect of spiral shock waves in the accretion disc. No emission from the irradiated hemisphere of the secondary star is seen in the Doppler maps of HeII 4686Å. This is further confirmed by the absence of the low-velocity component in the observed trailed spectra of HeII 4686Å (see Section 4.4.2). The non-equal emission of the two sides of the asymmetry lends some support to the models of Smak (2001).

The asymmetry and non-equal intensity of the two regions of emissions observed in the Doppler maps of EC21178-54 is similar to that observed in some DNe during outbursts, e.g. U Gem (Groot 2001), EX Dra (Joergens et al. 2000) and SS Cyg (Steeghs et al. 1996). In DNe these always decay when the system returns to quiescence. When the system is in outburst, the disc radius expands and is comparable to the tidal radius. But when the system returns to a quiescent state, the disc shrinks to smaller radius compared to the tidal radius, and consequently, the spiral waves disappear. It is not yet clear if this spiral structure in EC21178-54 is permanent or not. But since this was seen in both observations taken a month apart (2011 September to 2011 October), one might suspect that EC21178-54 has an extended period of excited spiral structures in the accretion disc. This is only the fourth example of spiral waves in a NL, e.g. V347 Pup (Thoroughgood et al. 2005), V3885 Sgr (Hartley et al. 2005), and UX UMa (Neustroev et al. 2011).

In Figures 4.17 and 4.18, the top panels show the Doppler maps of the H_α and H_β lines. The Doppler maps of the Balmer lines also suggest an asymmetric accretion disc similar to that of HeII 4686Å lines but with less defined spiral structure. In general, the Doppler maps of the Balmer lines reveal a more circular accretion disc rather than the one elongated in the first and third quadrant revealed in the Doppler maps of HeII 4686Å lines. The disc extent is consistent with that of the HeII 4686Å lines. The Doppler map of the H_α line (Figure 4.17 top panel) shows no evidence of the emission associated with irradiated secondary, whereas that of H_β line (Figure 4.18 top panel) suggest that there could be emission from the secondary star. This possibly shows heating of the secondary star by radiation from the outer regions of the accretion disc. The reality of this feature in the Doppler map of H_β is questionable (see Section 4.4.2). A possible reason for the absence of the distinct spiral structure in the Doppler maps of the Balmer lines is that these lines are more strongly affected by the additional absorption component in the lines, making the Doppler maps difficult to interpret.

4.4.2 Trailed spectra of the line profiles

The bottom panels of Figures 4.15 to 4.18 show the observed continuum-normalized and phase-binned trailed spectra of HeII 4686Å, H_α and H_β lines respectively. The image on the bottom left of each figure show the trailed spectra based on the input spectra, whereas the image on the bottom right of each figure show the trailed spectra reconstructed based on the input data/Doppler maps. The agreement between both trailed spectra (observed and reconstructed) serves as a measure of the reliability of the Doppler maps.

The observed trailed spectra of HeII 4686Å lines from the observations of 2011 October 22-23 and 2011 September 5 (Figures 4.15 and 4.16 bottom left) show two peaks in emission separated by $\sim$ 1000 km/s at phase 0.0 with the semi-amplitude of $\sim$ 600 km/s. The two peaks moves in anti-phase direction with respect to each other. At phase $\sim$ 0.2, the two peaks comes to within 200 km/s of each other; it is not clear if this two peaks swaps side. But at about phase $\sim$ 0.7, the redshifted peak crosses the zero velocity from red to blue, whereas the blueshifted peak crosses the zero velocity from blue to red (see Figures 4.15 and 4.16 bottom left). The reconstructed trailed spectra for HeII 4686Å lines (Figures 4.15 and 4.16 bottom right) show consistent results with the observed trailed spectra. The trailed spectra of HeII 4686Å for EC21178-54 are very similar to that of IP Peg for the same line (Harlaftis et al. 1999). They both show at least two peaks in emission that move in anti-phase. The only difference is the absence of the third central peak in emission in both trailed spectra of HeII 4686Å of EC21178-54, which is present for IP Peg. This central feature is associated with the secondary star and is seen as an S-wave in the trailed spectra. It is most common in DNe during outbursts and is thought to be due to the irradiation of the secondary star, e.g. IP Peg (Harlaftis et al. 1999).

Figure 4.17 (bottom left) show the observed trailed spectra of the H_α line from 2011 September 5 data. There are two emission peaks that are separated by $\sim$ 600 km/s and clearly visible throughout the orbital cycle. For the H_α line, the two emission peaks are moving in-phase with respect to each other. As with the HeII lines, the trailed spectra of the H_α do not show any emission that is attributed to the secondary star. This is evident by the absence of the central emission feature seen in the trailed spectra of IP Peg during outbursts (Steeghs et al. 1997). The reconstructed trailed spectra of this line is also consistent with the observed trailed spectra.

The observed trailed spectra of the H_β line from 2011 October 22-23 data (Figure 4.18 bottom left) resembles that of the H_α line. There are two emission peaks that are clearly visible and moving in-phase with each other. The separation between the two peaks is $\sim$ 600 km/s and remains constant throughout the orbital phase. The central absorption dip is present in H_β. However, at $\phi \sim 0.7$, the second peak disappear or switches to absorption and re-appears at $\phi \sim 0.9$. The reconstructed trailed spectra of H_β lines reveals the present of a third peak which crosses from blue to red at $\phi \sim 0.2$ and again crosses from red to blue at $\phi \sim 0.7$, consistent with the RV curves. This peak is not present in the observed trailed spectra but is associated with the emission from the secondary star. The reconstructed trailed spectra is not consistent with the observed trailed spectra. This is because the redshifted peak in the reconstructed spectra never disappear at phases 0.7-0.9, whereas it should according to the observed spectra. Therefore, the emission associated with the secondary star should be interpreted with extreme care. The χ^2 value for the H_β line was approximately 1.6, whereas the values of χ^2 of the other lines were much less than 1.5, e.g. 1.2 (2011 October) and 1.0 (2011 September) for HeII 4686Å, and 1.4 for the H_α line.

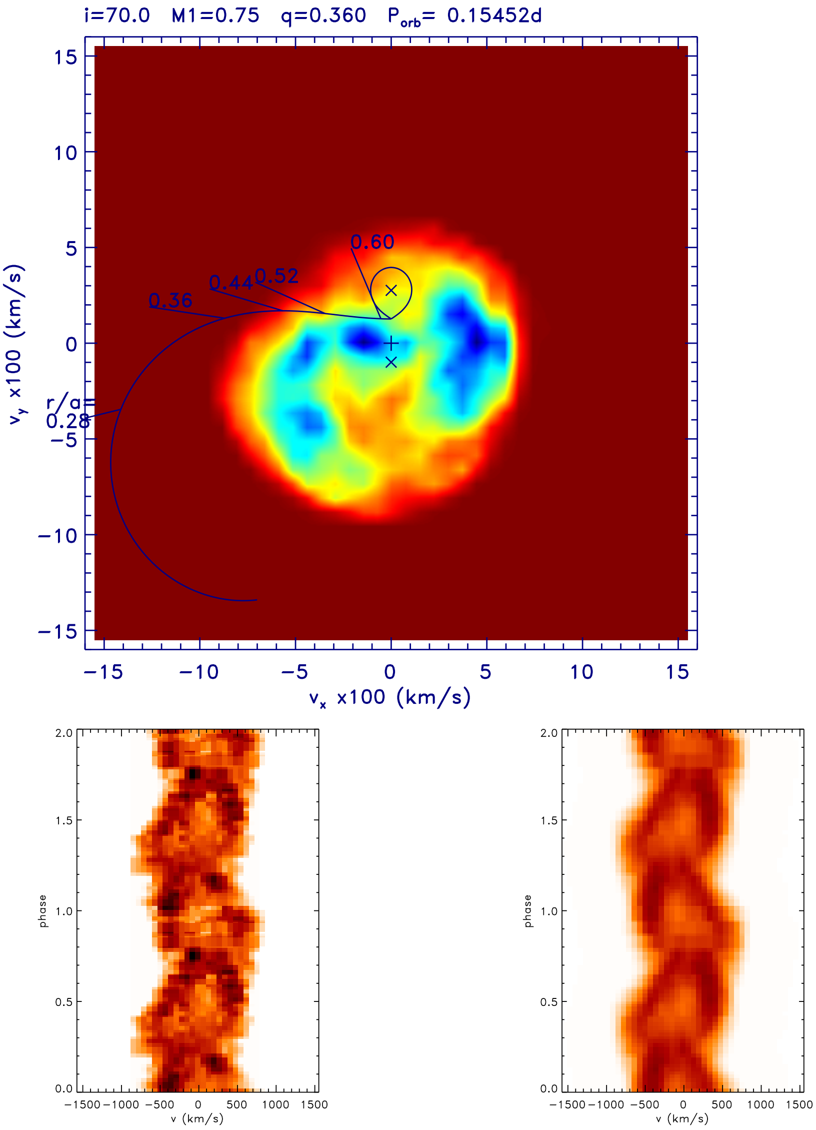

Figure 4.15: The Doppler map (top) and trailed spectra (bottom) of HeII 4686Å. The bottom left image is the trailed spectra from the input data and the image on the bottom right is the trailed spectra reconstructed based on the input data (2011 October 22-23).

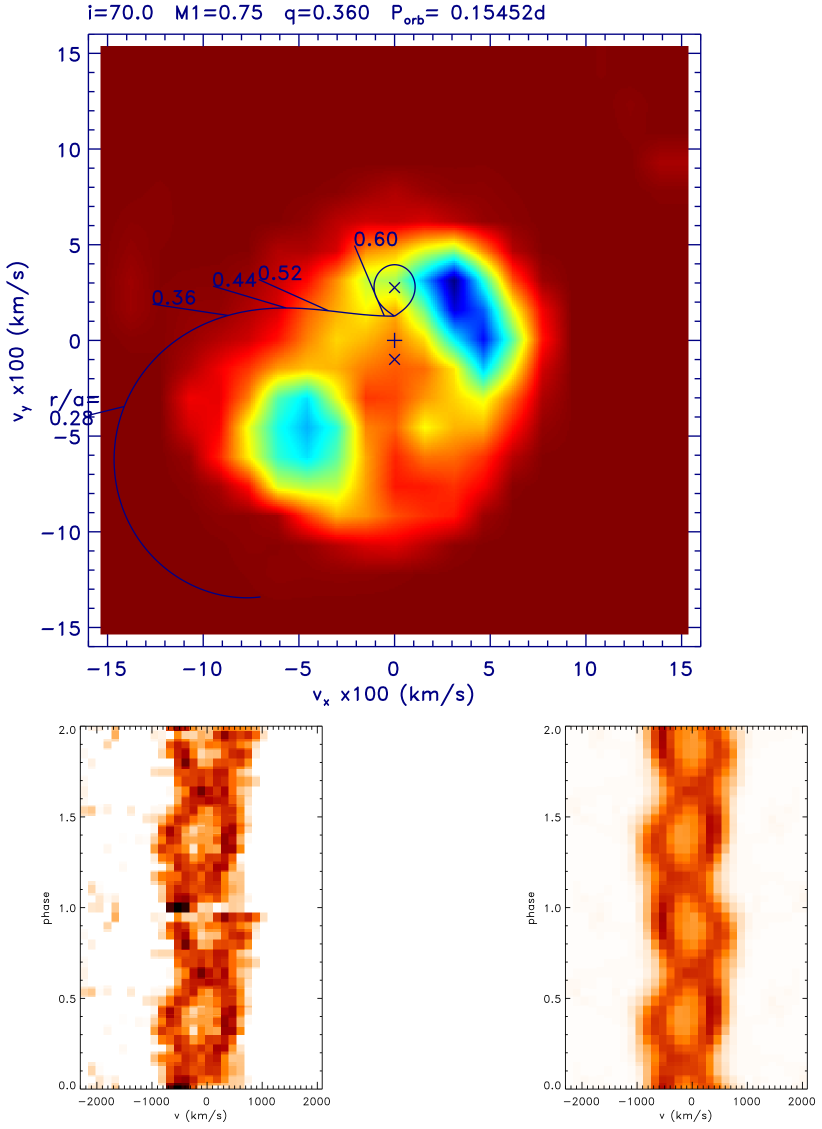

Figure 4.16: The Doppler map (top) and trailed spectra (bottom) of HeII 4686Å. The bottom left image is the trailed spectra from the input data and the image on the bottom right is the trailed spectra reconstructed based on the input data (2011 September 5).

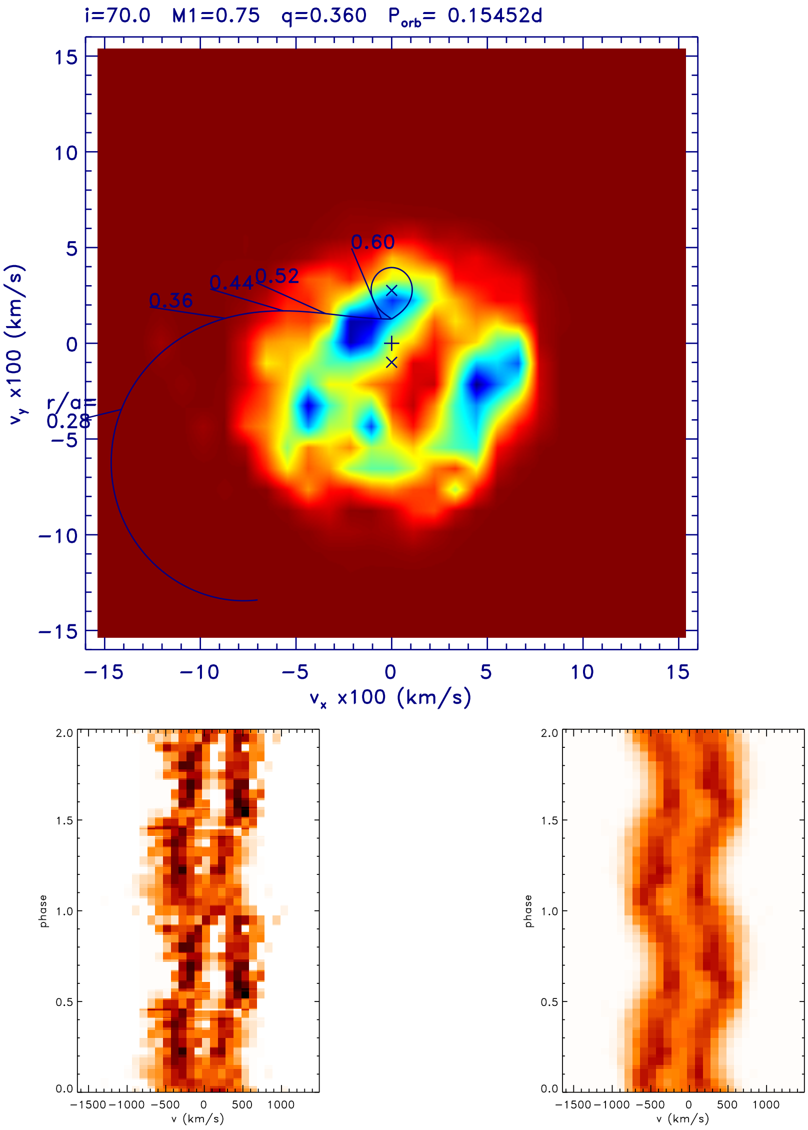

Figure 4.17: The Doppler map (top) and trailed spectra (bottom) of H_α. The bottom left image is the trailed spectra from the input data and the image on the bottom right is the trailed spectra reconstructed based on the input data (2011 September 5).

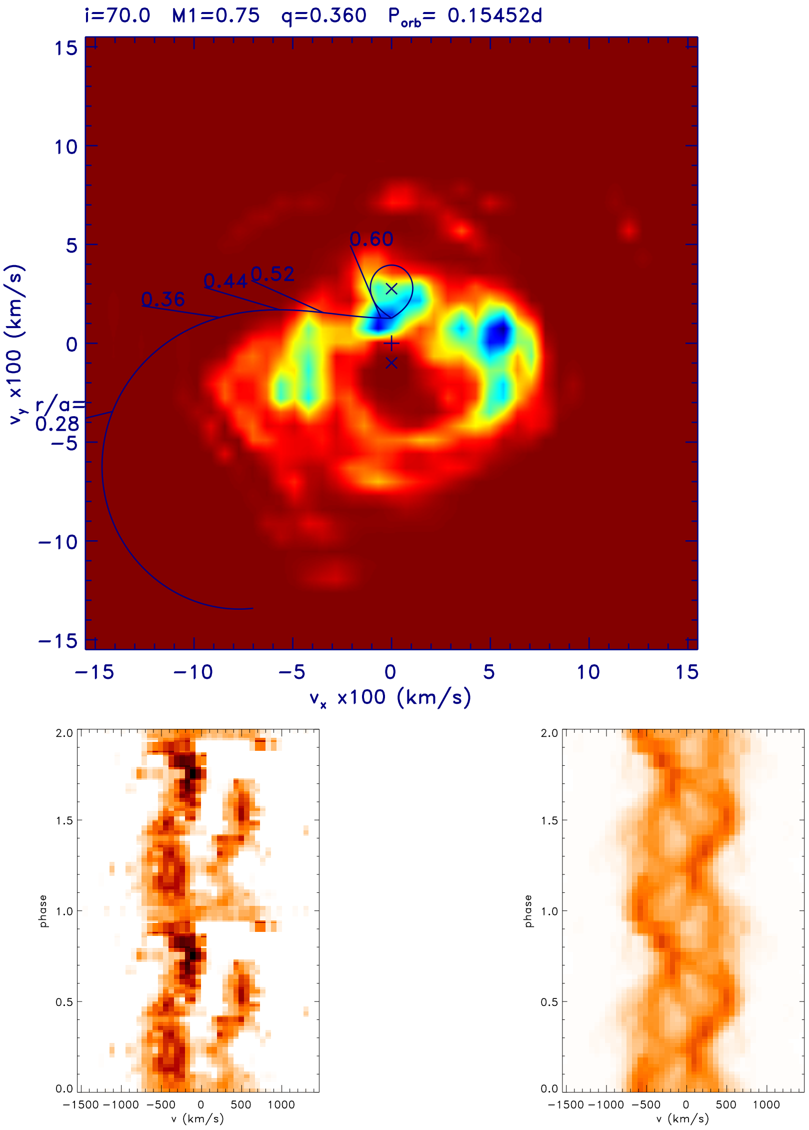

Figure 4.18: The Doppler map (top) and trailed spectra (bottom) of H_β. The bottom left image is the trailed spectra from the input data and the image on the bottom right is the trailed spectra reconstructed based on the input data (2011 October 22-23).

Chapter 5

Discussion

In Chapter 4 we presented phase-resolved spectroscopy of EC21178-54. The spectra are dominated by emission from HeII 4686Å, Balmer lines, and several other HeI lines. Here I discuss some of the interesting features observed as well as their implications, and possible future observations that may contribute to our understanding of spectral features and accretion in CVs.

5.1 Basis properties of EC21178-54

The results presented in Chapter 4 followed from four nights worth of observations of our target object, EC21178-54, covering at least one orbital phase of the system per epoch. The light curve of EC21178-54 shows deep V-shaped eclipses of the primary that are symmetrical, typical of SW Sex or RW Tri stars of NLs, and suggesting a high-inclination system. The photometry was used to establish a new ephemeris of EC21178-54, which was crucial for phasing our spectroscopic data.

Our spectroscopic analysis has revealed that EC21178-54 is dominated by emission from the accretion disc; the double-peaked emission lines confirm the presence of the highly inclined accretion disc. The strength of the HeII 4686Å for EC21178-54 is similar and/or comparable to that seen during the outbursts of IP Peg (Marsh & Horne 1990). The ratio of HeII 4686Å to H_β is greater than unity and the presence of HeII 5411Å suggests that these two lines originate from the region which has higher than normal level of ionization, e.g. SW Sex (Groot et al. 2001). H_δ and H_ϵ, and some HeI lines show both emission and absorption cores. The spectra of EC21178-54 show broad emission features from HeII at 4200 Å and CII at 4267 Å, these lines were present in the spectra of IP Peg during outburst (Marsh & Horne 1990). Based on these characteristics alone we may conclude that EC21178-54 is a member of either the RW Tri or UX UMa class because it changes in spectral characteristics all the time (and since the double-peaked emission lines rule out the SW Sex membership).

From the average spectra shown in Figures 4.3 and 4.4 (Chapter 4), it is clear that the spectra of EC21178-54 change with time from epoch to epoch. The average spectrum from 2002 September 7 shows broad and double-peaked emission lines in HeII 4686Å and the Balmer series but in pure emission (see Figure 4.4 top panel). The average spectrum obtained in 2011 September 5 show broad and double-peaked emission lines from H_α and HeII 4686Å, see Figures 4.3 (middle and bottom panels) and 4.4 (middle panel). But H_β and H_γ show two components: one peak in emission and other absorption. H_δ, H_ϵ and the other members of the higher Balmer series appears in pure absorption. The average spectrum obtained in 2011 October 22-23 shows the usual broad double-peaked emission lines from HeII 4686Å, H_β and H_γ. H_δ and H_ϵ shows two peaks, one in emission and the other in absorption. This suggest that EC21178-54 was observed in three different states namely: pure emission (2002 September), pure absorption (2011 September), and mixed absorption and emission (2011 October). Based on these results/analysis we conclude that our target might undergo variations in mass-transfer rate, or, at times it is dominated by an additional absorption component associated with the bright spot. We have seen that the bright spot appears strong at $0.75 \leq \phi \leq 0.95$ (see Section 4.2.2), and the higher Balmer lines change to absorption when the bright spot is visible. This short lived absorption comes from a vertically extended region above the bright spot Groot et al. (2001).

From radial velocity measurements of the emission line we find that the heliocentric systemic (γ) velocity of the system is -50 ± 14 km/s for EC21178-54 and the velocity amplitude (K_1) of 143 ± 19 km/s (Table 4.2). These measurements are based on the HeII 4686Å and H_α lines. The observed and reconstructed trailed spectra of EC21178-54 were consistent between the two observations, except for H_β which suggested a third component due to emission from the secondary star. We question the reality of this component in the Doppler map given the strong time variable absorption component of H_β in the trailed spectra.

We constructed Doppler maps of the three strongest emission lines. The results shown in Section 4.4.1 reveal an asymmetric and highly inclined accretion disc for EC21178-54. There is no evidence of emission from near the WD and emission from the secondary is only seen in the Doppler map of the H_β line, but the latter could be an artifact. NLs are disc-dominated systems and their luminosity is dominated by emission from the accretion disc and the bright spot. Doppler maps of HeII 4686Å line revealed the presence of a distorted accretion disc with two spiral arms (Figures 4.15 and 4.16). Such spiral structure has been seen before in the Doppler maps of three other NLs, e.g. V347 Pup (Thoroughgood et al. 2005), V3885 Sgr (Hartley et al. 2005), and UX UMa (Neustroev et al. 2011). This makes EC21178-54 the fourth NL to show spiral structure in its Doppler map. The previous three systems show spirals in the Balmer lines, whereas our target reveal them in HeII 4686Å. The spiral arms found in EC21178-54 are similar to those found in the Doppler maps of the DN IP Peg (e.g. Steeghs et al. 1997, Harlaftis et al. 1999) and EX Dra (Joergens et al. 2000) during outburts. But the spiral arms in the HeII 4686Å lines of EX Dra do not follow a circle centred on the WD but rather elongated along the (V_x, V_y) axis, the same appear to hold for EC21178-54 (see Figure 4.15). Doppler maps of H_α and H_β reveal a non-circular accretion disc, and are harder to interpret due to the time-variable absorption component. The best physical model to describe the observed Doppler maps of EC21178-54 suggest that $q = 0.36$, $M_1 = 0.75\ M_\odot$, $M_2 = 0.27\ M_\odot$, and $i = 70°$. The high inclination was selected to account for deep eclipses seen in the light curve of EC21178-54.

5.2 Future Work

EC21178-54 shows different spectral characteristics at different epochs: from pure absorption through mixed absorption and emission to pure emission. Recently, UX UMa was reported to show similar variations on a yet undetermined time scale (Neustroev et al. 2011). To understand this variable behaviour, more spectroscopic data taken at different epochs will be required. EC21178-54 has shown spiral structure in its Doppler maps on two occasions; whether these are permanent or not remain unknown. Thus more high resolution spectroscopic data, possibly with a large telescope like SALT, is needed to study the persistent excitation of two armed spirals in the accretion disc of EC21178-54. Such data will also help in the measurements of the radial velocities of the secondary star if it is detectable in the spectra. The results could be used to further constrain the physical properties of EC21178-54.

In this section, I would like to compare EC21178-54 with V3885 Sgr, the only NL with a secure radio detectation (Section 1.4). V3885 Sgr is one of the brightest NLs known to-date, its magnitude ranges between 9.0-10.5 mag. It belongs to the UX UMa subclass of NLs. It has been observed spectroscopically in the optical regime on several occasions, e.g. (Haug & Drechsel 1985, Hartley et al. 2005, Ribeiro & Diaz 2007). The average spectrum of V3885 Sgr shows very broad absorption profiles from the Balmer lines (e.g. H_β and H_γ) and HeI line at 4471 Å, with superimposed emission (Hartley et al. 2005). Also present are weak emission in HeII 4686Å and CIII/NIII blend at 4650 Å but the broad emission appears devoid of the emission structure associated with the absorption lines. The other HeI lines (at 4387 Å, 4713 Å and 4921 Å) are seen as weak absorption/emission lines. H_β, H_γ and HeI 4471Å line profiles are variable over the orbital cycle. No variations in spectral characteristics at different epochs has been suggested for V3885 Sgr as yet. Hartley et al. (2005) find spiral structures from the Doppler maps of the Balmer lines and HeI 4471Å. They also find evidence of the secondary star in the trailed spectra as well as the Doppler maps of H_β and H_γ. Recently, V3885 Sgr was shown to be associated with a 0.16 mJy radio source (see Körding et al. 2011).

Despite the different spectral characteristics of V3885 Sgr and EC21178-54, both have prominent spiral structures in their discs. Perhaps it is worthwhile to target the NLs with this disc feature with the new generation of sensitive radio arrays to search for radio emission. Given the advancement in technology and radio astronomy, it will be possible to discover more radio sources fainter than V3885 Sgr. For example, one of the Expanded Very Large

Telescope[1] (EVLA) primary goals include investigating and understanding radio transients. In addition, the ThunderKAT large array project on the Karoo Array Telescope[2] (MeerKAT) has more than 3000 hours of observing time fully dedicated to search for and study radio transients. Furthermore, the Square Kilometre Array[3] (SKA), which will be constructed in 2020, will also aid in studying and understanding radio transient. All these facilities will be available and may prove crucial in revealing new transient and also broadening our knowledge of transient events as well as radio emission in CVs.

---

[1] see https://science.nrao.edu/facilities/evla for more details on EVLA.

[2] http://www.ska.ac.za/meerkat/

[3] For more details visit the SKA-SA website http://www.ska.ac.za/

Appendix A

Original spectra of EC21178-54

A.1 Finding chart of EC21178-54

Figure A.1 shows the finding chart of EC21178-54 (the star at the centre of the image) marked by two vertical lines. The other bright star on the left was used to correct for instrumental response.

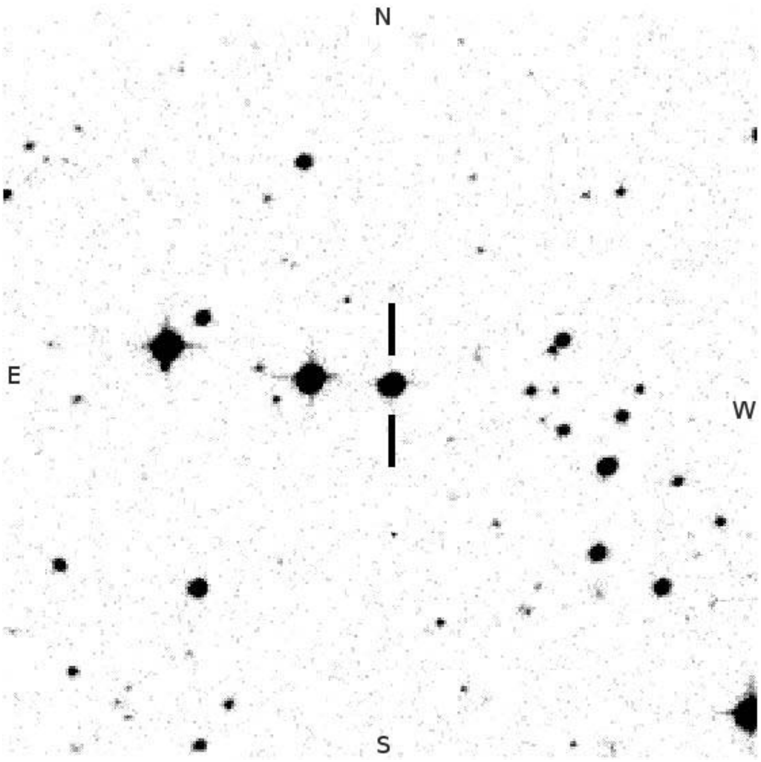

Figure A.1: The finding chart of EC21178-54 from cbastro website. This image is 5 × 5 arcmin^2. North is up and East is left.

A.2 Spectra of EC21178-54

In this appendix we show all the individual continuum normalized spectra of EC21178-54.

A.2.1 2002 archival observations

The spectra obtained in 2002 September are shown in Figure A.2, and they have been phased using Eq. (4.1). The numbers in brackets (1 to 7) denotes the spectral number from the first spectrum to the last, taken on that night of observations. The orbital phase increases from bottom to top. The spectra we had were insufficient to cover one orbital cycle of EC21178-54, and this is evident from Figure A.2.

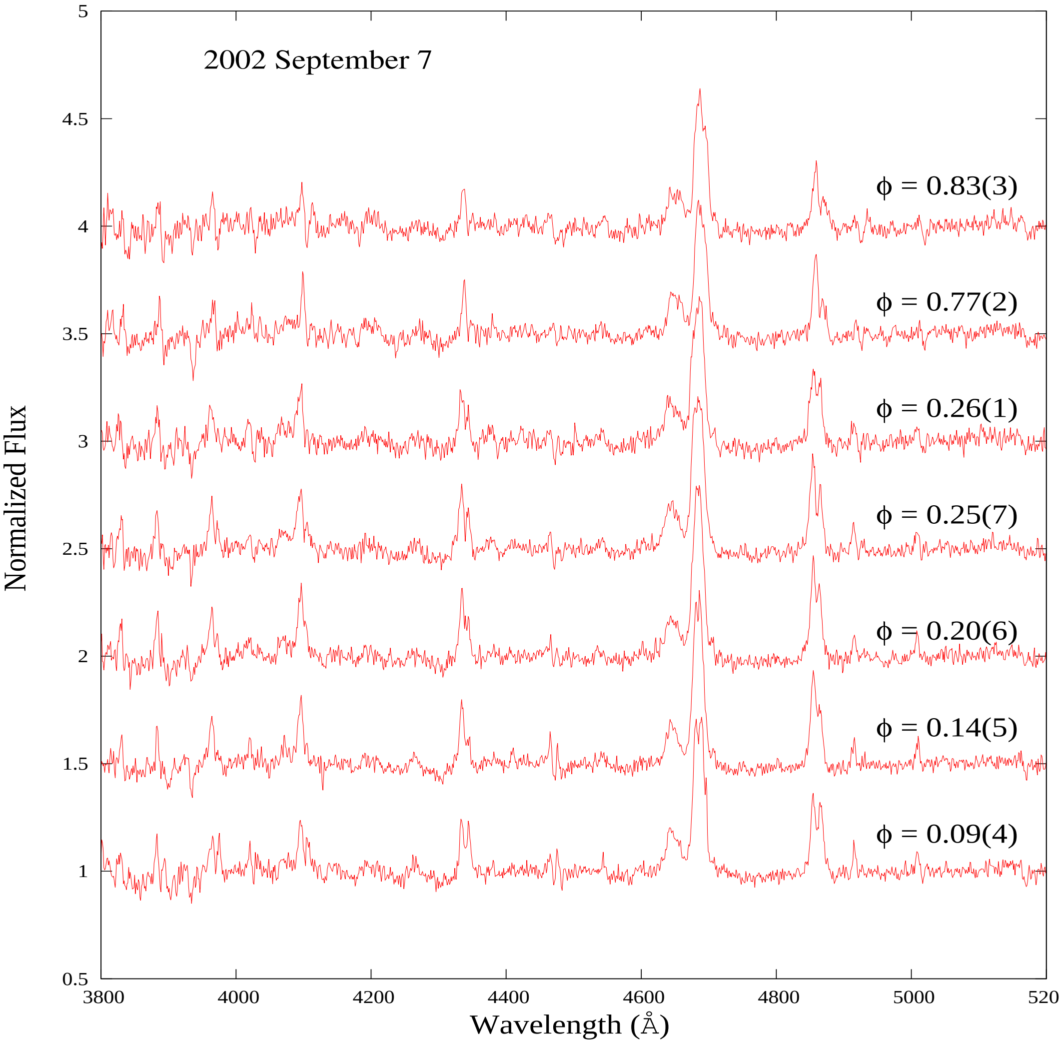

Figure A.2: The individual spectra of EC21178-54 obtained on 2002 September 7. All spectra have been normalized to the continuum level and the flux of each spectrum has been shifted from bottom to top by $\Delta flux = 0.5$ for display purposes.

A.2.2 2011 September observations

Figures A.3 and A.4 show the spectra obtained in 2011 September using grating number 7 (which covers the wavelengths from 3500Å to 7500Å). The spectra has been phased using Eq. 4.2, and the numbers 1 to 24 in brackets that appear in the figures represent the sequence in which they were obtained. The orbital phase increases from bottom to top, with the phases 0.0 to 0.48 in Figure A.3 and the remaining phases, $0.49 < \phi < 0.95$, are shown in Figure A.4.

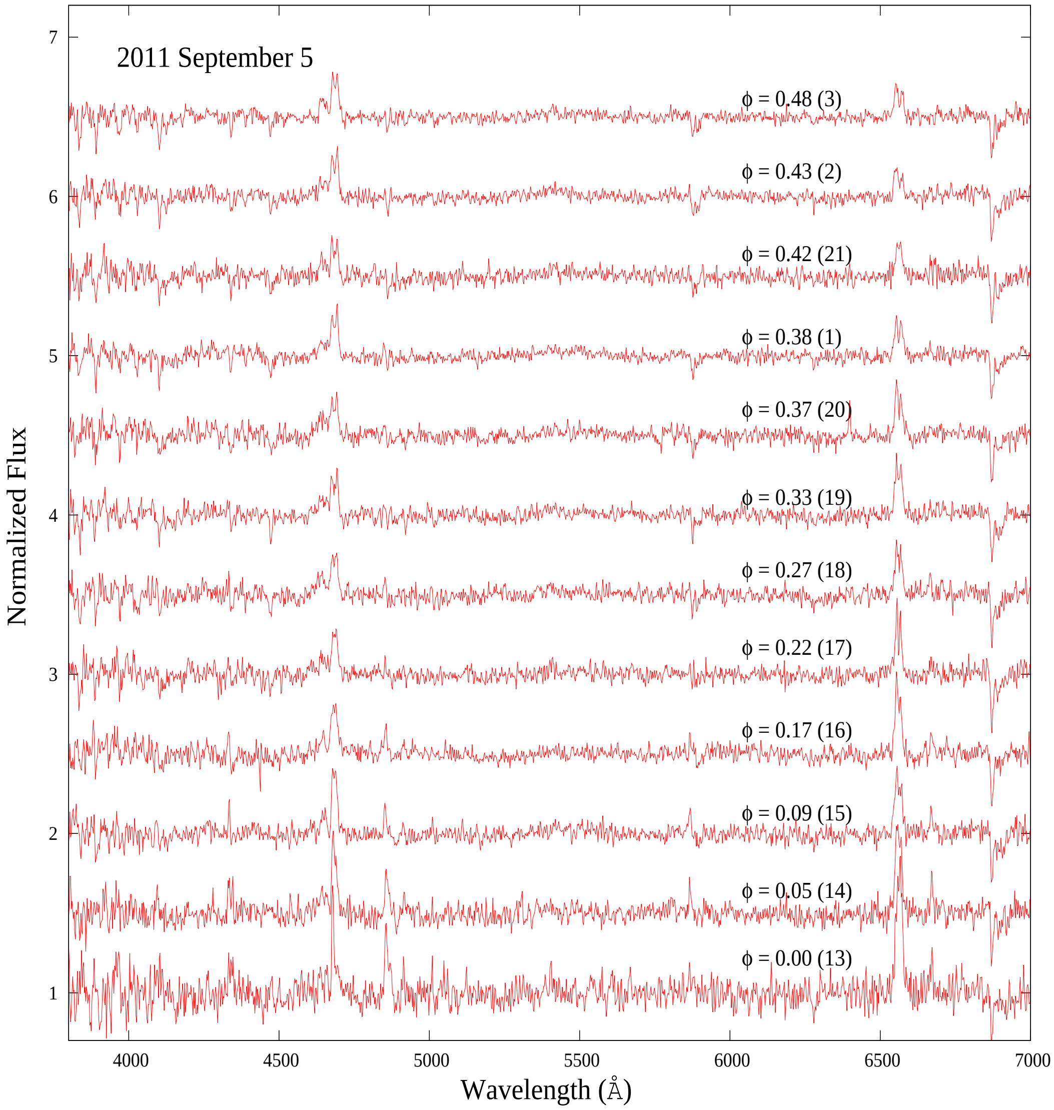

Figure A.3: The individual spectra of EC21178-54 obtained on 2011 September 5. All spectra have been normalized to the continuum level and the flux of each spectrum has been shifted from bottom to top by $\Delta flux = 0.5$ for display purposes.

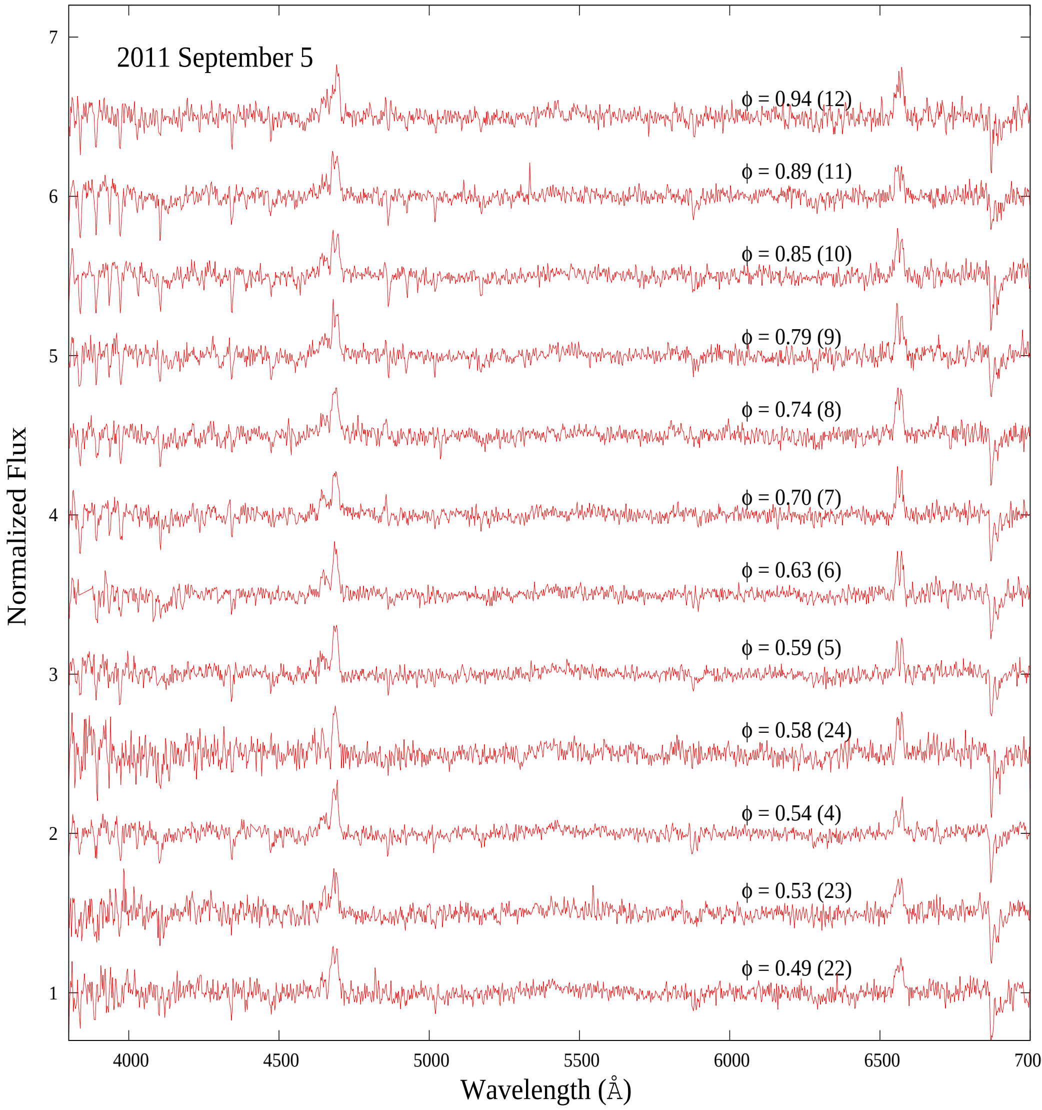

Figure A.4: The individual spectra of EC21178-54 obtained on 2011 September 5. All spectra have been normalized to the continuum level and the flux of each spectrum has been shifted from bottom to top by $\Delta flux = 0.5$ for display purposes.

A.2.3 2011 October observations

The spectra obtained in 2011 October were treated in the same way as those of 2011 September, and the results are shown in Figures A.5 and A.6. The numbers 1 to 12 in brackets on each figure represents the sequence of spectra taken on each night. The orbital phases were calculated using the ephemeris given in Eq. (4.2), and each date covers one orbital cycle of the binary. The phase increases from bottom to top in each figure, but we placed those spectra with $\phi > 0.95$ at the bottom because they corresponds to times of the eclipse of the bright spot and accretion disc (e.g. $\phi = 0.996$ in the bottom of Figure A.5).

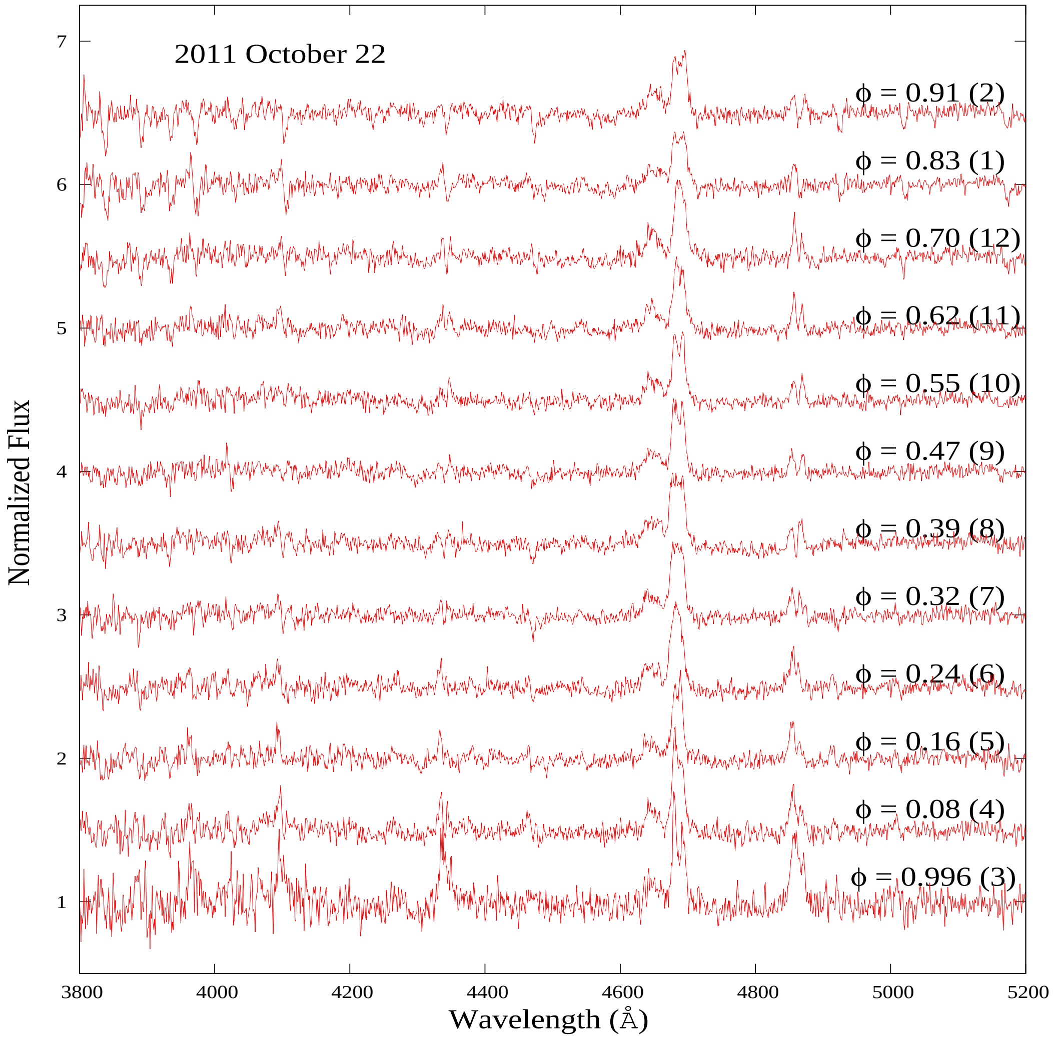

Figure A.5: The individual spectra of EC21178-54 obtained on 2011 October 22. All spectra have been normalized to the continuum level and the flux of each spectrum has been shifted from bottom to top by $\Delta flux = 0.5$ for display purposes.

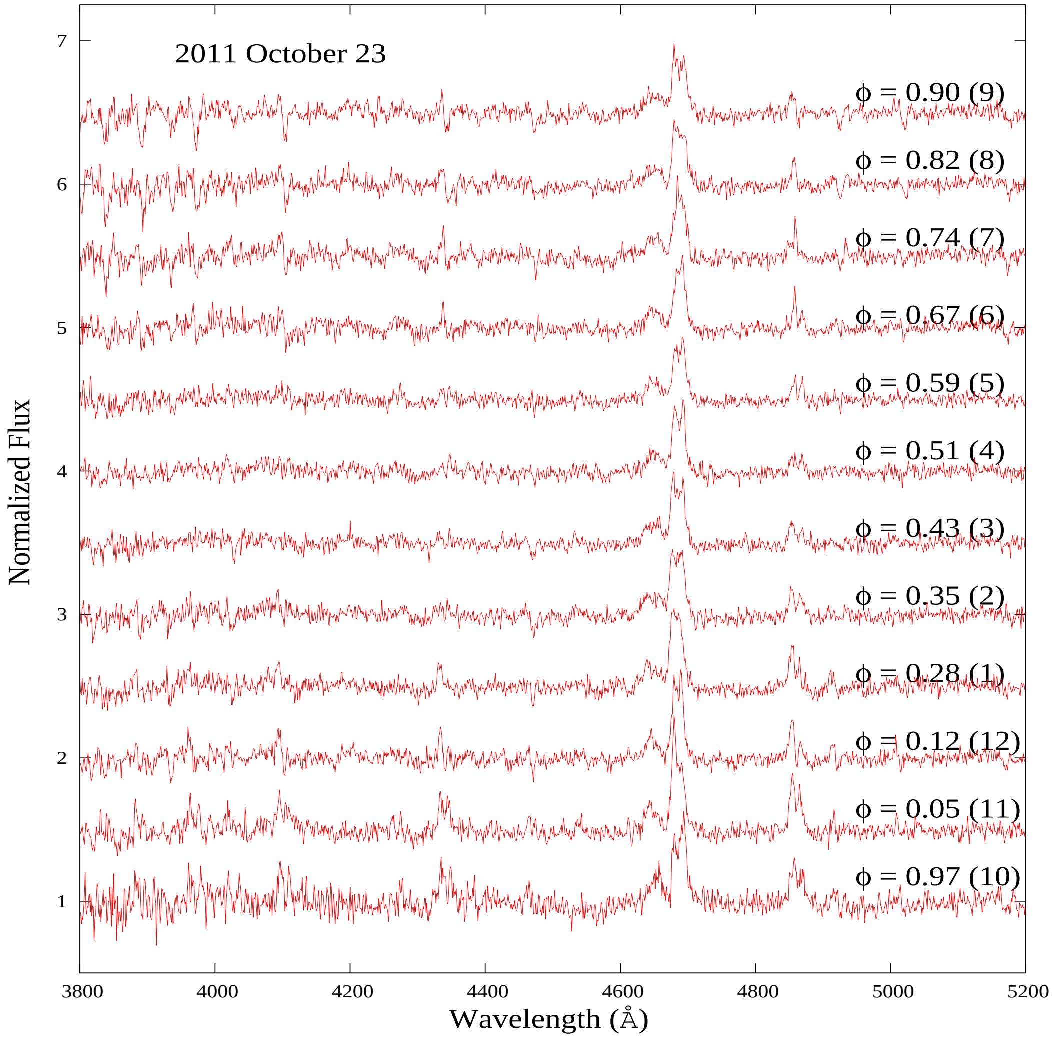

Figure A.6: The individual spectra of EC21178-54 obtained on 2011 October 23. All spectra have been normalized to the continuum level and the flux of each spectrum has been shifted from bottom to t op by $\Delta flux = 0.5$ for display purposes.

Bibliography

Armitage, P. J. & Murray, J. R. 1998, MNRAS, 297, L81

Baldwin, J. A. & Stone, R. P. S. 1984, MNRAS, 206, 241

Bath, G. T. 1969, ApJ, 158, 571

—. 1972, ApJ, 173, 121

—. 1973, Nature Physical Science, 246, 84

Brocksopp, C., Sokoloski, J. L., Kaiser, C., Richards, A. M., Muxlow, T. W. B., & Seymour, N. 2004, MNRAS, 347, 430

Calvelo, D. E., Vrtilek, S. D., Steeghs, D., Torres, M. A. P., Neilsen, J., Filippenko, A. V., & González Hernández, J. I. 2009, MNRAS, 399, 539

Coppejans, R., Gulbis, A. A. S., Kotze, M. M., Coppejans, D. L., Worters, H. L., Woudt, P. A., Whittal, H., Cloete, J., & Fourie, P. 2013, PASP, 125, 976

Dhillon, V. S. 1990, PhD thesis, Univ. Sussex, Falmer, Brighton

Dhillon, V. S., Jones, D. H. P., & Marsh, T. R. 1994, MNRAS, 266, 859

Dhillon, V. S., Smith, D. A., & Marsh, T. R. 2013, MNRAS, 428, 3559

Etzel, P. B. 2004, SBOP: Spectroscopic Binary Orbit Program (San Diego State University)

Faulkner, J. 1971, ApJ, 170, L99

Fender, R. P., Belloni, T. M., & Gallo, E. 2004, MNRAS, 355, 1105

Gänsicke, B. T. 2005, in Astronomical Society of the Pacific Conference Series, Vol. 330, The Astrophysics of Cataclysmic Variables and Related Objects, ed. J.-M. Hameury & J.-P. Lasota, 3

Gänsicke, B. T., Dillon, M., Southworth, J., Thorstensen, J. R., Rodríguez-Gil, P., Aungwerojwit, A., Marsh, T. R., Szkody, P., Barros, S. C. C., Casares, J., de Martino, D., Groot, P. J., Hakala, P., Kolb, U., Littlefair, S. P., Martínez-Pais, I. G., Nelemans, G., & Schreiber, M. R. 2009, MNRAS, 397, 2170

Green, R. F., Ferguson, D. H., Liebert, J., & Schmidt, M. 1982, PASP, 94, 560

Green, R. F., Schmidt, M., & Liebert, J. 1986, ApJS, 61, 305

Groot, P. J. 2001, ApJ, 551, L89

Groot, P. J., Rutten, R. G. M., & van Paradijs, J. 2001, A&A, 368, 183

—. 2004, A&A, 417, 283

Gulbis, A. A. S., Bus, S. J., Elliot, J. L., Rayner, J. T., Stahlberger, W. E., Rojas, F. E., Adams, E. R., Person, M. J., Chung, R., Tokunaga, A. T., & Zuluaga, C. A. 2011a, PASP, 123, 461

Gulbis, A. A. S., Elliot, J. L., Rojas, F. E., Bus, S. J., Rayner, J. T., Stahlberger, W. E., Tokunaga, A. T., Adams, E. R., & Person, M. J. 2010, in Bulletin of the American Astronomical Society, Vol. 42, AAS/Division for Planetary Sciences Meeting Abstracts #42, 1005

Gulbis, A. A. S., O'Donoghue, D., Fourie, P., Rust, M., Sass, C., & Stoffels, J. 2011b, in EPSC-DPS Joint Meeting 2011, 1173

Harlaftis, E. T., Steeghs, D., Horne, K., Martín, E., & Magazzú, A. 1999, MNRAS, 306, 348

Hartley, L. E., Murray, J. R., Drew, J. E., & Long, K. S. 2005, MNRAS, 363, 285

Haug, K. & Drechsel, H. 1985, A&A, 151, 157

Hawley, J. F. & Balbus, S. A. 1998, in Astronomical Society of the Pacific Conference Series, Vol. 137, Wild Stars in the Old West, ed. S. Howell, E. Kuulkers, & C. Woodward, 273

Hellier, C. 2001, Cataclysmic Variable Stars

Ho, L. C. 2005, Ap&SS, 300, 219

Homan, J., Wijnands, R., van der Klis, M., Belloni, T., van Paradijs, J., Klein-Wolt, M., Fender, R., & Méndez, M. 2001, ApJS, 132, 377

Horne, K. 1985, MNRAS, 213, 129

Horne, K. & Marsh, T. R. 1986, MNRAS, 218, 761

Hōshi, R. 1979, Progress of Theoretical Physics, 61, 1307

Howell, S. B., Nelson, L. A., & Rappaport, S. 2001, ApJ, 550, 897

Joergens, V., Spruit, H. C., & Rutten, R. G. M. 2000, A&A, 356, L33

Knigge, C. 2006, MNRAS, 373, 484

Knigge, C., Baraffe, I., & Patterson, J. 2011, ApJS, 194, 28

Körding, E., Rupen, M., Knigge, C., Fender, R., Dhawan, V., Templeton, M., & Muxlow, T. 2008, Science, 320, 1318

Körding, E. G., Jester, S., & Fender, R. 2006, MNRAS, 372, 1366

Körding, E. G., Knigge, C., Tzioumis, T., & Fender, R. 2011, MNRAS, 418, L129

Kotko, I. & Lasota, J.-P. 2012, A&A, 545, A115

Kraft, R. P., Mathews, J., & Greenstein, J. L. 1962, ApJ, 136, 312

Lasota, J.-P. & Hameury, J.-M. 2004, in Astronomical Society of the Pacific Conference Series, Vol. 315, IAU Colloq. 190: Magnetic Cataclysmic Variables, ed. S. Vrielmann & M. Cropper, 46

Lubow, S. H. & Shu, F. H. 1975, ApJ, 198, 383

Lucy, L. B. 1994, A&A, 289, 983

Lynden-Bell, D. 1969, Nature, 223, 690

Marsh, T. R. 2005, Ap&SS, 296, 403

Marsh, T. R. & Horne, K. 1988, MNRAS, 235, 269

—. 1990, ApJ, 349, 593

Martínez-Pais, I. G., Martín-Hernández, N. L., Casares, J., & Rodríguez-Gil, P. 2000, ApJ, 538, 315

Meyer, F. & Meyer-Hofmeister, E. 1981, A&A, 104, L10

Moore, P. & Collins, P. 1977, The astronomy of Southern Africa

Morales-Rueda, L., Marsh, T. R., & Billington, I. 2000, MNRAS, 313, 454

Motch, C. 1998, A&A, 338, L13

Neustroev, V. V., Suleimanov, V. F., Borisov, N. V., Belyakov, K. V., & Shearer, A. 2011, MNRAS, 410, 963

Noebauer, U. M., Long, K. S., Sim, S. A., & Knigge, C. 2010, ApJ, 719, 1932

O'Donoghue, D., Kilkenny, D., Koen, C., Hambly, N., MacGillivray, H., & Stobie, R. S. 2013, MNRAS, 431, 240

Osaki, Y. 1974, PASJ, 26, 429

—. 1996, PASP, 108, 39

—. 2005, Proceeding of the Japan Academy, Series B, 81, 291

Paczynski, B. & Sienkiewicz, R. 1981, ApJ, 248, L27

Papadaki, C., Boffin, H. M. J., & Steeghs, D. 2008, Journal of Astronomical Data, 14, 2

Patterson, J. 1984, ApJS, 54, 443

Patterson, J., Kemp, J., Harvey, D. A., Fried, R. E., Rea, R., Monard, B., Cook, L. M., Skillman, D. R., Vanmunster, T., Bolt, G., Armstrong, E., McCormick, J., Krajci, T., Jensen, L., Gunn, J., Butterworth, N., Foote, J., Bos, M., Masi, G., & Warhurst, P. 2005, PASP, 117, 1204

Patterson, J., Uthas, H., Kemp, J., de Miguel, E., Krajci, T., Foote, J., Hambsch, F.-J., Campbell, T., Roberts, G., Cejudo, D., Dvorak, S., Vanmunster, T., Koff, R., Skillman, D., Harvey, D., Martin, B., Rock, J., Boyd, D., Oksanen, A., Morelle, E., Ulowetz, J., Kroes, A., Sabo, R., & Jensen, L. 2013, MNRAS, 434, 1902

Pringle, J. E. 1981, ARA&A, 19, 137

Rappaport, S., Joss, P. C., & Webbink, R. F. 1982, ApJ, 254, 616

Rappaport, S., Verbunt, F., & Joss, P. C. 1983, ApJ, 275, 713

Ribeiro, F. M. A. & Diaz, M. P. 2007, AJ, 133, 2659

Ritter, H. 2010, Mem. Soc. Astron. Italiana, 81, 849

Ritter, H. & Kolb, U. 2003, A&A, 404, 301

—. 2005, VizieR Online Data Catalog, 5113, 0

Rodríguez-Gil, P., Gänsicke, B. T., Araujo-Betancor, S., & Casares, J. 2004, MNRAS, 349, 367

Rodríguez-Gil, P., Gänsicke, B. T., Hagen, H.-J., Araujo-Betancor, S., Aungwerojwit, A., Allende Prieto, C., Boyd, D., Casares, J., Engels, D., Giannakis, O., Harlaftis, E. T., Kube, J., Lehto, H., Martínez-Pais, I. G., Schwarz, R., Skidmore, W., Staude, A., & Torres, M. A. P. 2007a, MNRAS, 377, 1747

Rodríguez-Gil, P., Schmidtobreick, L., & Gänsicke, B. T. 2007b, MNRAS, 374, 1359

Roelofs, G. H. A. 2007, PhD thesis, Radboud Universiteit Nijmegen

Rowland, S. W. 1979, in Image Reconstruction from Projections: Implementation and Applications, ed. G. T. Herman, 9

Sawada, K., Matsuda, T., & Hachisu, I. 1986, MNRAS, 219, 75

Schmidtobreick, L. 2013, Central European Astrophysical Bulletin, 37, 361

Schmidtobreick, L., Rodríguez-Gil, P., & Gänsicke, B. T. 2012, Mem. Soc. Astron. Italiana, 83, 610

Schneider, D. P. & Young, P. 1980, ApJ, 238, 946

Shafter, A. W. 1983, ApJ, 267, 222

Shafter, A. W. & Hessman, F. V. 1988, AJ, 95, 178

Shafter, A. W., Szkody, P., & Thorstensen, J. R. 1986, ApJ, 308, 765

Shakura, N. I. & Sunyaev, R. A. 1973, A&A, 24, 337

Smak, J. 1984, Acta Astronomica, 34, 161

Smak, J. I. 2001, Acta Astronomica, 51, 295

Sokoloski, J. L. & Kenyon, S. J. 2003, ApJ, 584, 1021

Southworth, J., Gänsicke, B. T., Marsh, T. R., de Martino, D., & Aungwerojwit, A. 2007a, MNRAS, 378, 635

Southworth, J., Hickman, R. D. G., Marsh, T. R., Rebassa-Mansergas, A., Gänsicke, B. T., Copperwheat, C. M., & Rodríguez-Gil, P. 2009, A&A, 507, 929

Southworth, J., Marsh, T. R., Gänsicke, B. T., Aungwerojwit, A., Hakala, P., de Martino, D., & Lehto, H. 2007b, MNRAS, 382, 1145

Southworth, J., Smalley, B., Maxted, P. F. L., Claret, A., & Etzel, P. B. 2005, MNRAS, 363, 529

Souza, S. P., Babcock, B. A., Pasachoff, J. M., Gulbis, A. A. S., Elliot, J. L., Person, M. J., & Gangestad, J. W. 2006, PASP, 118, 1550

Spruit, H. C. 1998, astro-ph/9806141

—. 2010, ArXiv:1005.5279

Spruit, H. C. & Ritter, H. 1983, A&A, 124, 267

Spruit, H. C. & Rutten, R. G. M. 1998, MNRAS, 299, 768

Steeghs, D. 2003, MNRAS, 344, 448

Steeghs, D., Harlaftis, E. T., & Horne, K. 1997, MNRAS, 290, L28

Steeghs, D., Horne, K., Marsh, T. R., & Donati, J. F. 1996, MNRAS, 281, 626

Steeghs, D., Howell, S. B., Knigge, C., Gänsicke, B. T., Sion, E. M., & Welsh, W. F. 2007, ApJ, 667, 442

Steeghs, D., O'Brien, K., Horne, K., Gomer, R., & Oke, J. B. 2001, MNRAS, 323, 484

Steeghs, D. & Stehle, R. 1999, MNRAS, 307, 99

Stetson, P. B. 1990, PASP, 102, 932

Stobie, R. S., Kilkenny, D., O'Donoghue, D., Chen, A., Koen, C., Morgan, D. H., Barrow, J., Buckley, D. A. H., Cannon, R. D., Cass, C. J. P., Cranston, M. R., Drinkwater, M., Hartley, M., Hawkins, M. R. S., Hughes, S., Humphries, C. M., MacGillivray, H. T., McKenzie, P. B., Parker, Q. A., Read, M., Russell, K. S., Savage, A., Thomson, E. B., Tritton, S. B., Waldron, J. D., Warner, B., & Watson, F. G. 1997, MNRAS, 287, 848

Szkody, P., Henden, A., Fraser, O., Silvestri, N., Bochanski, J., Wolfe, M. A., Agüeros, M., Warner, B., Woudt, P., Tramposch, J., Homer, L., Schmidt, G., Knapp, G. R., Anderson, S. F., Covey, K., Harris, H., Hawley, S., Schneider, D. P., Voges, W., & Brinkmann, J. 2004, AJ, 128, 1882

Szkody, P. & Piche, F. 1990, ApJ, 361, 235

Taylor, A. R., Seaquist, E. R., & Mattei, J. A. 1986, Nature, 319, 38

Thoroughgood, T. D., Dhillon, V. S., Steeghs, D., Watson, C. A., Buckley, D. A. H., Littlefair, S. P., Smith, D. A., Still, M., van der Heyden, K. J., & Warner, B. 2005, MNRAS, 357, 881

Thorstensen, J. R. 2000, PASP, 112, 1269

Thorstensen, J. R., Ringwald, F. A., Wade, R. A., Schmidt, G. D., & Norsworthy, J. E. 1991, AJ, 102, 272

Torbett, M. V. & Campbell, B. 1987, ApJ, 318, L29

Unda-Sanzana, E., Marsh, T. R., & Morales-Rueda, L. 2006, MNRAS, 369, 805

Verbunt, F. & Zwaan, C. 1981, A&A, 100, L7

Warner, B. 1987, MNRAS, 227, 23

—. 1995, Cambridge Astrophysics Series, 28

—. 2004, PASP, 116, 115

Warner, B., Woudt, P. A., & Pretorius, M. L. 2003, MNRAS, 344, 1193

Winkler, L. 1977, AJ, 82, 1008

Wolfe, Jr., R. H., Horak, H. G., & Storer, N. W. 1967, The machine computation of spectroscopic binary elements, ed. O. Struve & M. Hack, 251

Zietsman, E. 2008, Master's thesis, University of Cape Town